In-situ Study of the Growth, Composition and Morphology of III-V Semiconductor Nanowires

Sjökvist, Robin

2023

In-situ Study of the Growth, Composition and Morphology of III-V Semiconductor Nanowires

ROBIN SJÖKVIST | CENTRE FOR ANALYSIS AND SYNTHESIS | LUND UNIVERSITY

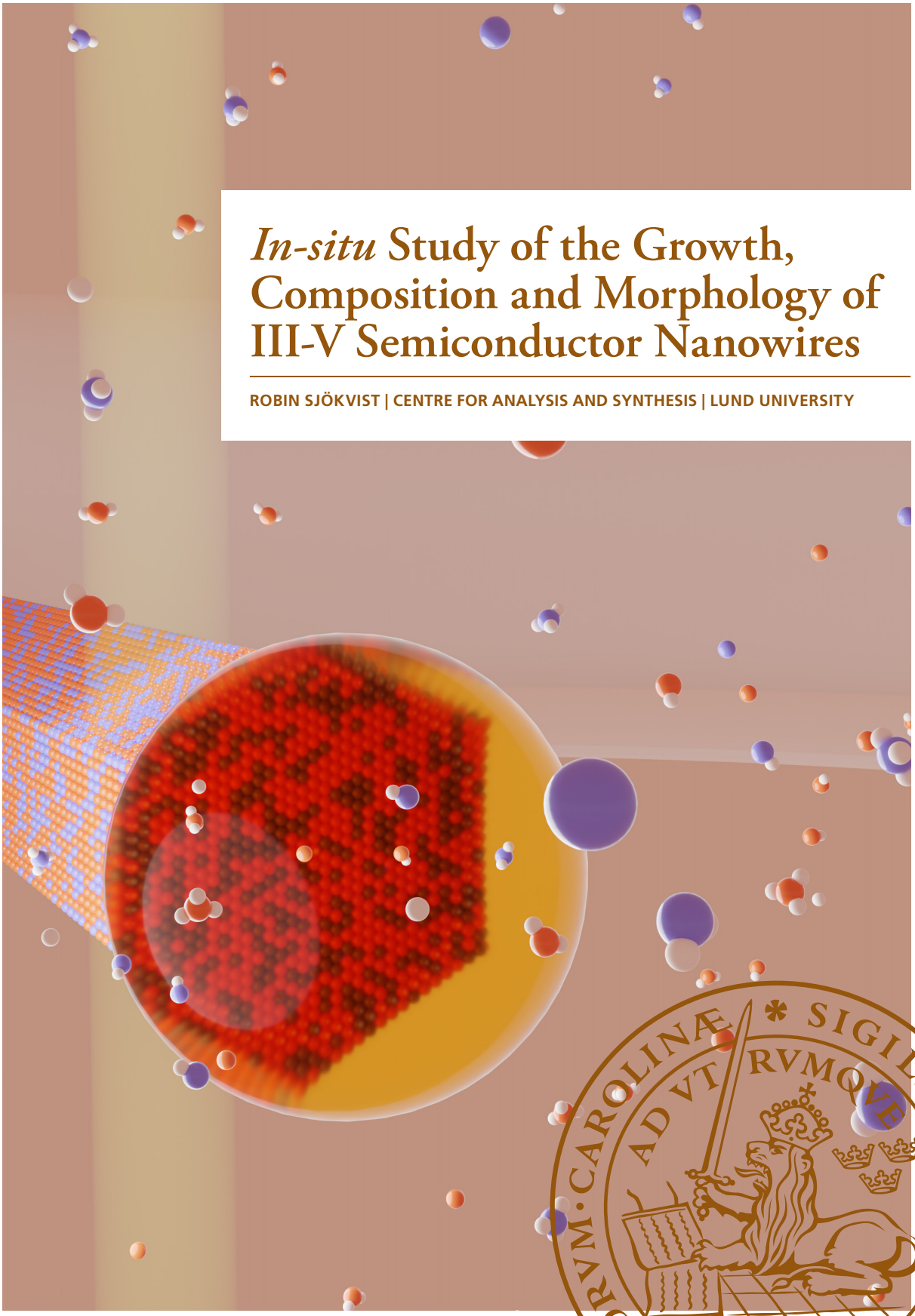

Indium, oh Indium, so rare and so fine,
In the world of materials, you're one of a kind.
Your unique properties, they do entice,
But using you in ETEM, is not so nice.

In an electron microscope, you're hard to place,
Your atoms so small, they're hard to trace.
But with your presence, insight we can glean,
Into the nanoscale, where you're often seen.

But oh, the struggle, it is oh so real,
To make you work, it takes a skilled hand and ideal.
Conditions so precise, it takes much care,
To get you ready, for the ETEM to be fair.

And even when ready, the process is tough,
The high energy beams, they can be rough.
But with patience and skill, and a bit of luck,
The data collected, is worth effort and muck.

So here's to Indium, our struggles we share,
In the pursuit of knowledge, and the answers we bear.
You may be difficult, but oh so divine.
In the world of materials, you're one of a kind.

Printed by Media-Tryck, Lund 2021 NORDIC SWAN ECOLABEL 3041 0903

LUND UNIVERSITY

ISBN 978-91-7422-974-5

Centre for Analysis and Synthesis
Department of Chemistry
Faculty of Science
Lund University

In-situ Study of the Growth, Composition and Morphology of III-V Semiconductor Nanowires

In-situ Study of the Growth, Composition and Morphology of III-V Semiconductor Nanowires

by Robin Sjökvist

LUND
UNIVERSITY

Thesis for the degree of Doctor of Philosophy
Thesis advisors: Prof. Kimberly Dick Thelander, Dr. Martin Ek Rosén, Dr. Daniel Madsen
Faculty opponent: Prof. Paul McIntyre

Doctoral dissertation to be publicly defended for the degree of PhD in lecture hall KC:A at the Department of Chemistry on Wednesday, the 4th of October 2023 at 9:00.

Organization
LUND UNIVERSITY

Department of Chemistry
Box 1
SE–221 00 LUND
Sweden

Document name
DOCTORAL DISSERTATION

Date of disputation
2023-10-04

Sponsoring organization

Author(s)
Robin Sjökvist

Title and subtitle
In-situ Study of the Growth, Composition and Morphology of III-V Semiconductor Nanowires

Abstract
It is widely known that nanoparticle seeded growth of III-V semiconductor nanowires often occurs via the vapor-liquid-solid mechanism. However, conventional growth of nanowires is carried out in closed systems, where most of the details and dynamics of the growth are impossible to follow. Since all analysis is typically carried out after growth completion and transfer, only the trends in the produced growth series give hints to the processes occurring at the nanoscale.

In this thesis, the growth of Au-seeded III-V semiconductor nanowires has been studied *in-situ*, during growth, by means of environmental transmission electron microscopy. The supply of growth species in the form of precursor molecules directly into the microscope column provides a unique opportunity to follow the nanowire growth while it is occurring, through all techniques commonly available in a transmission electron microscope. This means that nanoscale growth dynamics can be studied in real time under static or changing growth conditions, and changes in crystal structure, composition and morphology can be revealed.

The present investigation highlights the relation between the liquid nanoparticle and the solid nanowire. For GaSb nanowires, I show that the nanoparticle can swell by alloying to various extents with Ga, which will influence the formed nanowire diameter. I also investigate the compositional relationship between the Au-based nanoparticles and growing ternary InGaAs nanowires, where it is established that the solidified composition is dependent on both kinetics and thermodynamics. One of the main conclusions is that a high concentration of indium in the nanoparticle is needed in order to form indium rich solid InGaAs. The *in-situ* investigations reveal that nanowire growth is dynamic, and the layer-by-layer growth process consists of separate steps of material collection (incubation) and solidification (step-flow). I present how the layer-by-layer growth is affected by changes in the precursor flows for GaSb nanowires, and how the formation of defects in GaAs affects growth rate and can influence the growth behavior. Finally, I discuss the multilayer growth phenomenon in InGaAs nanowires, where multiple layers nucleate and grow simultaneously at the liquid-solid interface. In many cases the results are compared to simulations and models, which can be used to provide a more detailed understanding about the factors influencing the growth. The results presented in this thesis provide fundamental insight into the growth of nanostructures and are expected to be useful in the continued pursuit of atomic scale control.

Key words
Nanowire, Semiconductor, III-V, Transmission Electron Microscopy, *In-situ*, Environmental TEM, Crystal Growth

Classification system and/or index terms (if any)

Supplementary bibliographical information

Language
English

ISSN and key title

ISBN
978-91-7422-974-5 (print)
978-91-7422-975-2 (pdf)

Recipient's notes

Number of pages
265

Price

Security classification

In-situ Study of the Growth, Composition and Morphology of III-V Semiconductor Nanowires

by Robin Sjökvist

LUND
UNIVERSITY

A doctoral thesis at a university in Sweden takes either the form of a single, cohesive research study (monograph) or a summary of research papers (compilation thesis), which the doctoral student has written alone or together with one or several other author(s).

In the latter case the thesis consists of two parts. An introductory text puts the research work into context and summarizes the main points of the papers. Then, the research publications themselves are reproduced, together with a description of the individual contributions of the authors. The research papers may either have been already published or are manuscripts at various stages (in press, submitted, or in draft).

QR-codes: This thesis contains a QR-code at the start of every chapter. They exist to give the reader an idea of what *in-situ* nanowire growth looks like, so use your phone's camera or a dedicated QR reader to have a look! In order of appearance: QR 1: Nanowire growth with a tilted interface. QR 2: SI video 1 from **Paper v**, showing twin formation in GaAs. QR 3: Nanowire with defect at the interface. QR 4: Controlled GaAs nanowire nucleation. QR 5: Growing InGaAs nanowire. QR 6: SI video 3 from **Paper vi**, showing multilayer growth in InGaAs. QR 7: Nanowire growth from solid nanoparticle.

Cover illustration front: An illustration of an ETEM experiment. Nanowire growth is enabled by the precursor molecules in the surrounding gaseous environment, which supply growth materials to the nanowire via the nanoparticle. At the same time, the nanowire is being probed by an electron beam.

Cover illustration back: A poem about working with indium in the environmental transmission electron microscope, generated by my colleague Azemina Kraina through ChatGPT.

Funding information: The thesis work was financially supported by Vetenskapsrådet (VR).

Faculty of Science, Department of Chemistry

ISBN: 978-91-7422-974-5 (print)
ISBN: 978-91-7422-975-2 (pdf)

Printed in Sweden by Media-Tryck, Lund University, Lund 2023

Seeing is believing

Contents

List of publications

This thesis is based on the following publications, referred to by their Roman numerals:

I **Diameter Control of GaSb Nanowires Revealed by *In situ* Environmental Transmission Electron Microscopy**

M. Marnauza, **R. Sjökvist**, S. Lehmann, and K. A. Dick
The Journal of Physical Chemistry Letters, 2023, 14, 7404–7410

I cooperated with M. M. in project initiation, experimental investigation, data processing and writing of the manuscript.

II **Compositional Correlation between the Nanoparticle and the Growing Au-Assisted $In_xGa_{1-x}As$ Nanowire**

R. Sjökvist, D. Jacobsson, M. Tornberg, R. Wallenberg, E. D. Leshchenko, J. Johansson, and K. A. Dick
The Journal of Physical Chemistry Letters, 2021, 12, (31), pp. 7590-7595

I initiated and led the project, was main responsible in the experimental investigation and wrote the manuscript.

III **Ternary InGaAs Nanowire Composition Studied via *In-Situ* Transmission Electron Microscopy and Simulation**

R. Sjökvist, M. Tornberg, D. Jacobsson, and K. A. Dick
Manuscript

I initiated and led the project, was main responsible in the experimental and simulation-based investigation and wrote the manuscript.

IV ***In-situ* study of growth dynamics in Au-seeded GaSb nanowires**

R. Sjökvist, M. Marnauza, and K. A. Dick
Manuscript

I cooperated with M. M. in project initiation, experimental investigation, data processing and writing of the manuscript. I led the work on the simulation.

v **Direct Observations of Twin Formation Dynamics in Binary Semiconductors**

M. Tornberg, **R. Sjökvist**, K. Kumar, C. R. Andersen, C. B. Maliakkal, D. Jacobsson, and K. A. Dick
ACS Nanoscience Au, 2022, 2, (1), pp. 49-56

I assisted in the data analysis and writing of the manuscript.

vi **Observation of the Multilayer Growth Mode in Ternary InGaAs Nanowires**

R. Sjökvist, M. Tornberg, M. Marnauza, D. Jacobsson, and K. A. Dick
ACS Nanoscience Au, 2022, 2, (6), pp. 539-548

I initiated and led the project, was main responsible in the experimental investigation and wrote the manuscript.

Publications where I have contributed, but will not be discussed further in this thesis:

vii **Time-Resolved Compositional Mapping During In situ TEM Studies**

A. R. Persson, M. Tornberg, **R. Sjökvist**, and D. Jacobsson
Ultramicroscopy, 2021 222, 113193

Acknowledgements

Although thesis writing is something you mostly do on your own, the work presented here would not have been the same without the help, support and input from a number of people. Naturally, I will not be able to list all the names here, but I have tried to group people into categories where they can identify themselves. Know at least that I appreciate every single one of you and I am very grateful for all the support I have received.

I would like to start by thanking my supervisors, Kimberly, Martin and Daniel. In different ways you have all supported me throughout my PhD studies and made sure I have gotten the help I needed when I needed it. Daniel, you were with me in the lab from day one, and I have always appreciated your input and knowledge regarding the experimental parts of nanowire growth and microscopy. We have spent many hours at the microscope together, and I am sorry that so many of them consisted of us waiting and hoping to find perfect nanowires. Martin, your knowledge about microscopy, image simulation and post processing of microscopy data has been invaluable. My only regret is that I should have realized this sooner and incorporated it more into my projects. And finally Kimberly, thank you for giving me the freedom to explore and learn based on my interests, while still nudging me in the right directions. You have taught me many things, including the great importance of fika, as many of our scientific discussions have occurred in the polymat kitchen over a cup of coffee.

I would like to thank past and present group members for all the fun times, fika and interesting discussions we have had. The helpful, kind and relaxed culture within our group is something which I am proud of having been part of, and which I will absolutely miss. Although eating cake before lunch every Tuesday is likely not the best for your health, it definitely helps for morale. I am also happy that you have found yourself a replacement cake-cutter in Aidas, he will do a tremendous job!

Our group is heavily affiliated with nCHREM, and I would therefore like to extend a thank you to Crispin, Reine and Daniel for keeping it running, and to all the other people I have had the pleasure of discussing microscopy data with in the bunker. I would also like to take this opportunity to send a message to all ETEM users I have worked together with: I am sorry for insisting on supplying the heavily contaminating element In into the microscope all the time. But look at all the nice papers I was able to write!

I would like to especially thank some of the older PhD students, Marcus, Erik and Axel, who showed me the ropes and who taught me a lot during my first years of PhD studies. Equally important are the younger PhD students who arrived slightly after me, David, Mikelis and Tianyi, who I have had the pleasure of sharing an office with. Tianyi, you always manage to lift the moods up when times are tough, with your infectious laugh and eagerness to help out when there is a need. I always get excited when you pull up your

computer to show the latest ETEM results, since your videos are simply the coolest. David, it has been great to have someone not working with nanowires around, who can be a voice of reason regarding, for example, electron beam effects. Your written English might be archaic, and your constant sighing could drive a wind turbine, but I wouldn't have wanted it to be any other way. Mikelis, we have worked together tightly for several years now, and have managed to supervise two Master's students, get a research grant, travel to the US, and publish. The rapid and valuable exchange of thoughts and knowledge we have had has allowed me to learn and grow a lot over the last years, and I hope you can say the same. Nothing about my PhD studies would have been the same if I had had other office mates during these past years, so thank you all for the jokes and laughs, rants, help and support, gossip and very interesting discussions. I feel saddened that I will have to leave the tight gang that we have formed, but I am certain that you will have even more fun times in the future, with whoever replaces me in the office quartet.

The papers that I have had the pleasure of co-authoring have been shaped with the help of many capable researchers. Therefore, I give a special thank you to everyone I have worked together with on any paper. Sometimes, drafting a manuscript can be an arduous process, but it is important to remember that every little change implemented based on every comment is done to polish and improve the work, and leads to an overall much better end product.

As teaching is a large part of the PhD studies, I have had the opportunity of teaching basic and advanced courses in chemistry, materials science and electron microscopy. I would therefore like to thank everyone I have taught with, and also the PI:s responsible for those courses.

I would like to thank my friends and colleagues at CAS and polymat for the nice work culture at our division. The PhD network and the Feel Good Committee deserve a specific shout out for supplying help in the bureaucratic marsh that comes with a state governed institution, and for organizing barbecues, board game and movie nights and excursions.

Speaking of bureaucracy, thank you Maria and Sara for being such great administrative staff, I can't even count how many times you have helped me with a form, signature, reimbursement or booking. I would also like to thank Ola, my institutional representative, for his dedication to my individual study plan and my well-being, and for all the help regarding the administrative stuff of the thesis.

I also would like to thank my friends and colleagues affiliated with nanolund. The annual meetings and student retreats are always nice breaks during the fall, and have helped me getting more insight into what nano related research is being carried out throughout the university.

Before I started my PhD studies, I did my undergraduate studies here in Lund. I would

therefore like to thank the teachers and organizers of the Engineering Nanoscience program for providing an inspiring package of courses, and to my classmates for helping me reach my full potential. Without all of you, I might not even have pursued a PhD, so thank you. I am very happy that so many of my former classmates are still around for the occasional lunch, and of course that I can call so many of you close friends.

Since I have been around in Lund for quite some time, I have also made many friends in other environments than the undergraduate and graduate study programs, such as the different spex I have been involved with, and The Funktional Group. I am also extremely lucky to have retained many friends from before I moved to Lund. So thank you all for keeping me sane, and giving me something to think about that isn't nanowires!

The same goes for my family. Thank you everyone for always supporting me in my work, and for all the good times in Nässjö. Mom and dad, you have given me so much love and support over the years, and I couldn't be luckier to have you as my parents. Oliver and Tilda, we have always had each other's backs, and your achievements constantly inspire me to do my absolute best. One of the best parts about living in another city is to get to come home and get showered in love once in a while.

And finally, Linnea. Everyone said that we were crazy for writing our theses at the same time, but I think the fact that you and I huddled together in our tiny home office and wrote day and night was what in the end kept me sane throughout these months. I couldn't have done this without you, and I can't wait to see what our next adventure together will bring.

Popular summary in English

The basic concept that materials are constructed from tiny, "indivisible", building blocks was coined over 2000 years ago by Greek philosophers, where the word atom comes from the Greek word for indivisible, *atomos*. Our understanding has increased dramatically over the last few hundreds of years and we have succeeded in collecting, describing and grouping over a hundred different atomic species in the periodic table of the elements. We also know that atoms consists of protons, neutrons and electrons (which, in turn, consist of even smaller building blocks), which describe the type of atom, and to some extent how it will react with other atoms of different kinds. Millions of atoms join together in many cases to create different types of objects and materials, where the materials of focus in this thesis are crystals.

What is common between all crystals is that they, at the atomic level, have a clear periodic structure, even if there of course can be random defects and faults. Some crystals only consist of one kind of atom, like copper (Cu) or silicon (Si), that creates a specific three-dimensional pattern, so called crystal structure, based on how the atoms arrange themselves. Other crystals consist of two or more different atomic species, for examples table salt (sodium chloride, NaCl), where different atoms take specific positions in the crystal structure so that the crystal becomes stable.

Observation of crystal growth is in essence not difficult to achieve, as long as you know how to do it. There are, for example, crystal growth sets that can be bought in most toy stores. In this case, one would start with a piece of crystal submerged in water and add a powder that will dissolve, and over the next few days a crystal with nice facets will grow. The process is illustrated to the left in Figure 1. Even if the growth is comparably fast, it is likely too slow for us to perceive the changes by eye in real time. In order to observe the growth in real time a higher resolution is needed, since then much finer details can be seen. If one would break off a piece of crystal and place it in the powder solution in a light microscope one would have an easier time following the crystal growth, as the resolution and magnification would be increased compared to the bare eye. Despite this, one would still not be able to see the tiniest changes in the crystal, where singular atoms move from the liquid and attach to the solid crystal. In this case, more expensive and technologically advanced toys are needed.

In my work, I have observed the growth of semiconductor crystals, that consist of the elements indium (In), gallium (Ga), arsenic (As) and antimony (Sb) in different combinations, in real time at the atomic scale. For this I have used a transmission electron microscope, a microscope that uses electrons instead of light to illuminate the crystals. The electrons have a much shorter wavelength than light, which means that they can be used to image objects with much better resolution, allowing the atoms to be revealed. One condition is that the

sample has to be very thin, less than 100 nanometers. Electron microscopes are typically used to image different types of materials and to determine properties such as crystal structure, shape and composition. Usually, the samples are then situated in a vacuum, very low pressure, within the microscope and ideally they should not change while they are being observed. What is special about the microscope I have used is that one can both heat the samples and send in various gases, which means that the sample can be observed under real conditions where chemical reactions can take place.

Just as the case with the crystal growth set, one has to supply material (the powder) to grow the crystal. In my case, I send in a vapor of molecules that contain the atoms I want to incorporate in my crystal, where the molecules decompose and release the atoms when they reach the sample and are heated. The way my crystals grow is also a bit different. I use the vapor-liquid-solid (VLS) method to grow the solid crystals, where the material is delivered as a vapor and travels through a liquid nanoparticle. The resulting crystals are rod-like, where the diameter is determined by the size of the nanoparticle which is typically on the order of tens of nanometers, and they grow as long as one supplies growth materials. This type of structure is often referred to as a *nanowire*, and the shape makes its properties different than the same material in bulk form. The growth of nanowires in the microscope is illustrated to the right in Figure 1.

By studying the growth of nanowires *in-situ*, during growth, we can learn how different materials behave during growth and how we can affect them by changing vapor flow and temperature. We can, for example, study how the shape and composition changes based on the nanoparticle, and which conditions promote defect formation in the resulting crystal. All of these aspects will be discussed in this thesis. Ultimately, this study will be of benefit to other researchers that are trying to control crystal growth at the atomic scale, and the hope is that this will contribute to the development of better components based on semiconductors and nanowires.

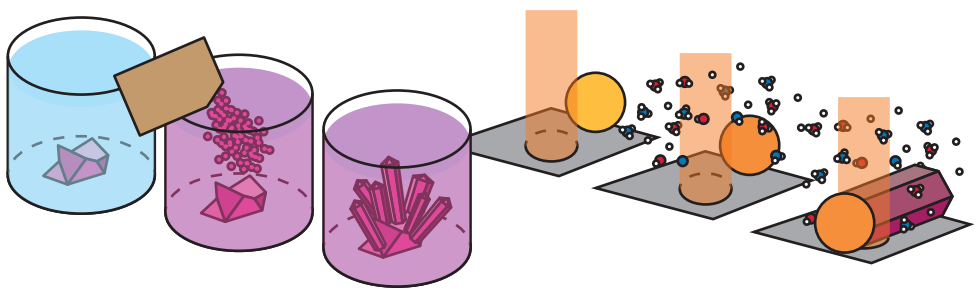

Figure 1: **English:** *Left:* The growth of a crystal from a commercial crystal growth kit for children. *Right:* The growth of a nanowire while it is being illuminated by an electron beam.
Svenska: *Vänster:* Växt av en kristall från kristallväxtkit för barn. *Höger:* En nanotråd som växer medan en elektronstråle träffar den.

Populärvetenskaplig sammanfattning på svenska

Det grundläggande konceptet att material ska vara uppbyggda av väldigt små, "odelbara", byggstenar myntades för långt över 2000 år sedan av grekiska filosofer, där ordet atom kommer från grekiskans ord för odelbar, *atomos*. Över de senaste få hundra åren har vår förståelse ökat drastiskt, och vi har lyckats samla, beskriva och gruppera över hundra olika atomslag i det periodiska systemet. Vi vet också att atomer består av protoner, neutroner och elektroner (som i sin tur består av ännu mindre byggstenar), som beskriver vilken typ av atom det är och till viss del hur den kommer att reagera med andra atomer av olika slag. I många fall sitter miljontals atomer ihop för att bilda olika typer av objekt och material, där kristaller är de material som står i centrum i den här avhandlingen.

Det som är gemensamt för alla kristaller är att de på atom-nivå har en tydlig periodisk struktur, även om det kan förekomma slumpmässigt placerade orenheter och fel. Vissa kristaller består bara av en typ av atomer, såsom koppar (Cu) eller kisel (Si), som bygger upp ett specifikt 3-dimensionellt mönster, så kallad kristallstruktur, baserat på hur atomerna arrangerar sig. Andra kristaller består av två eller fler olika atomslag, till exempel bordssalt (NaCl), där olika atomer upptar specifika positioner i kristallstrukturen för att kristallen ska bli stabil.

Att observera kristalltillväxt är egentligen inte så svårt, om man vet hur man ska göra. Till exempel finns det kristallväxtkit att köpa i de flesta leksaksaffärer. Där börjar man med en bit kristall i vatten, tillsätter ett pulver som löser sig, och över de närmsta dagarna växer kristallen och bildar fina facetter. Processen är illustrerad till vänster i Figure 1. Även om växten är förhållandesvis snabb, så är den troligen för långsam för att man ska kunna se förändringar i realtid på storleksskalan man kan observera med ögat. Om man vill observera kristalltillväxten i realtid så behövs det alltså högre upplösning, vilket betyder att man kan se detaljer som är mycket mindre. Om man bryter av en bit kristall och lägger i pulverlösningen under ett ljusmikroskop kommer man lättare kunna se och följa kristallens växt på mycket närmre håll än vad man kunde tidigare. Trots detta kommer man fortfarande inte se de absolut minsta förändringarna i kristallen, där enskilda atomer rör sig från vätskan och sätter sig på den fasta kristallen. För detta behövs betydligt dyrare och mer tekniskt avancerade leksaker.

I mitt arbete har jag observerat växten av halvledarkristaller, som består av ämnena indium (In), gallium (Ga), arsenik (As) och antimon (Sb) i olika kombinationer, i realtid på den atomära skalan. Till min hjälp har jag haft ett så kallat transmissionselektronmikroskop, ett mikroskop som använder elektroner istället för ljus för att avbilda kristallerna. Elektroner har en mycket mindre våglängd än ljus, vilket gör att man kan använda dem för att avbilda föremål med mycket bättre upplösning, så att man kan se atomerna. Ett kriterium är att provet måste vara väldigt tunnt, mindre än 100 nanometer. I vanliga fall används

elektronmikroskop för att avbilda olika typer av material och ta reda på egenskaper såsom kristallstruktur, form och komposition. Det genomgripande temat är att materialen då befinner sig i vakuum inne i mikroskopet, alltså väldigt låga tryck, och idealt inte ändrar sig medan man tittar på dem. Det speciella med mikroskopet jag har använt är att man både kan upphetta sina prover och skicka in olika gaser, så att man kan observera sina prover under verkliga förhållanden där kemiska reaktioner kan äga rum.

Precis som i fallet med kristallväxtkitet, så måste man tillsätta material (pulvret i exemplet) för att kunna växa sin kristall. I mitt fall skickar jag in molekyler i gasfas som innehåller de atomer jag vill inkorporera i min kristall, som bryts ner och lämnar ifrån sig atomen när de når provet och hettas upp. Sättet som mina kristaller växer på är också lite annorlunda. Jag använder den så kallade vapor-liquid-solid (VLS) metoden för att växa kristallerna (solid), där materialet kommer från gasfasen (vapor) och går via en flytande nanopartikel-droppe (liquid). Detta resulterar i att kristallerna får en avlång form, där diametern bestäms av droppens storlek, typiskt på skalan tiotals nanometer och växer så länge man skickar in mer material. Den här typen av strukturer kallas ofta för *nanotrådar* och formen gör att egenskaperna hos materialet blir annorlunda än när materialet är i bulkform. Växten av nanotrådar i mikroskopet är illustrerad till höger i Figure 1.

Genom att studera växten av nanotrådarna *in-situ*, medan de växer, kan vi lära oss mycket om hur olika material beter sig under växt och hur vi kan påverka dem genom att ändra gasflöden och temperatur. Vi kan till exempel studera hur form och komposition ändras baserat på nanopartikeln, och under vilka förhållanden vi bildar mer defekter i kristallen. Alla dessa aspekter kommer att tas upp i denna avhandling. Förhoppningen är att detta kommer vara till nytta för andra forskare som försöker kontrollera kristalltillväxt på den atomära skalan, utan att själva kunna studera den så som jag har gjort, och att detta kommer att bidra till att förbättra tillverkningen av komponenter baserade på halvledarmaterial och nanotrådar.

List of abbreviations and chemical compounds

Abbreviation	Introduced in
ADF - Annular Dark Field	Chapter 3.1.4
BF - Bright Field	Chapter 3.1.4
CCD - Charge Coupled Device	Chapter 3.1.4
CMOS - Complementary Metal–Oxide–Semiconductor	Chapter 3.1.4
DF - Dark Field	Chapter 3.1.4
DRP - Dry Rotation Pump	Chapter 3.2.2
EELS - Electron Energy Loss Spectroscopy	Chapter 3.1.5
ETEM - Environmental Transmission Electron Microscopy	Chapter 1
FEG - Field Emission Gun	Chapter 3.1.2
FFT - Fast Fourier Transform	Chapter 4.9
FPS - Frames Per Second	Chapter 6.1
GHS - Gas Handling System	Chapter 3.3
GPA - Geometric Phase Analysis	Chapter 4.10
HAADF - High Angle Annular Dark Field	Chapter 3.1.4
HRTEM - High-Resolution Transmission Electron Microscopy	Chapter 3.1.4
IP - Ion Pump	Chapter 3.2.1
MBE - Molecular Beam Epitaxy	Chapter 2.2
MEMS - MicroElectroMechanical System	Chapter 3.4
MFC - Mass Flow Controller	Chapter 2.2.1
MOCVD - Metal-Organic Chemical Vapor Deposition	Chapter 2.2
MOVPE - Metal-Organic Vapor Phase Epitaxy	Chapter 2.2
MV - Manual Valve	Chapter 3.3.1
PC - Pressure Controller	Chapter 3.3.1
PT - Pressure Transducer	Chapter 3.3.1
RGA - Residual Gas Analyzer	Chapter 3.2.2
SAG - Selective Area Growth	Chapter 2.2
SCCM - Standard Cubic Centimeters per Minute	Chapter 3.3.1
STEM - Scanning Transmission Electron Microscopy	Chapter 3.1.1
TEM - Transmission Electron Microscopy	Chapter 1
TMP - TurboMolecular Pump	Chapter 3.2.2
UHV - Ultra High Vacuum	Chapter 3.2.1
VLS - Vapor-Liquid-Solid	Chapter 2.2.1
VSS - Vapor-Solid-Solid	Chapter 2.2.1
WZ - Wurtzite	Chapter 2.1.2
XEDS - X-ray Energy Dispersive Spectroscopy	Chapter 3.1.5
ZB - Zincblende	Chapter 2.1.2

Chemical Compounds	Introduced in
AlGaAsSb - Aluminum Gallium Arsenide Antimonide	Chapter 2.1.1
AsH_3 - Arsine	Chapter 2.2.1
DMGa - Di Methyl Gallium	Chapter 3.3.2
GaAs - Gallium Arsenide	Chapter 2.1.1
GaN - Gallium Nitride	Chapter 2.1.2
GaSb - Gallium Antimonide	Chapter 2.4.4
InAs - Indium Arsenide	Chapter 2.4.4
InGaAs - Indium Gallium Arsenide	Chapter 2.1.1
InP - Indium Phosphide	Chapter 3.3.4
InSb - Indium Antimonide	Chapter 2.1.1
MMGa - Mono Methyl Gallium	Chapter 3.3.2
PH_3 - Phosphine	Chapter 3.3.1
SiN_x - Silicon Nitride	Chapter 2.4.2
TMAl - Tri Methyl Aluminum	Chapter 3.3.1
TMGa - Tri Methyl Gallium	Chapter 2.2.1
TMIn - Tri Methyl Indium	Chapter 3.3.1
TMSb - Tri Methyl Antimony	Chapter 3.3.1

Chapter 1

Introduction

The field of materials science is vast, combining knowledge from many different fields of science with the common goal of discovering, producing, analyzing, applying and combining materials. A specific topic in materials science is the exploration of nanostructures, where the small dimensions are of interest. The present text will focus on the growth and analysis of a particular type of nanostructure, the nanowire.

A nanowire is, in essence, a tiny crystal with high aspect ratio, where the diameter is typically on the order of tens of nanometers while the length can reach several microns. The specific nanowires that will be discussed in this thesis are Au-seeded III-V semiconductor nanowires, where the 'III-V' indicates that they consist of materials from group III and V of the periodic table of elements. The Au nanoparticle is typically liquid during growth, and is used to provide a preferential site for the nanowire to grow from. This gives the nanowires the appearance shown in Figure 1.1. So why would one want to study these nanosized crystals? To understand this, we will first discuss the properties of semiconductors.

One of the main characteristics of semiconductors is that they possess a band gap, an energy gap in the band structure, which the electrons need to overcome to induce conductance. This puts the electronic properties of semiconductors in between those of conductors (e.g. metals), which do not have any band gap, and insulators (e.g. ceramics), which have a band gap that is large and difficult to overcome. The relatively small bandgap of semiconductors allows the excitation of electrons to a higher energy band, where conduction is possible, with a high degree of control. It also allows electrons to relax to the original band, which can result in the emission of electromagnetic radiation. [1]

Due to its popularity as the main component in commercial solar cells, Si is likely the

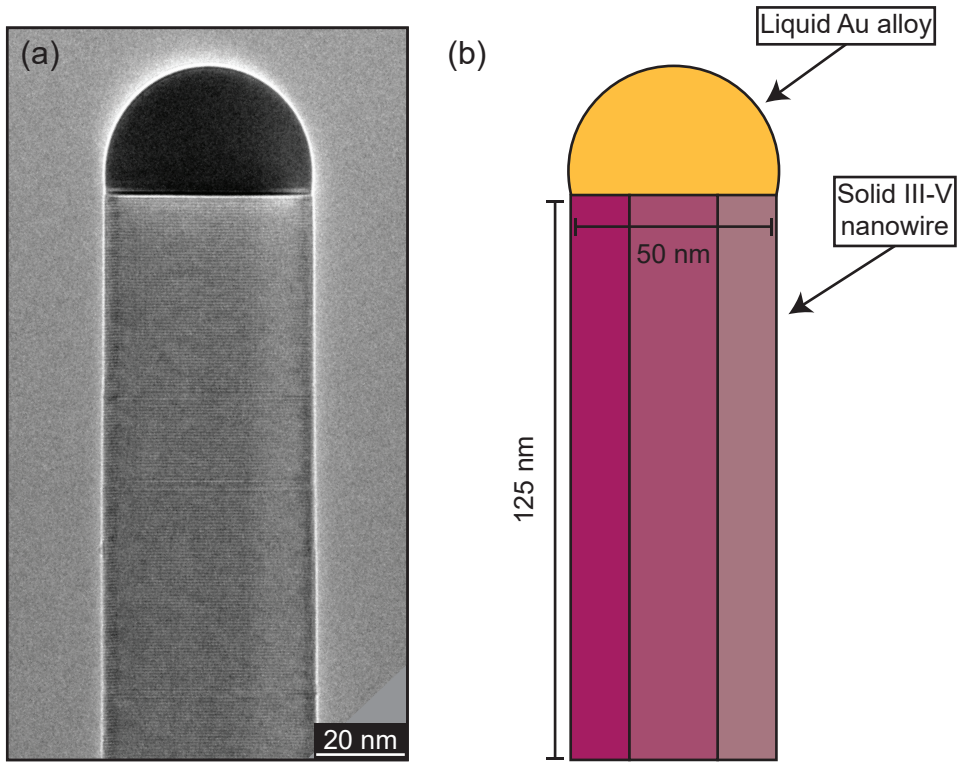

Figure 1.1: (a) An electron micrograph of a nanowire. (b) A schematic representation of the nanowire shown in (a), highlighting the nanoparticle, the solid nanowire and the dimensions. Note that the dimensions are only typical and might vary depending on how the nanowire was grown. In this case, the end of the nanowire is not depicted and extends several hundred nanometers outside of the figure.

most well-known semiconductor. Si has many strengths: it is abundant, sufficiently good at many things, and flexible in its properties. However, as will be discussed in more detail later, III-V materials, among others, can perform better in most applications where Si is used. An example of this is the computer chip industry, where Si has been replaced by other materials in many cases, in order to create smaller, faster and more energy efficient devices. [2]

The actual material is not the only aspect that matters when improving electronic devices. When approaching the nanoscale, the ratio between surface and bulk of the different materials will start to impact the overall properties to a larger degree, and may degrade the device performance. Morphology will then start to play a significant role, which is one of the reasons research on nanowires is promising. By, for example, changing the architecture of common electronic devices, such as transistors, from two-dimensional to three-dimensional, there is a possibility to achieve better control and to fit more computing power per unit area. This is achieved by growing nanowire heterostructures, segments of differ-

ent materials exhibiting specific properties along the nanowire axis, where each segment is controlled in length, composition and crystallinity. [3,4]

A large part of working with nanowires is related to fine-tuning the growth parameters so that such precise structures can be formed. In reality, the growth is plagued by a number of challenges including non-uniform diameter growth (tapering), change of growth direction (kinking), non-uniform length distributions and growth along the surface (creeping), all of which takes fine-tuning to get rid of. However, these are all aspects that can be easily observed with high statistical value directly after the growth, using quick and simple methods such as scanning electron microscopy. When growing more complex nanowire structures where, for example, heterostructures between different materials and compositionally precise ternary segments need to be formed, the investigation of the quality is more difficult. Here, more advanced techniques such as transmission electron microscopy (TEM) need to be utilized in order to unravel the outcome of the growth.

TEM has been heavily used to study a large range of different materials at the nanoscale, due to the versatility of the technique. By using electrons to image samples, information about crystallinity, crystal structure, composition, morphology, etc. can be found with relative ease and the possibility of atomic resolution. For nanowires, TEM has been used to determine such properties as the crystal phase purity, growth direction, axial and radial heterostructure sharpness and compositional distribution, to name a few. [5]

TEM is a continuously evolving technique, and increasingly more *in-situ* solutions have been made commercially available in recent times. *In-situ* is a broad term, which generally encompasses the recording of any process as it happens, typically under some sort of external input. The inputs can affect the environment of the sample, such as the temperature and surrounding medium (gaseous or liquid), or they can affect the sample through other means such as an electric bias or a probing laser beam. Sometimes, the former case is termed environmental transmission electron microscopy (ETEM) in order to make a distinction, and this is the type of setup that has been used for the work presented in this thesis. By supplying heat and growth materials to Au nanoparticles situated within the microscope, I have been able to observe the growth of nanowires under real, controllable, conditions.

The process of carefully adjusting growth parameters until the resulting nanowire structures are ideal is something all experimental nanowire growers are familiar with, and eventually the desired outcome is often achieved. However, even if the traditional way of growing nanowires gives a recipe for how to get the desired result, they cannot precisely show why the growth turned out the way it did. This highlights the strength of the *in-situ* investigations: being able to observe the growth as it happens gives unique insight into the atomic-scale processes that occur during the growth. By using techniques such as ETEM, the growth of nanowires can be observed and recorded in real time at the atomic scale, and data such as composition, growth rate, effect of material flows and temperature can be collected.

1.1 Aim of this thesis

This thesis is meant to describe how and why *in-situ* observation of nanowire growth is interesting, beneficial and important for expanding our understanding of the nanowire growth phenomenon. Chapter 2 is dedicated to the fundamental understanding of nanowires and how they grow. In Chapter 3, TEM is introduced, and we will compare traditional setups to the ETEM setup used throughout the work presented here. Methods and techniques we use to grow our nanowires *in-situ*, but also methods to analyze the resulting data, are discussed in Chapter 4. In Chapter 5, the influence the nanoparticle has on the nanowire in terms of morphology and composition is discussed, and results from **Paper I**, **II** and **III** are shown. In Chapter 6 the topic is layer growth dynamics in nanowires, where **Paper IV**, **V** and **VI** make the basis for the discussion.

Chapter 2

Semiconductor nanowires

In this chapter, we will discuss what nanowires are, what they are made of, and some examples of their intended usage. We will then move towards explaining the general principles of their growth from both an experimental and a theoretical point of view. The concept of combining different materials within the nanowire, creating ternary materials and heterostructures, will also be introduced.

2.1 Materials, properties and applications

In this section, III-V semiconductors will be discussed briefly, and their properties will be compared to those of Si. This will then be used to introduce applications of these materials. In the second half I will discuss the nanowire morphology and the properties of nanowires further, pointing out some benefits of growing III-V materials in this shape rather than as thin films.

2.1.1 A brief discussion on III-V semiconductor properties

As should be evident by now, the semiconductor materials within the nanowires that are the focus of this thesis are commonly referred to as III-V semiconductors. This is because their atomic lattice consists of pairs of elements from group III and V in the periodic table, forming stoichiometric compounds with a 1:1 ratio between the two groups. In that sense, the most basic III-V semiconductors consist of one element from each group, forming a binary compound, e.g. gallium arsenide (GaAs) or indium antimonide (InSb). These

Table 2.1: Some basic bulk parameters of Si and a few III-V semiconductors. a_0 is the lattice parameter in the cubic crystal structure presented and E_g is the bandgap energy. All values are found in reference [6].

Semiconductor	Crystal structure	a_0 [Å]	E_g [eV]	Bandgap type	Electron Mobility [$cm^2V^{-1}s^{-1}$]	Hole Mobility [$cm^2V^{-1}s^{-1}$]
Si	Diamond	5.431	1.12	Indirect	1400	450
GaAs	Zincblende	5.653	1.424	Direct	8500	400
InAs	Zincblende	6.058	0.354	Direct	40000	500
GaSb	Zincblende	6.096	0.726	Direct	3000	1000

binary compounds vary in their semiconducting properties, and a summary of some of these properties can be seen in Table 2.1, where they are presented in relation to those of Si. From Table 2.1 it can for example be seen that the III-V semiconductors presented all exhibit direct bandgaps, which means that, compared to Si, they are more suitable for light-emitting applications.[2] The magnitude of the bandgap relates to what energy photons can be absorbed or emitted by the semiconductor, and the electron and hole mobilites relate to the conducting capabilities of the semiconductor.

One way to tailor the properties of semiconductors is by incorporating trace amounts of elements from group II, IV or VI into the lattice, so called doping. The dopants will improve the conductance of the semiconductor by either contributing more holes or electrons that can be used as charge carriers, depending on the type of dopant added.[7] Another way to influence the properties is to exchange parts of the group III or V elements with other elements from the same group, forming ternary (e.g. indium gallium arsenide, $In_xGa_{1-x}As$) or quarternary (e.g. aluminum gallium arsenide antimonide $Al_xGa_{1-x}As_ySb_{1-y}$) compounds.*[8,9,10] This way, the properties of the semiconductor can be tailored beyond the properties of the pure binaries to fit exactly with the desired device application. The resulting properties will in most cases be a non-linear combination of the properties of the binary compounds. One property that to a good approximation changes linearly with composition is the lattice parameter, a_0, based on Vegard's law, shown in Equation 2.1.[7]

$$a_{A_xB_{1-x}} = xa_A + (1-x)a_B \tag{2.1}$$

In Equation 2.1, the lattice parameter of the compound, $a_{A_xB_{1-x}}$, varies based on the compositional relationship, x, between the lattice parameter of its constituents, a_A and a_B. Adjusting the lattice parameter of a semiconductor by instead growing a ternary compound can be used when forming semiconductor heterostructures. Heterostructure formation is the formation of a stacked structure of different semiconductors on top of each other, and is essential in the construction of advanced devices.[11,12,13] By lattice-matching the semiconductors to each other, essentially making the lattice parameters more similar, there is

*In these compounds, x and y are used to denote the composition. When no specific composition is discussed, they are often omitted for clarity.

a higher chance of achieving a heterostructure with good electronic properties.[14] This is because lattice mismatch is a common source of strain in the material and can eventually lead to the formation of defects that degrade the properties.[15]

Today, III-V semiconductors are already used in a wide range of applications such as integrated circuits, transistors, light-emitting diodes, lasers and high efficiency solar cells.[2] Their popularity in such a vast range of applications stems from the flexibility in their properties and performance. However, there are some limitations to the traditional thin film structure of semiconductor devices that lead to the exploration of the nanowire morphology for these materials. This will be the focus of the next section.

2.1.2 Properties and applications of nanowires

As was already mentioned in Chapter 1, nanowires are, in essence, nanostructures that are confined in two dimensions while elongated in the third. Typically, the diameters of nanowires are less than 100 nanometers, while the lengths can be several microns. When dimensions are decreased to such an extent that they become similar to the electron wavelength in the material, a quantum confinement effect arises, which affects the available energy levels for the electrons and therefore also the optical and electronic properties.[16] Nanowires are therefore often referred to as electronically one-dimensional materials. The small cross-section of nanowires also provides a strain-accommodating effect, where, if the area between two moderately lattice-mismatched materials is sufficiently small, the interface will be strained but often dislocation free.[17] This makes nanowires ideal materials for constructing heterostructures, as the electronic and optical properties will not be deteriorated by dislocations. The strain-accommodating properties have also allowed researchers to form short, axial segments of different materials with different band gaps in the nanowire structure, which can act as quantum dots, for example.[13,16]

In Table 2.1, it can be seen that all the listed III-V materials exhibit the zincblende (ZB) crystal structure, when in bulk form. ZB is the stable crystal structure for most of the bulk III-V semiconductors at ambient conditions, with the exception of the nitrides, e.g. gallium nitride (GaN), where the stable crystal structure is wurtzite (WZ). In the nanowire morphology, however, many of the III-V materials can be grown in the metastable WZ crystal structure instead.[18,19] For any of the III-V materials, the difference in the resulting properties of the two different crystal structures is significant, giving more flexibility in the choice of materials when growing nanowire-based structures.[20]

Many researchers grow nanowires with the goal of constructing a III-V semiconductor nanowire based device. The nanowire morphology allows for the construction of smaller or otherwise architecturally different devices in application where traditionally grown III-Vs already are in use. A few examples include: nanowire transistors,[3,4,21] light generation,[22,23]

light harvesting nanowire solar cells,[11,24] chemical and biological sensors[25] or for demonstration of exotic quantum phenomena (e.g. the majorana fermion).[26,27] Many of these devices require careful design, where atomic precision within the structure is needed, and a combination of the control of crystal structure, composition in ternary regions, sharpness of heterostructures and integration to other materials will determine the final device performance. For example, in tandem solar cells, different segments of III-V materials with different bandgaps are required to be able to collect a larger range of the solar spectrum, and all of these should be joined at atomically sharp heterostructures to ensure the proper functionality.[11,24] Similarly, several materials with different bandgaps are combined to create complex and highly efficient transistor designs.[28] To achieve such delicate device structure, the nanowires have to be grown using a growth method that provides sufficient control. Simultaneously, for the nanowire growth to be viable for application, there should also be significant throughput in terms of nanowires produced.[29] A discussion of different growth methods available will be the focus of the next section.

2.2 Growth methods

There are several methods of forming nanostructures with the nanowire morphology, but generally they can all be classified as either top-down or bottom-up synthesis methods. Top-down methods of forming nanowires involve the construction of a bulk piece of the material you would like to form nanowires of, and then selectively removing material until you are left with only the nanowires. While top-down approaches show strengths in position control and final nanostructure dimensions, they are also costly, as the process involves the production of a bulk sample with a thickness determined by the requirements from the final application. A lot of thought will also have to be spent on the etching method employed, so that it is selective, anisotropic and does not degrade the properties of the final nanowires. Finally, as discussed previously, III-V materials in bulk form are more limited in crystal structure and material combinations that do not produce dislocations at their heterostructures.[30]

Bottom-up approaches instead rely on different approaches to selectively grow nanostructures in the nanowire shape from the start, from a substrate. Bottom-up formation of nanowires encompasses several techniques with different advantages and disadvantages depending on the procedure, where many of the techniques useful for III-V nanowires are based on epitaxial matching with crystalline substrates. In epitaxy, there is a choice between using the same material as the intended nanowire growth (homoepitaxy) or a different material (heteroepitaxy), which will have implications on the epitaxial matching, resulting growth direction and cost.[7,31] In order to guide the growth so that the nanowire structure is achieved instead of a pure surface growth mode, an accumulating medium is used. Examples include masking the surface so that growth is concentrated in periodically placed

openings (so called selective area growth, SAG),[32] or using seed particles as accumulation and nucleation spots.[33] Seed particles can also either be placed periodically or randomly, depending on if an ordered array of nanowires is desired.[34]

In order to achieve growth of nanowires, material has to be supplied. The two most common methods are molecular beam epitaxy (MBE) and metal-organic vapor phase epitaxy (MOVPE), where MBE utilizes beams of atomic sources to deliver growth material, while MOVPE utilizes metal-organic and hydride precursor sources.[7] A more general term that encompasses MOVPE is metal-organic chemical vapor deposition (MOCVD), where the growth is not necessarily epitaxial, which is the case if the nanowires are grown in the vapor (aerotaxy)[35] or on amorphous substrates (e.g. the type of growth that stands as the basis for this thesis). In this thesis, the method employed to grow the nanowires is particle-assisted MOCVD, and as such that is the growth method that will be considered from now on.

2.2.1 MOCVD

MOCVD has for a long time been a standard technique for growing III-V semiconductors and other materials.[36] One of its main advantages over MBE is its high throughput, making it more viable for industry. The main parts of an MOCVD setup include a system for supplying gases and a reactor chamber wherein the growth will take place. The gas supplied depends on the intended growth, but in the case of III-V semiconductor nanowires, as mentioned earlier, the precursors are usually metal-organics and/or hydrides. Metal-organic sources consist of a metallic atomic species, which is bound to several organic ligands, as exemplified by tri methyl gallium (TMGa) in Figure 2.1 (a). Hydrides instead consist of an atomic species of interest bound by three H atoms, as exemplified by arsine, AsH_3, in Figure 2.1 (a). The metal-organic sources are stored in containers called bubblers, in the form of liquids or solid powders, and a carrier gas, commonly H_2, is used in order to vaporize and transport them to the reaction chamber. Hydrides, on the other hand, do not need to be carried with a carrier gas since they are stored in gaseous form. Conventional MOCVD operates at a high background pressure of H_2, ensuring few fluctuations and good stability of the growth environment within the chamber. A schematic of a typical MOCVD setup is shown in Figure 2.1 (b).

In the reaction chamber, the substrate is typically placed on a susceptor capable of heating the substrate. This enables the pyrolysis† of the precursors, so that they may release the atomic species of interest, and temperatures of several hundreds of degrees centigrade are needed for this process to be efficient. The elevated temperature also allows the atomic species to attain some degree of diffusion on the substrate, which is necessary if the pyrolysis happens far away from any nanoparticle. Although the nanoparticles act as collection sites

†Often referred to as "cracking".

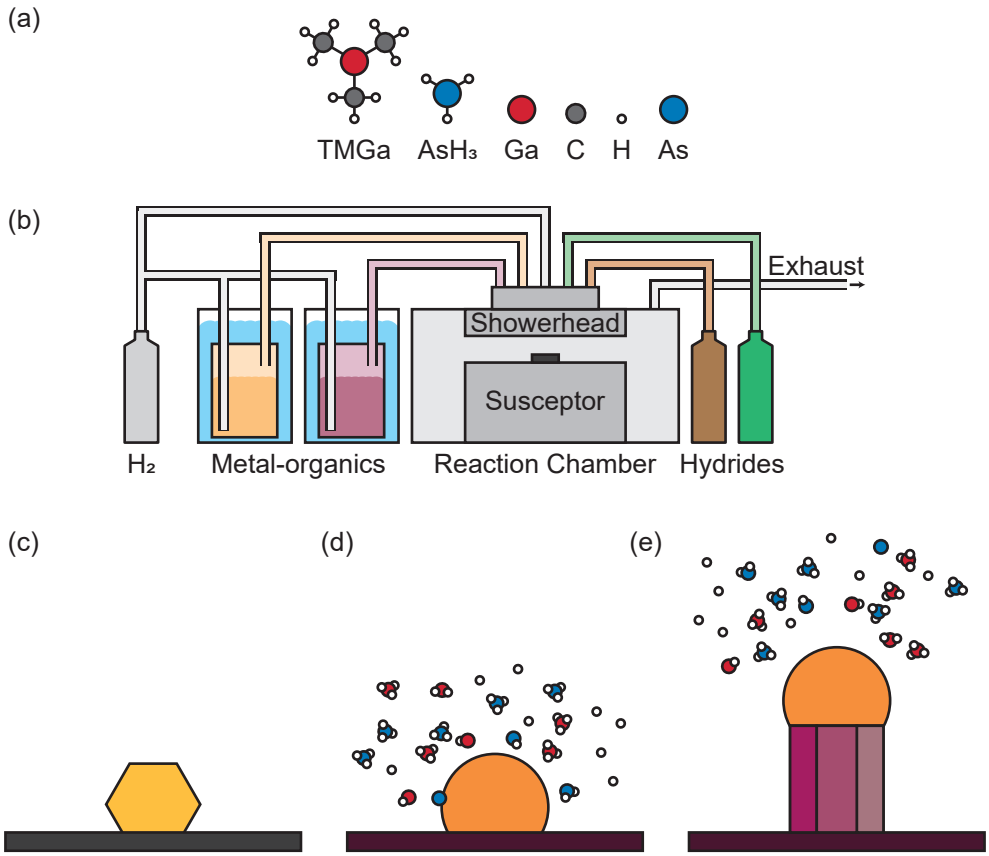

Figure 2.1: (a) A schematic representation of typical metal-organic (TMGa) and hydride sources (AsH_3), and their constituents. (b) A schematic of a typical MOCVD setup. The metal-organics are stored in bubblers, while the hydrides and H_2 are stored in gas-cylinders. In the reaction chamber, the sample (dark gray) is situated on a heated susceptor. The precursors and H_2 arrive at a showerhead from which the gas is supplied into the chamber. A vent line removes excess material and unwanted reaction products from the chamber. (c)-(e) the vapor-liquid-solid nanowire growth process, where (c) shows a solid nanoparticle on a substrate. In (d) the substrate is heated and precursors are supplied, allowing the nanoparticle to alloy with the growth species and become liquid. In (e) the epitaxial nanowire has formed, starting from the interface between the nanoparticle and the substrate.

for the supplied growth material during nanowire growth, there is often a certain degree of solidification directly onto the substrate, which will be a competing process and depends on the growth conditions. The temperature will also affect the phase of the nanoparticle, where it has been shown that having the nanoparticle in the liquid state is often beneficial. This sort of growth is referred to as vapor-liquid-solid (VLS) growth of nanowires and is detailed in Figure 2.1 (c)-(e). VLS, compared to vapor-solid-solid (VSS) where the nanoparticle is in a solid state, often proceeds faster and gives a more controlled growth.[37] For epitaxial, crystalline substrates, the nanoparticle also typically alloys slightly with the substrate, leading to an increased preference for the resulting nanowire to grow in the vertical direction.

When supplying the growth material into the chamber, the controlled flow of the individual precursors are typically set by mass flow controllers (MFC). A flow into a chamber may not accurately translate between different setups, since the material delivery to the actual substrate depends on the chamber geometry. It is therefore beneficial to instead measure the internal pressure in the chamber and report the supplied material as partial pressures instead. That being said, growth conditions are not typically directly translatable between different setups, although general trends in the resulting growth can be comparable. When performing a study of the growth conditions, a good way to ensure that the properties studied can be presented on a common axis is to use the V/III ratio, the ratio between the amount of group V and group III precursor, when reporting the data. As the amount of group V element supplied is often much larger than the amount of group III element (up to several thousands of times more), but can also be on a similar level, this gives a scale for the ratio without having to report the pressures separately. This can be especially convenient when performing growth series, where the flow of either precursor is held constant. Such V/III ratios will be frequently used later in this thesis.

Now that we have some idea about what to do experimentally to get the nanowires growing, it is time to have a look at the theoretical considerations of nanowire growth, starting with the concept of nucleation.

2.3 Basics of nucleation

The concept of equilibrium is something encountered on a daily basis, whether consciously or not. A pendulum set in motion will eventually stop and rest in a position straight down from its anchor point. In this case, the surrounding forces acting on the pendulum will eventually cause it to lose the momentum that it was given at the beginning of the experiment. However, if we continually push on the pendulum, we can force it to keep on swinging in its effort to reach the equilibrium state. Crystal growth is not so different in this regard. In order to facilitate the growth of a crystal from a liquid or vapor phase, we have to push the system out of equilibrium and make sure that the system can minimize its internal energy by forming a solid crystalline phase. In nanowire growth, we continually supply growth material (similarly to continuously pushing the pendulum) to the vapor phase in order to force the growth of the solid nanowire (keeping the pendulum in motion). The idea of constantly supplying material so that the nanowire continues growing at a stable rate is commonly referred to as steady-state growth, as will be discussed later. Instead of pushing with a physical force (as in the pendulum example), we here push on the system with a thermodynamic driving force, which will be the main concept of this section.

2.3.1 Thermodynamic background

In a simplified way, the concept of equilibrium of a system can be thought of as a state in which the free energy of the system is at a minimum. The system as a whole will contain a certain number of chemically active species, often referred to as components, which can be present in a certain number of different phases. Taking a simplified version of the growth of a Au seeded GaAs nanowire as an example, there would be four components (Ga, As, Au and GaAs) that are present to various degrees in three phases (vapor, liquid and solid). Each component that exists in each phase is contributing to the total energy of the system, depending on their concentration and the temperature. When growing nanowires, the energy of the system is often expressed using Gibbs free energy, G, which describes the free energy of the system at constant pressure and temperature.‡ The total Gibbs free energy of a system is found by adding all the contributions from the components in all the phases presented above. However, the absolute value of G is not of practical use, it is rather the change in G, or ΔG, that arises when e.g. components are transferred between the different phases that determines the way the driving force will push the system, as will be further discussed throughout this section. [38]

Associated with each component i in each phase is a chemical potential, μ_i, defined as the derivative of G with respect to the amount of the component, n_i, at constant temperature, pressure and amount of other components, according to Equation 2.2.

$$\mu_i \equiv \left(\frac{\delta G}{\delta n_i}\right)\Big|_{T,P,n_{j\neq i}} \tag{2.2}$$

The chemical potentials can be used to calculate a chemical potential difference, $\Delta\mu$, which corresponds to a driving force for material to move between phases, as shown in Equation 2.3.

$$\Delta\mu_i^{\alpha\rightarrow\beta} = \mu_i^{\alpha} - \mu_i^{\beta} \tag{2.3}$$

If Equation 2.3 results in a positive value, there is a driving force for component i to move from phase α to phase β. In the case of nanowire growth, where the nanowire consists of binary pairs of group III and V elements, the equation of the driving force for solidification has to involve the chemical potential of both elements in the liquid as compared to the chemical potential of the solidified atomic pair, shown for the formation of InAs in Equation 2.4.

‡This is of course a simplification, although very useful when describing chemical reactions.

$$\Delta\mu_{InAs}^{l\rightarrow s} = \mu_{In}^{l} + \mu_{As}^{l} - \mu_{InAs}^{s} \tag{2.4}$$

The chemical potential difference in Equation 2.4 we here define as the supersaturation of In and As in the liquid phase, as compared to solidified InAs. The concept of supersaturation can give a direct indication whether or not there is a driving force for solidification from the liquid phase, and will frequently be referred to in the later chapters.

The contribution to the total Gibbs free energy for stoichiometric solid phases can be readily computed based on temperature alone, where the parameters necessary for the computation can be found in tables for empirically determined thermodynamic data.[39] For liquids, gases and other non-stoichiometric phases, finding the contribution to Gibbs free energy of an element in the phase becomes more complex, as the mixing of species is associated with additional energy terms. As the number of components increases in a phase, higher order interaction parameters can be considered for a more complete expression of the free energy.§

2.3.2 Classical nucleation theory

In this section we will discuss the formation of a stable nucleus from the perspective of classical nucleation theory.[7,40] In order for nucleation to occur, there needs to exist a phase that is supersaturated with material. The first case we will be discussing is that of an isolated vapor, where the nucleus will be a liquid droplet.

If a supersaturation between the vapor phase with respect to the liquid phase is assumed, there is a thermodynamic driving force to nucleate a liquid droplet. However, forming a droplet also involves the creation of an interface between the liquid and solid phase. Therefore, there will be two factors contributing to the change in Gibbs free energy during nucleation, shown in Equation 2.5.

$$\Delta G = \Delta G_V + \Delta G_S \tag{2.5}$$

In Equation 2.5, the first term refers to the volume contribution of the nucleus, while the second term is related to the surface of the nucleus. Since the vapor is supersaturated, forming the bulk of the nucleus will involve a decrease of Gibbs free energy, meaning that ΔG_V will be negative. However, the formation of any surface always leads to an increase in energy, due to the abrupt change in environment the atoms at the surface experience. As objects become smaller, their surface to volume ratio increases, which means that for a very small nucleus the surface term can dominate and make it more favorable for the nucleus to dissociate again. Eventually, if a nucleus manages to grow large enough, the volume term

§That is, if they can be found in literature, which is not always possible.

will start to dominate, and growing the nucleus will be favorable. For the simplest case of a spherical droplet formed in a vapor with no surfaces present, as shown in Figure 2.2 (a) and (b), the equation for Gibbs free energy looks like this:

$$\Delta G(r) = \Delta G_V + \Delta G_S = -\frac{4\pi r^3}{3}\frac{\Delta\mu}{\Omega_L} + 4\pi r^2\gamma \tag{2.6}$$

Since the formation of a spherical nucleus is considered in Equation 2.6, ΔG is given as a function of the radius of the sphere, r. In the first term, which represents the reduction in Gibbs free energy upon forming the volume part of the nucleus, we also find the supersaturation, $\Delta\mu$, and the volume of the monomers that the nucleus consists of, Ω_L.¶ Dividing by Ω_L results in a final expression in number of monomers, that is then multiplied by the supersaturation (which is expressed in chemical potential difference per monomer in vapor versus liquid, in this case). The second term in Equation 2.6 represents the increase in Gibbs free energy resulting from the formation of the surface of the nucleus, which in this case consists of the standard expression for the surface area of a sphere multiplied by the surface energy (or more commonly named the surface tension for liquids), γ, expressed in energy per unit area. As the radius increases, both terms increase in magnitude. The important difference is that for a very small nucleus, the surface area to volume ratio will be large, which results in a positive Gibbs free energy for forming the cluster. Therefore, a sufficiently large cluster needs to form for it to be stable, and at this point the continued growth of the nucleus will be favorable. The critical point where the trend changes, i.e. where the derivative of Gibbs energy is equal to 0 with regards to further addition of monomers, indicates the smallest stable cluster size for the system. In the case of a spherical cluster, this is easiest expressed as a critical radius, r^*, as denoted in Figure 2.2 (c), where a typical curve of ΔG and the contribution from both the terms in Equation 2.6 are drawn. Beyond this size, further additions stabilize the cluster and the system can lower its free energy by growing the nucleus. The simple example shown in Figure 2.2 (c) assumes a constant supersaturation as the nucleus grows, which is a simplification. In reality, the supersaturation would change constantly as material is being transferred to the growing liquid phase (a change that is negligible if the volume of the vapor phase is large).

We can increase the complexity of the nucleation by introducing a substrate surface that is also present in the vapor, as shown in Figure 2.3 (a). A surface present in a supersaturated ambient phase will often act as a preferential site for nucleation, since the surface can act to minimize the energy barrier for nucleation. Nucleation on a substrate involves both the formation of an interface to the vapor phase, but also the formation of an interface between the nucleus and the substrate. At the same time, the already existing interface between the vapor and the substrate is diminished, which is a negative energy contribution to Gibbs free energy. For an isotropic nucleus, the surface energies of the different interfaces are related

¶The "monomer" in the case of nanowire growth would be an elemental III-V pair, such as a GaAs pair.

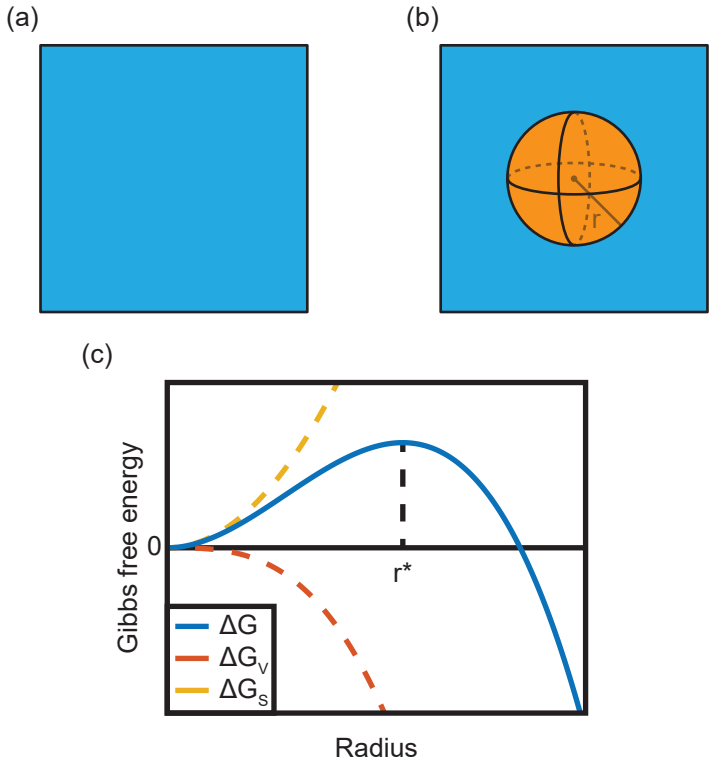

Figure 2.2: (a) Schematic illustration of an infinite vapor phase without walls or borders (you might have to use your imagination for this one). (b) A liquid nucleus with radius r has formed in the supersaturated infinite vapor phase. (c) A schematic representation of the difference in Gibbs free energy as a function of radius, along with the volume associated term and the surface associated term. The critical radius for stable growth, r^* is marked in the graph.

through the Young equation, where the forces resulting from the surface energies give the nucleus a specific shape:

$$\gamma_{sv} = \gamma_{ns} + \gamma_{nv} cos\theta \tag{2.7}$$

In Equation 2.7 the surface energies, γ, of the different interfaces (n = nucleus, s = substrate, v = vapor) are related through the wetting angle, θ of the nucleus. Depending on the surface energy balance presented in Equation 2.7 the nucleus will be wetting (wanting to maximize the interface to the substrate, θ is small) or non-wetting (wanting to maximize the interface to the vapor phase, θ is large). Examples of how the surface energies affect the wetting angle, and therefore the droplet shape, are schematically shown in Figure 2.4.

The total Gibbs free energy for forming an isotropic nucleus at the substrate, based on Equation 2.5, becomes:

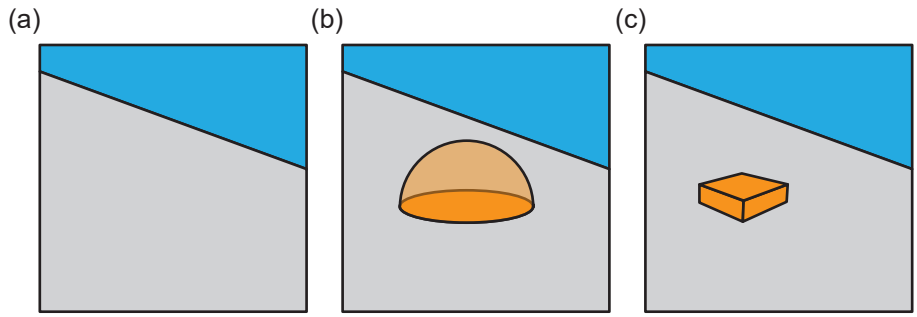

Figure 2.3: (a) A supersaturated vapor phase, now with a substrate surface present. (b) An isotropic nucleus has formed at the substrate-vapor interface. (c) An anisotropic nucleus has formed at the substrate-vapor interface.

$$\Delta G = V\frac{\Delta\mu}{\Omega} + A_{nv}\gamma_{nv} + A_{sv}\gamma_{sv} + A_{ns}\gamma_{ns} \tag{2.8}$$

In Equation 2.8, similarly to Equations 2.5 and 2.6 the first term is related to the formation of the volume of the nucleus and the rest of the terms are related to the creation and removal of the different surfaces. The formation of the bulk and removal of part of the substrate-vapor interface contribute to a lowering of Gibbs free energy.

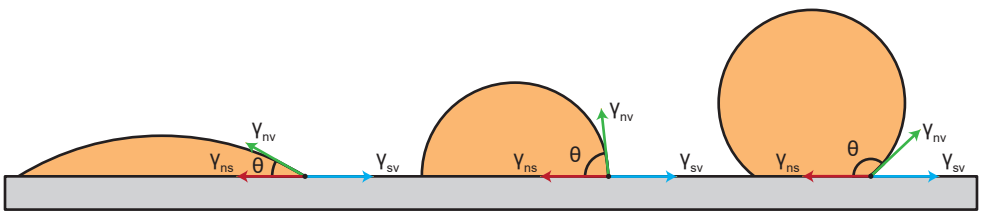

Figure 2.4: Schematic representation of nuclei with increasing wetting angle from left to right.

When a solid material nucleates it will eventually develop facets, as shown in Figure 2.3 (c). Higher energy surfaces tend to grow faster, which in bulk results in the formation of an equilibrium shape. Although the concept of a smallest amount of atoms that can be said to form a facet is an interesting discussion point in itself, it can sometimes be beneficial to assume that the nucleus has an unchanging faceted shape during its expansion. By further generalizing Equation 2.8 to make it more look like the simple expression for Gibbs free energy presented in Equation 2.5, we can express the formation of a nucleus with different facets, that may have different surface energies associated with them:

$$\Delta G = \frac{V}{\Omega}\Delta\mu + \sum_j A_j\gamma_j \tag{2.9}$$

In Equation 2.9 we keep the volume term from Equation 2.8, but lump all the formed or removed surfaces together into one sum term. This takes into account all different facets and interfaces that are formed during the nucleation.

2.3.3 Kinetics

While the thermodynamics outlined throughout this chapter gives the framework that can be used to determine which phase is the most stable and where material needs to go to minimize the energy of a system, it does not fully explain the rates of the processes involved. For this it is necessary to consider the kinetics of the system, which can be used to identify rates of processes such as chemical reactions or atomic attachments. Precursor pyrolysis, adatom diffusion, arrival (evaporation) of atoms to (from) the nanoparticle, nucleation and atomic attachment to a nucleus are all processes relevant to nanowire growth that can be described using rates. In many cases, kinetics and thermodynamics are used in tandem to give a more complete picture of the nanowire growth, as will be discussed in more detail in Chapter 5 and 6.

2.4 Nucleation and growth of nanowires

In this section, the concepts outlined in the previous section will be used to describe the nucleation and continued growth of semiconductor nanowires. The VLS growth, first described by Wagner and Ellis,[41] and introduced earlier, will form the basis of the discussion. The differences between the formation of the initial nucleus, and the continuous growth found after the nanowire and nanoparticle have stabilized, will be discussed. Finally, the growth dynamics and crystal structures of nanowires will be described in more detail. First, however, the seed particle must be considered.

2.4.1 A few notes on the seed particle

Nanowire growth from seed particles is a popular and relatively easy method, used since the research on nanowires began to accelerate.[42] Nanoparticles provide a preferential site for nucleation, if the growth conditions are favorable, which promotes axial growth. Au seed nanoparticles are, for example, by far the most popular nanoparticles to use, since the noble Au does not get incorporated into the solid III-Vs to any large extent, and the growth is in general simple compared to the alternatives.[43,44] However, Au is avoided in the Si industry, since it creates deep level traps in the bandgap of Si, deteriorating its properties.[45, 46] Nonetheless, for studying the growth processes, it works very well, and that is why Au has been used as seed particle for all the studies included in this thesis.

A common trend for Au-seeded nanowire growth is that the group V elements alloy to a very low extent, while the group III elements alloy readily with the seed particle. A combination of *ex-situ* studies of nanowires post-growth, solubility calculations, and growth models, have shown that As and P alloy in quantities less than 1 at.%, Sb alloys in slightly higher amounts (<5 at.%), while Ga and In alloy by tens of at.% in Au, during growth.[47,48] However, *in-situ* experiments provide the possibility of measuring the composition of the nanoparticle directly during growth, giving a method to confirm these predictions.[49] This will be discussed later on in the thesis.

2.4.2 Forming the initial nucleus

Before nucleation, the nanowire growth system consists of a liquid nanoparticle resting on a substrate surrounded by an ambient vapor, as shown schematically in Figure 2.5 (a). This means that before nucleation we already have three different phases of material present in the system. In order for growth material to be dissolved into the nanoparticle, there needs to be a supersaturation between the vapor phase and the liquid phase, creating a driving force for the material to be accumulated by the nanoparticles. At the same time, there should not be a driving force for forming solid islands straight onto the substrate, since then surface growth would be favored.[50] When material is sufficiently dissolved into the nanoparticle, there will be a supersaturation** with respect to forming the solid material, and a nucleus will eventually form as shown in Figure 2.5 (b). The nucleus will then ideally grow to cover the entire interface between the nanoparticle and the substrate, see Figure 2.5 (c), eventually lifting the nanoparticle to initiate the formation of a vertically aligned nanowire structure, Figure 2.5 (d).

The situation described in Figure 2.5 (a) and (b) is vastly simplified for a number of reasons. For one, if the nanowire growth is carried out through conventional, epitaxial, MOCVD there is usually an annealing step included before the growth is initiated, in order to improve the yield of vertically aligned nanowires and to remove surface contaminants.[51] During this step, the system will be elevated to high temperatures, leading to some degree of alloying between the nanoparticle and the substrate.[52] This is especially common if the nanowire to be grown consists of the same materials as the substrate. The alloying with the substrate will create an etch-pit, which can help in promoting the growth in the vertical direction.[53] If instead the nanowire is grown on an amorphous substrate, as is the case for the nanowires grown in this thesis, an annealing step is not necessary, since the nanoparticle is not dissolving the substrate. The wetting of the nanoparticle in this case is also less than for epitaxial growth, and there seems to be less prevalence for the resulting nanowire structure to form

**When discussing nanowire growth, the reader will realize that the nanoparticle is often referred to as being supersaturated with respect to the solid, which is a sloppy, but convenient, way of saying that the there is a supersaturation between the relevant dissolved species in the liquid nanoparticle, as compared to the compound they form in the solid.

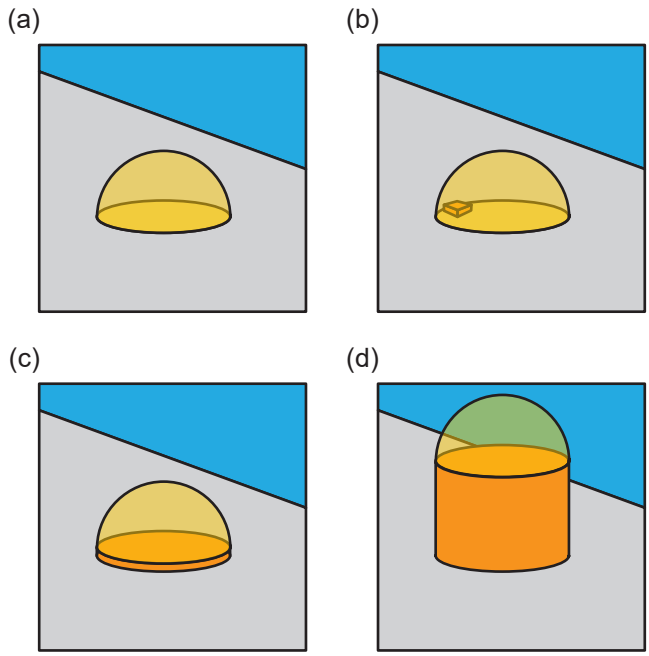

Figure 2.5: (a) A liquid seed particle residing on a substrate surface. (b) A nucleus has formed within the droplet, at the substrate-droplet interface. (c) The nucleus has grown to cover the whole interface. (d) The nanowire has started to grow vertically from the surface.

an interface to the substrate. The formation of an initial nucleus on an amorphous substrate involves rapid growth of material while the nanoparticle decides which facets to wet based on relations similar to those presented in Equation 2.7.[54] The nucleation of nanowires on amorphous silicon nitride (SiN_x) will be further discussed in a Chapter 4.

2.4.3 Layer growth dynamics

After nucleation and the subsequent stabilization of the system, axial growth of the nanowire ideally commences. Early theoretical models predicted that stable nanowire growth proceeds through a layer-by-layer growth process, where bilayers of the group III and V elements form at the interface between the nanoparticle and nanowire.[55] This process would then occur through atomic attachment of one bilayer at a time, with only one active nucleus at any time. The "flatness" of the nucleus (a singular bilayer of III-V pairs) has to do with the wetting of the "substrate" (the nanowire), promoting a small wetting angle according to the Young equation shown earlier in Equation 2.7. For the lack of polynucleation, the argument is that the limited volume of the nanoparticle and low solubility of the group V elements make the supersaturation change drastically during the nucleation

event.[56] Simultaneously, the newly formed nucleus will act as a preferential site for continued attachment, further depleting the nanoparticle. As a result, the nanoparticle is not sufficiently supersaturated with respect to the solid phase to overcome the nucleation barrier once a stable nucleus has formed, and only one nucleus is therefore present at a time.[57] The supersaturation will also dictate the growth of the formed nucleus as it expands as a layer across the liquid-solid interface, where continued supply of growth material might be needed in order for the layer to finish and completely cover the interface.

After a layer has grown to completion, the nanoparticle is in a depleted state, and must acquire more material in order to increase its supersaturation again. Eventually, a new nucleus will form and the cycle repeats. This cyclic process has been confirmed to be the mode in which several common III-V nanowire materials grow, through *in-situ* TEM investigations (more on that in Chapter 6).[58] In these investigations, the time from nucleation to layer completion is often termed the step-flow (or step-propagation or layer completion) time, while the time the nanoparticle spends collecting material after a layer is completed is called the incubation time. This process is shown schematically in Figure 2.6, going from nucleation, (a), to layer-propagation, (a)-(d), and finally incubation, (d) back to (a).

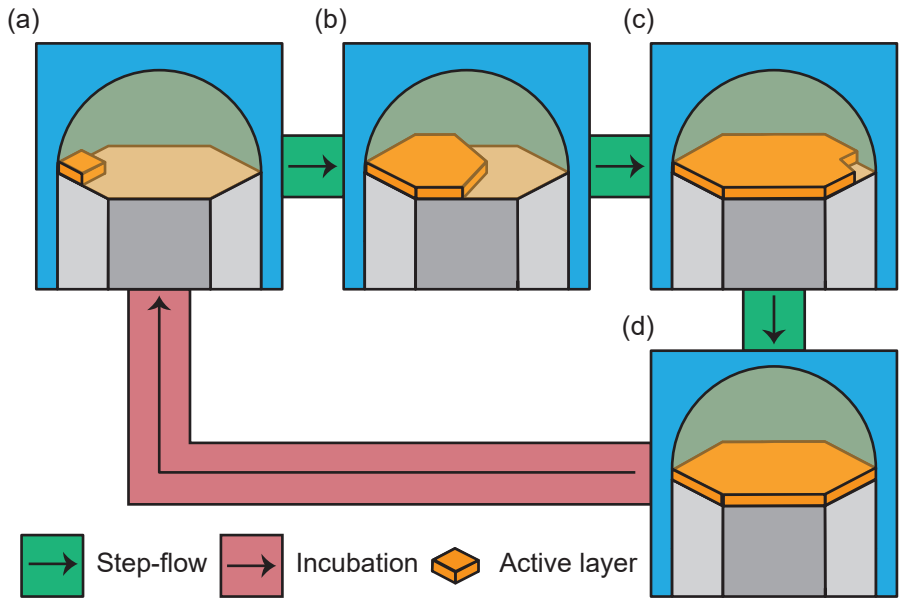

Figure 2.6: The layer-by-layer growth dynamics detailed schematically, and shown for the individual processes step-flow and incubation. (a) The nanowire, where a nucleus has just formed at the interface between nanoparticle and nanowire. (b)-(d) The nucleus is spreading to eventually cover the entire interface between nanoparticle and nanowire. From the nucleation event in (a) to the layer completion in (d) the layer proceeds during what is called the step-flow. After the layer has covered the whole interface, incubation starts, where there is a delay before the next nucleation occurs, and the cycle repeats.

As long as the nanowire continues to grow in the same crystal structure and the same direc-

tion, the nucleation of the individual layers will be straightforward. Since the nucleus and the rest of the nanowire consists of the same material, there is no surface energy between the nucleus and "substrate". Hence, the nuclei will form and spread across the interface between nanoparticle and nanowire at a more or less steady rate for steady growth conditions. This type of growth is often termed "steady-state" since we continuously push the system out of equilibrium conditions by supplying more material, causing the system to solidify material as a means of again reducing its energy, towards equilibrium. By keeping a steady material supply through the vapor, which leads to a steady material solidification, this enables the steady-state growth away from equilibrium.[50] Later, we will discuss what can happen when the surrounding growth conditions are changed, and how the system finds its way back to steady-state growth.

2.4.4 Crystal structures

As mentioned earlier, the most stable crystal structure at ambient conditions for the III-V materials that are the focus of this thesis is the ZB crystal structure. However, GaAs and indium arsenide (InAs) are examples of III-V materials that can also be grown in the WZ crystal structure, when the crystals are grown in the nanowire shape.[59,60] Theoretical models have proposed that the energy of formation for the two crystal structures is sufficiently similar, and that the supersaturation between the dissolved species in the nanoparticle and the solid material can affect which polytype forms.[61] Typically, there are clear trends in the formation of either polytype based on the growth conditions used, where even higher order polytypes can be found under specific conditions.[19] However, for certain III-V nanowire materials, the controlled formation of the WZ crystal structure has been difficult to achieve. One such material is gallium antimonide (GaSb), where it is speculated that the less ionic nature of the compound, as compared to, for example, the III-As compounds, is affecting its ability to form stacking faults and the WZ polytype.[62,63,64]

Figure 2.7 (a) shows a schematic of a nanowire heterostructure consisting of a segment each of GaAs WZ (Figure 2.7 (b), (c)) and GaAs ZB (Figure 2.7 (d), (e)). The crystal structures are schematically drawn and imaged in a specific viewing direction, in order to reflect the most commonly observed growth direction of III-V nanowires (the $[\bar{1}\bar{1}\bar{1}]$ direction in ZB and the [0001] direction in WZ), as well as illustrating a viewing direction where clear differences can be seen between the two. WZ exhibits an "ABAB" stacking sequence in the growth direction presented here, which means that the structure consists of two alternating layers that differ in atomic positions. Similarly, ZB has three different layers, producing an "ABCABC" stacking sequence. The difference in stacking is also shown along the nanowire axis in Figure 2.7 (f). The crystal can locally contain a deviation from this stacking sequence, producing e.g. "ABCBCABC". This would be termed a stacking fault or stacking defect. Another type of deviation is crystallographic twins in ZB, producing

a stacking sequence “ABCBACBA”. The twinned segment produced is crystallographically the same as the original ZB segment, only twisted by 60 degrees around the axial direction of the crystal.

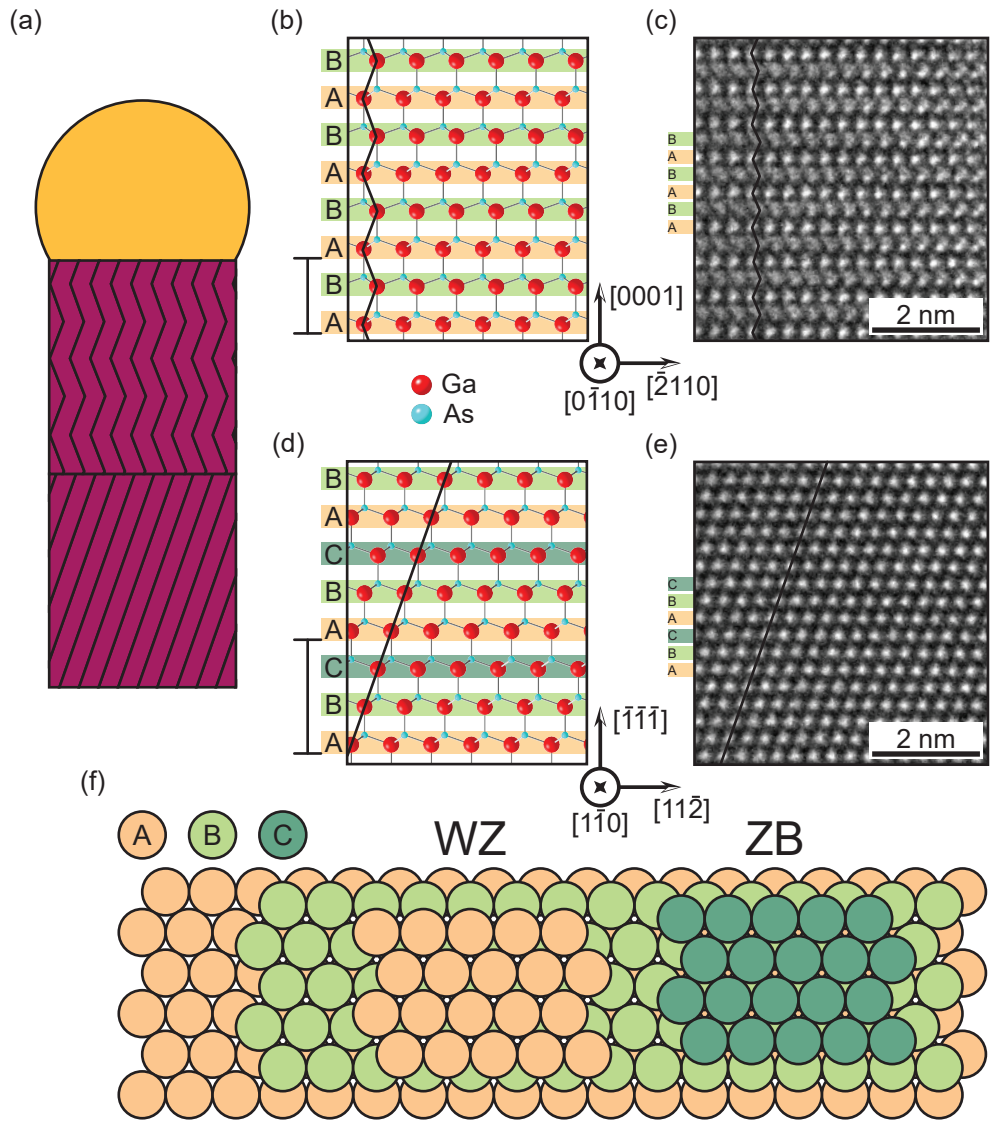

Figure 2.7: (a) A schematic of a nanowire, which consists of a WZ segment (top) and a ZB segment (bottom). The nanowire is drawn to be growing in the [0001] direction in WZ and the [$\bar{1}\bar{1}\bar{1}$] direction in ZB, which are the most common experimentally observed growth directions for semiconductor nanowires. Drawn crystals (CrystalMaker) are shown for WZ (b) and ZB (d), while micrographs depicting the same structures are shown in (c) and (e), respectively. The black lines in (b)-(e) are guides for the eye. The viewing direction is chosen so that the difference between the two structures is clearly seen, where the stacking order has been marked with letters A-C in panels (b)-(e). (f) The close-packed stacking of the two crystal structures, as seen along the nanowire growth direction.

In most relevant cases, where good control of the growth of the nanowire is achieved and the epitaxial matching with the substrate is not used to influence the nanowire, the nanowire grows in the $[\bar{1}\bar{1}\bar{1}]$ direction in ZB or the [0001] direction if the crystal structure is WZ, as illustrated in Figure 2.7. A clear example where this has been demonstrated is when the nanowires have been grown through aerotaxy, which is a method of growth that does not involve a growth substrate. It has been demonstrated that 99% of the nanowires grown through aerotaxy adopt the ZB crystal structure, with the $[\bar{1}\bar{1}\bar{1}]$ growth direction.[35] That being said, nanowires can in many cases be forced to grow in other growth directions through epitaxial matching with the substrate.[34]

2.4.5 Heterostructure formation and ternary growth

As has already been mentioned, the possibility of forming heterostructures with relative ease is one of the core strengths of nanowire growth. The simplest case is when a purely crystallographic heterostructure is formed, for example as a segment of WZ in a ZB GaAs nanowire. Typically, pure ZB and WZ regimes for binary compound nanowires can be found by varying easily accessible growth parameters such as V/III ratio, but specific methods have to be developed to make the heterostructures sharp between the pure crystal structures.[59] Therefore, switching between the pure crystal structures often results in a transition through a mixed, stacking fault rich, regime, where the stacking sequence neither produces long range ZB nor WZ. When forming a pure crystal structure, every layer that nucleates and grows across the interface consists of the exact same material as the previous layers, meaning that the interface energy between nucleus and "substrate" (nanowire) is equal to 0. If the nucleus instead has a different stacking than expected, essentially creating a stacking fault in the structure, an additional energy term treating the interface between the nucleus and the nanowire needs to be considered.[65] As discussed earlier, however, this energy term should be very small during nanowire growth, and stacking faults can readily form.[66] The formation of twins in GaAs is discussed further in Chapter 6 and **Paper v**, but an example of stacking faults and twinning is shown in Figure 2.8 (a).

In a similar way, compositional heterostructures can be formed by changing the gas phase composition to replace one of the elements with another one from the same group.[64,67] An example would be to grow GaAs and then switch to GaSb, as shown in Figure 2.8 (b) and (c). The GaSb nucleus would not only have an associated surface energy term to the substrate, but there would also be an added strain term to the expression of Gibbs free energy (shown in Equation 2.5), changing it to Equation 2.10.

$$\Delta G = \Delta G_V + \Delta G_S + \Delta G_\epsilon \tag{2.10}$$

The addition of strain on the lattice will further increase the barrier for nucleation, and

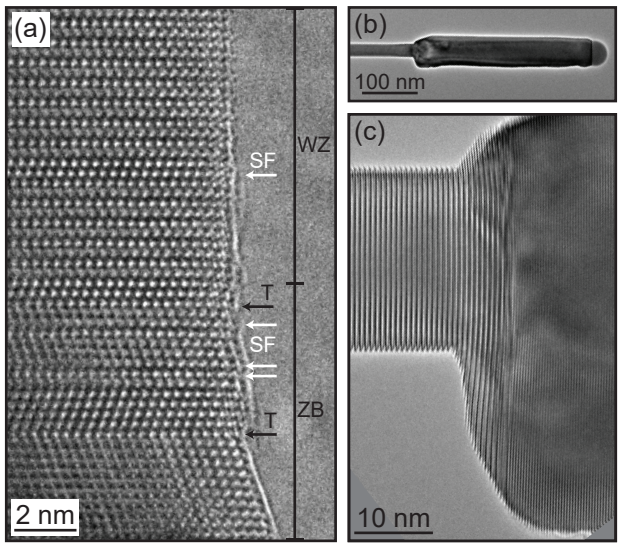

Figure 2.8: (a) A TEM micrograph showing a part of an InGaAs nanowire. The bottom half is predominantly ZB, while the top half is predominantly WZ. Some crystallographic twins (T) and stacking faults (SF) are marked by black and white arrows, respectively. As the structure becomes more defected the exact stacking sequence becomes more difficult to determine, but the twin present furthest down in (a) is clear. (b) A compositional heterostructure between GaAs (left) and GaSb (right). As can be seen, the radius expands significantly in the GaSb segment. (c) A magnified micrograph of the heterostructure shown in (b). The crystal structure changes as the material changes.

therefore also increase the required supersaturation for nucleation. For many combinations of binary III-V semiconductors, heterostructure formation works well in one direction, but worse in the other.[68] There are many factors that contribute to this, for example the solubility of the different elements in the nanoparticle and the liquid-solid surface energy between the Au-based alloy and the different compounds. In one heterostructure direction, the strain on the nucleus will be compressive, while in the other the strain will be tensile, owing to the difference in lattice parameter, which can also affect the nucleation. In the case of InAs and GaAs, growth of GaAs on InAs can easily be achieved, while the reverse direction often results in nanoparticle loss or a change in growth direction (kinking).[69,70,71]

Instead of forming an abrupt heterostructure between two binaries, the nanowire might force (or the growth conditions can be tailored to give) the growth of a ternary transition region.[72] For certain applications, specific ternary compositions are formed to match the lattice parameter between different segments or to give specific properties.[10,73] If the composition is gradually changed so that the change in composition is small, the lattice parameter across the transition region will also change gradually, which significantly lowers the strain term in Equation 2.10. However, for certain materials, e.g. InGaAs, there exists a miscibility gap for normal growth temperatures, which results in a phase separation of InAs and GaAs in bulk crystals.[74,75] The investigation of transition regions in InGaAs has been a large part of **Paper II**,**III** and **VI**, and will be further discussed in Chapter 5 and 6.

Chapter 3

The transmission electron microscope

Transmission electron microscopes have been a central part of many materials scientists' arsenals since they began being commercialized in the 1930's, and big improvements to methodology, instrumentation and post-processing of the data is made every year.[76,77] In this chapter, the basic operations of a transmission electron microscope, as well as the layout of the environmental transmission electron microscope used throughout the work presented in this thesis, will be introduced. The different imaging modes that are common in modern TEM, and the origin of contrast within the transmission electron microscope, will be discussed. Differences between the design of an environmental transmission electron microscope, as compared to a traditional transmission electron microscope, will be highlighted, and a detailed description of the gas handling system and its connection to the environmental transmission electron microscope will be presented. Unless otherwise specified, the TEM book by Williams and Carter has been used as the reference throughout this chapter.[78]

3.1 Basics of TEM

A transmission electron microscope, at its core, is quite similar to a traditional table-top light microscope. Basic light microscopes often operate by shining visible light from underneath a sample and then collecting the transmitted light into magnifying optical lenses, before allowing the light to reach the observer's eye. Thus, the image of the object of interest will appear much larger than what it actually is, while the light can also create contrasts between different areas of the object that allow more or less light to shine through (due to differences in mass and thickness). TEM works much in the same way: there is a

source that supplies electrons instead of photons, which are then allowed to travel to and interact with a sample. This creates some kind of contrast between areas that interact more or less with the electrons. The beam of electrons is then magnified using lenses and projected onto a camera or a fluorescent screen, so that the information can be viewed by eye. Some notable differences between a standard light microscope and a transmission electron microscope are that the latter is typically operated under vacuum conditions and the lenses are electro-magnetic instead of traditional optical lenses. Based on the discussion above, the transmission electron microscope can be split into four parts:

- The illumination system responsible for forming the initial beam of electrons.
- The image formation system responsible for the interaction of the beam with the sample.
- The projection system responsible for the magnification and selection of what information is being relayed.
- And finally the detection system, responsible for detecting the signals produced through TEM.

Figure 3.1 (a) shows a real image of the transmission electron microscope used in the works presented in this thesis, while Figure 3.1 (b) schematically shows the lenses that constitute the different systems described in the list above. All of the systems work in tandem to allow the study of a wide range of samples, and will be discussed later on in this chapter. At a glance, this might seem awfully complex, so why do we bother using electrons to image rather than simply light? In order to answer that, we need to discuss resolution, the smallest resolvable separation between objects, which is connected to the wavelength of the electrons or photons used for imaging.

The wavelength of an electron is related to its kinetic energy, and in the case of TEM, generated electrons are accelerated by using a high voltage, commonly between 80-300 kV, with some microscopes using as high voltages as a few MV. The high electric potential, V, results in a kinetic energy of the electrons as eV, where e is the charge of the electrons. The high energy of the electrons results in a small wavelength, λ based on Equation 3.1 (here disregarding relativistic effects).

$$\lambda = \frac{h}{\sqrt{2m_0 eV}} \tag{3.1}$$

In Equation 3.1, h is Planck's constant and m_0 is the rest mass of the electrons. As already mentioned, the wavelength is connected to the resolution when imaging. In a light microscope, the theoretical maximum resolution (without using any advanced super-resolution

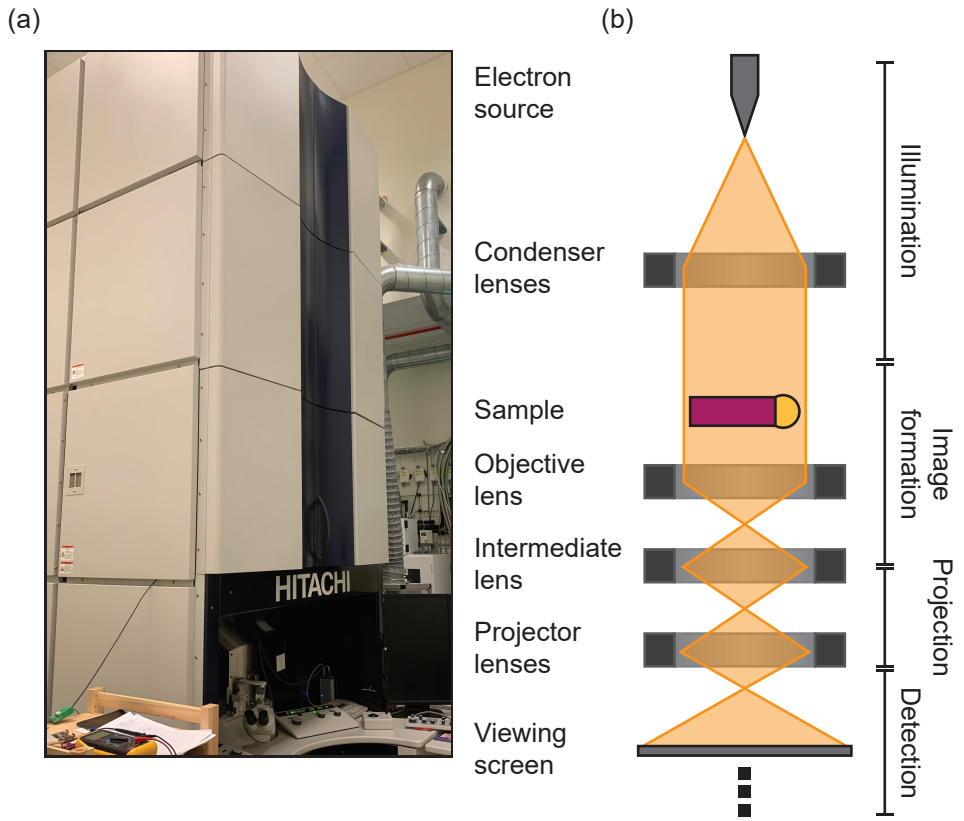

Figure 3.1: (a) An image of the environmental transmission electron microscope, Hitachi HF3300S, used for all the *in-situ* experiments presented in this thesis. The microscope itself is, of course, hidden behind a cover, but some of the controls and the viewing screen are visible at the bottom of the image. (b) A simplified schematic illustrating the lenses present throughout a typical transmission electron microscope column. Some important objects along the path are also shown (Electron source, Sample and Viewing screen). The four systems we split the microscope into when discussing it are also outlined.

methods such as STED[79] or STORM[80])* is given by the Rayleigh criterion presented in Equation 3.2.

$$\delta = \frac{0.61\lambda}{\mu \sin\beta} \tag{3.2}$$

In Equation 3.2, δ is the observable separation, and μ and β are the refractive number of the viewing medium and the magnifying lens semi angle of collection, respectively. If we assume that the denominator in Equation 3.2 is equal to 1, we see that the resolvable

*STimulated Emission Depletion (STED) microscopy. STochastic Optical Reconstruction Microscopy (STORM).

distance becomes a little more than $\lambda/2$, which puts us at a few hundred nm for visible light. The wavelength of an electron accelerated to 300 keV, on the other hand, is 0.00223 nm, much smaller than an atom!† With such a small wavelength, imaging of atoms should therefore be trivial. However, as it turns out, the electromagnetic lenses used in TEM play a large role in the final attainable resolution.

3.1.1 Lenses and apertures

In order to shape the beam of electrons that travel down the column of the microscope, electromagnetic lenses are used. As the electrons travel down, they move in a spiral around the optical axis, and the magnetic field generated by the lenses can be used to affect this movement, and to shape the electron beam to smaller or larger cross section. The way this is done is a bit different than regular optical lenses. Lenses that affect light can be of many types, where two main types are convex and concave lenses, that can be used to converge or diverge parallel beams of light, respectively. All electromagnetic lenses are convex, meaning that several lenses are typically used in series to shape the beam. This becomes important when considering that most modern transmission electron microscopes can operate in both a conventional TEM mode, where the beam is parallel and covers a large area of the sample, and in a scanning transmission electron microscopy (STEM) mode, where a very fine probe is formed and scanned across the sample. An example of how an electromagnetic lens shapes the beam can be seen in Figure 3.2.

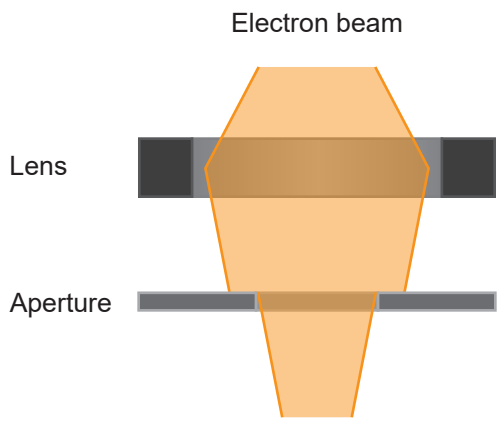

Figure 3.2: A schematic showing an electron beam traveling through an electromagnetic lens and its aperture. Both the lens and aperture are assumed to be circular in their geometry, and are as such drawn as cut in half (so that the cross-section is seen). The beam path is affected by the lens in the sense that the direction of the electrons is changed as they travel through. As the beam travels through the aperture, the outermost electrons are blocked off, and therefore do not continue down the column.

†This is if we disregard relativistic effects. If we add them, the wavelength would be even smaller!

Electromagnetic lenses are typically not too great at what they do. If a lens is not cylindrically symmetrical, for example, this deviation will be transferred to the beam of electrons in the form of astigmatism. This is corrected for by placing stigmators in the column, which are advanced, multipole, lenses, that are used to shape the beam to become more cylindrically symmetrical. Another problem that is common for electromagnetic lenses is the emergence of multiple kinds of aberrations, where electrons that arrive at the lens closer to, or further away, from the optical axis will be affected differently by the lens. A major kind is called spherical aberration, which causes electrons further away from the optical axis to be focused to a point earlier than electrons closer to the optical axis. Electrons of different energies will also be affected differently by the lenses, an effect called chromatic aberration. In this case, electrons of lower energy will be more strongly affected by the lens. However, when comparing two evils, spherical aberration is in most cases the more prevalent form of aberration, and therefore most effort has been put to dampen the spherical, rather than the chromatic, aberration. There exists also several higher order aberrations, and specific equipment called aberration correctors can be used to limit them.[81]

One way to further shape the beam and to limit the electrons most affected by spherical aberration is to use apertures in the column. Apertures are essentially holes in a plate of thick, non-electron transparent materials, which will limit the radius of the electron beam and therefore block a certain number of outer electrons, as shown in Figure 3.2. They can also be used in clever ways to select which electrons are used when imaging, which becomes important in many imaging modes available in TEM.[59,82]

Now that we know a little bit about lenses and their drawbacks, it is time to briefly discuss the four different systems and their associated lenses, as presented earlier, starting with the illumination system.

3.1.2 Electron sources, the illumination system and the imaging modes

All electron microscopes need a way to produce the electrons used for imaging. The electron source of a transmission electron microscope is commonly referred to as the electron gun, and there are several different types of guns available depending on the intended usage of the microscope. The two main classes of electron guns are thermionic, where the electrons are emitted through heat, or field emission, where the electrons are mainly emitted through the pull of an electric field (but can also be heated). When a field emission gun (FEG) is unheated it is typically referred to as a cold FEG, and its main advantages are that the electrons emitted are more coherent (less energy spread) and a higher current density can be achieved than in the other cases. However, a limitation is that it typically requires a better vacuum, since it can act as a site for deposition of gas phase molecules, ultimately degrading the electron emission. By running a high current through the gun, termed flashing the gun, the contaminants can be removed, which gives a way of ensuring adequate emission. We

will discuss the cold FEG more when we discuss the setup that was used throughout this thesis.

When the electrons have been generated and accelerated, the first set of lenses they encounter is the condenser lens system. This lens system is responsible for forming the image of the electron source and is used to affect the size of the area being illuminated further down at the sample, when operating the microscope in conventional TEM mode. Two or more lenses often work in tandem to achieve a close to parallel illumination of the sample. In STEM mode, the beam is instead condensed to a fine point and scanned across the sample, which allows the collection of information not attainable in conventional mode. The scanning is achieved using scan coils in the microscope column, which allows lateral displacement of the beam. However, the actual formation of the fine probe is handled by the objective lens, as will be discussed when the image formation system is explained in the next section.

3.1.3 Sample interaction and the image formation system

One typical requirement for TEM samples is that they are electron transparent, which means that on average, the electrons that travel through the sample partake in less than one scattering event. In other words, the mean free path of the electrons in the sample is longer than the sample thickness. This means that the majority of the electrons are actually transmitted through the sample without interacting. However, many of them still interact with the sample in various ways, resulting in a large range of signals that can be detected. Some of the important signals are summarized in Figure 3.3, which will be referred to later when we discuss contrast in TEM. One common type of interaction is termed elastic scattering, where the electrons interact with the nuclei of the atoms in the sample, change trajectory, but do not lose energy. When electrons on the other hand interact inelastically, with the electron cloud, they lose energy in some way, which means that the coherency of the electrons is lost.

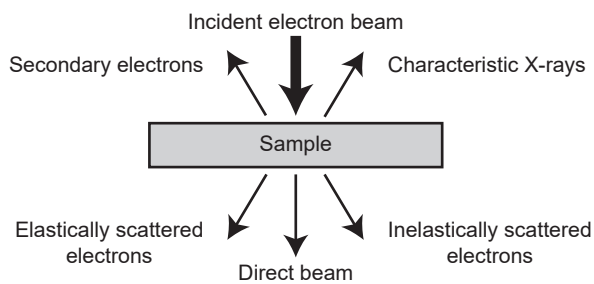

Figure 3.3: A schematic detailing some of the signals generated when the electron beam interacts with a sample.

In the sample area sits the objective lens, with its main responsibility to use the electrons transmitted through the sample to form the first image of the sample, to be conveyed to the projection system. It also has other responsibilities depending on the imaging mode used. In conventional TEM, the electrons (ideally) arrive at the sample as a parallel beam, illuminating a portion of it. The resulting image of the part of the sample will be conveyed from the objective lens to the projection lens system via an intermediate lens. However, the strength of the objective lens will in this case determine where along the optical axis the image of the sample forms, and will therefore decide whether the sample is in focus or not as it is being conveyed by the intermediate lens. In the back focal plane of the objective lens there also forms a diffraction pattern of the sample (diffraction will be discussed later). Depending on the strength of the intermediate lens, one can chose to convey instead the diffraction pattern to the projection lens system. This is accessed by operating the microscope in diffraction mode. Both conventional TEM and diffraction are illustrated in Figure 3.4.

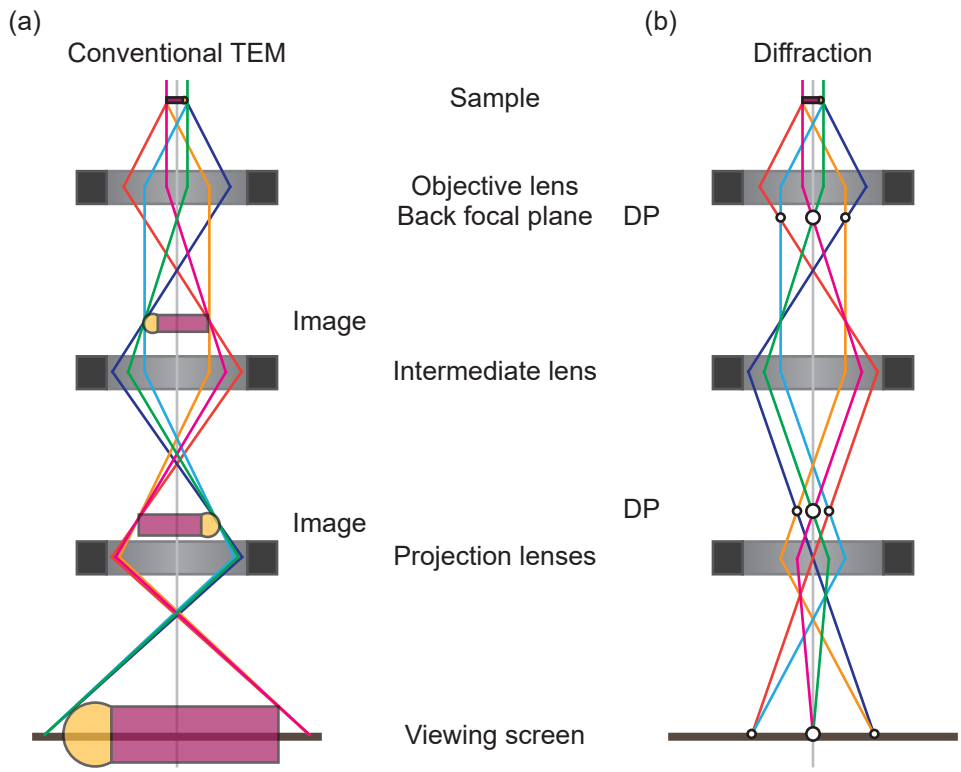

Figure 3.4: Schematics illustrating the beam path while operating the transmission electron microscope in parallel beam mode for conventional TEM imaging (a) and diffraction (b). The main difference between the two configurations is the strength of the intermediate lens, which decides what information will be conveyed to the projection lens system.

As discussed earlier, the transmission electron microscope can also be operated in STEM

mode where the beam is condensed to a small probe before the sample. To achieve this, the objective lens is in most modern systems split into an upper pole piece above the sample and a lower pole piece below the sample, where the upper pole piece is used to form the fine probe. After the beam has been transmitted through the sample, the lower pole piece works in tandem with the projector lenses in order to make sure that the electrons end up on the correct detector, which will be discussed more in the next section.

3.1.4 Projection, detection and contrast

In conventional TEM, the projection lens system is responsible for the magnification of the information the intermediate lens is conveying, whether it is an image or a diffraction pattern. Eventually, the image or diffraction pattern ends up on a fluorescent screen or an electron sensitive camera (common technologies for the camera construction are charge coupled device (CCD) or complementary metal–oxide–semiconductor (CMOS)), where the contrast produced as the parallel beam interacted with the sample is displayed. When operating the microscope in STEM mode, the projection lens system determines which electrons end up being detected, depending on the scattering angle they exit the sample with. This is usually achieved by having two detectors: a bright field (BF) detector and an annular dark field (ADF) detector. To understand why the microscope is equipped with all these detectors, we need to spend some time to discuss the contrasts generated when the electron beam interacts with the sample.

The first contrast we will discuss is amplitude contrast. This is, simply put, contrast that arises from the difference in amounts of electrons that are transmitted through the different parts of the sample without interacting strongly. This can be further split into mass-thickness contrast and diffraction contrast. Mass-thickness contrast, as the name suggests, arises when there are differences between the mass and thickness of different regions of the sample. The reason is that thicker parts of the sample have a higher probability of absorbing or scattering electrons than thinner parts. Similarly, a region of high density material will scatter electrons more strongly than a low density region. These effects result in fewer electrons passing through higher density or thicker regions of the sample. Since the cameras used for conventional TEM operates by detecting the electrons that arrive at its pixels, the thicker regions of the sample will appear darker when the resulting image is displayed on the computer screen.

The other type of amplitude contrast introduced earlier, diffraction contrast, is also important, especially when analyzing crystalline samples. Diffraction as a phenomenon involves coherent, elastic scattering of electrons, depending on the periodicities present in the sample. Since crystals exhibit long range order, diffraction can be utilized to determine, for example, the crystal structure, the orientation of the crystal and whether or not there exists any defects in the material. A diffraction pattern formed through the scattering will

exhibit discrete spots in a pattern that relates to the crystal structure of the material, and is essentially a fourier transform of the information contained in the illuminated region. It always contains a central spot created by the undiffracted primary beam, and additional spots at specific distances from it.

As was already mentioned, the objective lens forms a diffraction pattern of the sample in its back focal plane. This can be used in order to enhance diffraction contrast in an image, by inserting an aperture into the back focal plane. By centering the aperture on the central spot, essentially only allowing the undiffracted beam to pass through, one can create an image where all regions that diffract the beam appear dark. This type of imaging is termed bright field (BF) imaging, since the "background" (where there is no sample to disrupt the beam) will appear bright, while all other areas appear dark. Similarly, when centering the aperture on one of the diffracted spots, only the information in the sample that generated that specific diffraction will be relayed to form an image. This is especially useful when the sample contains several different crystal structures or viewing directions, since only the crystals that diffract to the specific spot will appear bright in the final image. Since the primary beam is also blocked, the background will in this case appear dark, and the imaging mode is therefore called dark field (DF) imaging.

Both mass-thickness contrast and diffraction contrast are important for the image formation in STEM mode. As already mentioned, two different detectors are commonly utilized when operating the microscope in STEM mode, namely the BF and the ADF detectors. The BF detector is centered on the optical axis of the microscope, and is consequentially used to detect electrons that have either not scattered or only scattered weakly when interacting with the sample. Hence, the background in the final image will appear bright, giving the detector its name. The ADF detector is annular and therefore has a hole in the central beam path. The point of the ADF detector is to register electrons that have scattered upon interacting with the sample. As mentioned earlier, the projection system and objective lens can be used to chose which electrons, depending on their scattering angle, will hit the ADF detector, resulting in several modes of operation. Possibly most popular is high angle annular dark field (HAADF) STEM, where only electrons that have scattered with a comparatively high angle are detected. At such high angles, the contrast is only created by mass-thickness differences of the sample, which allows for easier interpretation. An example detailing how the differently scattered electron beams end up on the different detectors in STEM mode is shown in Figure 3.5.

For the work presented in this thesis, perhaps the most important type of contrast is the so called phase contrast. This type of contrast has the most effect when performing high-resolution transmission electron microscopy (HRTEM), which enables imaging with atomic resolution. In broad terms, phase contrast appears from interference between the direct and diffracted waves, where the electron waves experience a phase shift as they pass through the sample, depending on its potential. The effect on the phase will depend on

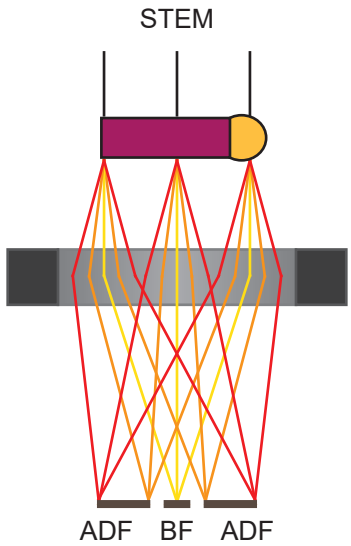

Figure 3.5: Schematic diagrams illustrating the beam path while operating the transmission electron microscope in STEM mode, with a condensed beam hitting the sample at three different spots illustrated by the lines at the top of the figure. Electrons scattered at larger angles (more red) will end up further out on the detector, while electrons that are less scattered (more yellow) will end up closer to the center of the optical axis. Here, some electrons end up on the BF detector, while some end up on the ADF detector. By tweaking the lens strength, one can ensure that more or less strongly scattered electrons end up on the ADF detector.

how close the electrons pass the atomic columns in the sample, where electrons passing close to the atoms will be more strongly affected. Phase cannot be directly detected and will therefore be translated to amplitude contrast, as described by a contrast transfer function. This contrast transfer function includes a number of properties of the microscope, including aberrations and the strength of the objective lens. This means that, by limiting the aberrations, the contrast transfer can be improved. Microscopes are often calibrated so that the atomic columns appear dark while the spaces between them appear bright at optimal conditions.

3.1.5 Compositional analysis

In terms of compositional analysis, there are two main methods used in TEM: electron energy loss spectroscopy (EELS), where the energy of the transmitted electrons is analyzed after the interaction with the sample, and x-ray energy dispersive spectroscopy (XEDS), where the x-rays generated by the interaction between electrons and specimen are analyzed. Here we will only discuss XEDS, since that was the method available in the microscope used throughout this thesis.

As mentioned earlier, the beam electrons sometimes interact inelastically with the sample

being investigated. Inelastic interactions involve a transfer of energy, and occasionally this energy causes inner core electrons bound to the atoms in the sample to be ejected as secondary electrons. This leaves the atom in an excited state, something that can be relieved by allowing an outer shell electron to relax and occupy the vacant spot in the inner shell. During the relaxation, the outer shell electron has to release energy equal to the difference between the two energy levels it is moving between. This energy can leave the atom as a photon, which therefore is characteristic to the difference between the energy levels present in the atom. The process is illustrated in Figure 3.6.

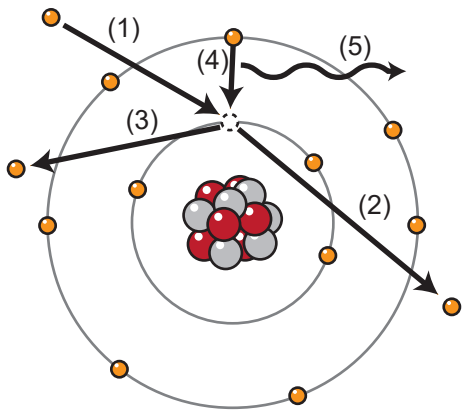

Figure 3.6: Schematic detailing the generation of x-rays from electron irradiation. An incident electron (1) interacts inelastically with a core electron of an atom in the specimen, changing trajectory (2) and emitting the core electron as a secondary electron (3). The atom enters an excited state, where relaxation can be achieved by allowing an electron from an outer shell to reduce its energy and occupy the now empty core energy level (4). The excess energy is emitted as a characteristic x-ray (5).

The basis of XEDS is to detect these x-rays that are generated when the electron beam interacts with the sample. In conventional TEM, the spectrum will be generated from the entire area being illuminated, which is useful for homogeneous phases. After detection, the x-rays will be presented in the form of a spectrum, detailing all the elements present in the illuminated part of the sample. The acquisition of this type of spectrum is typically rather quick, since many x-rays are generated by the parallel beam and all the detected x-rays are used in the construction of a single spectrum. Similarly, in STEM mode, a spectrum can be generated from a singular point in the sample. This will also result in a singular x-ray spectrum with equally fast acquisition. However, operating in STEM mode provides more flexibility, as there is also the possibility of generating compositional maps by raster scanning the beam and generating individual spectra from each scan point. Since the beam is scanned, the signal generated from each point will be much smaller than for a stationary beam, and the creation of a compositional map is therefore rather time consuming.

The spectral information can also be used for quantification, and the most common technique is by utilizing Cliff-Lorimer ratios, as in Equation 3.3.

$$\frac{C_A}{C_B} = k_{AB}\frac{I_A}{I_B} \tag{3.3}$$

In Equation 3.3, C_A (C_B) and I_A (I_B) are the concentration and spectral intensity of species A (B), while k_{AB} is the Cliff-Lorimer factor. This factor depends on the atomic number of the elements being considered, and is usually theoretically determined. The drawback with the Cliff-Lorimer determination of concentrations is that it assumes very thin samples, and quantification gets progressively worse for thicker samples. This is because the Cliff-Lorimer factor does not account for absorption and fluorescence within the specimen, which occurs to a greater extent in thicker samples.

3.1.6 *In-situ* TEM

In classical electron microscopy, one of the core aspects is that the samples being investigated are unchanging, and should ideally not be affected much by the electron beam. Of course, with enough high energy electrons, one can easily destroy a sample, or otherwise affect it. A couple of common examples are "drilling" holes in the crystal when producing diffraction patterns with a condensed beam or depositing layers of carbon-based material while imaging if the vacuum is not good enough. Nowadays, however, *in-situ* TEM is becoming increasingly popular, where the sample is subjected to some kind of intentional external input while being investigated. The possible inputs involve heating,[83] biasing,[84,85] liquid conditions,[86,87] gaseous conditions,[88,89] exposure to photons[90] and mechanical inputs,[91] among others. This has allowed researchers to visually investigate many different processes occurring in micro- to nanoscale materials, such as oxidation and degradation,[92,93] nucleation and crystallization,[94,95] domain migration,[96] light-matter interactions,[97] catalytic properties,[98,99] phase transformations[100] and liquid-solid interfaces.[83] Especially interesting for the work conducted in this thesis are of course the various *in-situ* investigations of nanowire growth, where aspects such as morphology,[101,102] composition[49] and layer growth dynamics[58,103,104] have been explored. The specific *in-situ* setup that was used for the work presented in this thesis is discussed in the following section.

3.2 The environmental transmission electron microscope

Before we begin discussing the different parts of the environmental transmission electron microscope, it should be noted that the specific microscope that was used throughout the work presented in this thesis is designed to be useful for studying chemical reactions, with an emphasis on nanowire growth. As such, an open cell configuration for gas supply was chosen. With an open cell, the gas is flowed *directly into the column of the microscope*, which

will have some implications as we will see shortly. Closed cell setups are more readily available, and there are many solutions and brands (e.g. DENSsolutions, Protochips and Hummingbird Scientific). The common denominator is that the chemical reaction is kept in a closed environment attached to the sample holder, so no gas (or liquid, in the case of liquid cells) can escape into the microscope column. This also means that the actual encasing needs to be electron transparent, but it typically has a thickness of tens of nanometers, which will affect the electron beam as it travels through. In this sense the open cell configuration is convenient, since interpretation of the information seen in the resulting images is more direct when the electron beam has only interacted with the sample.

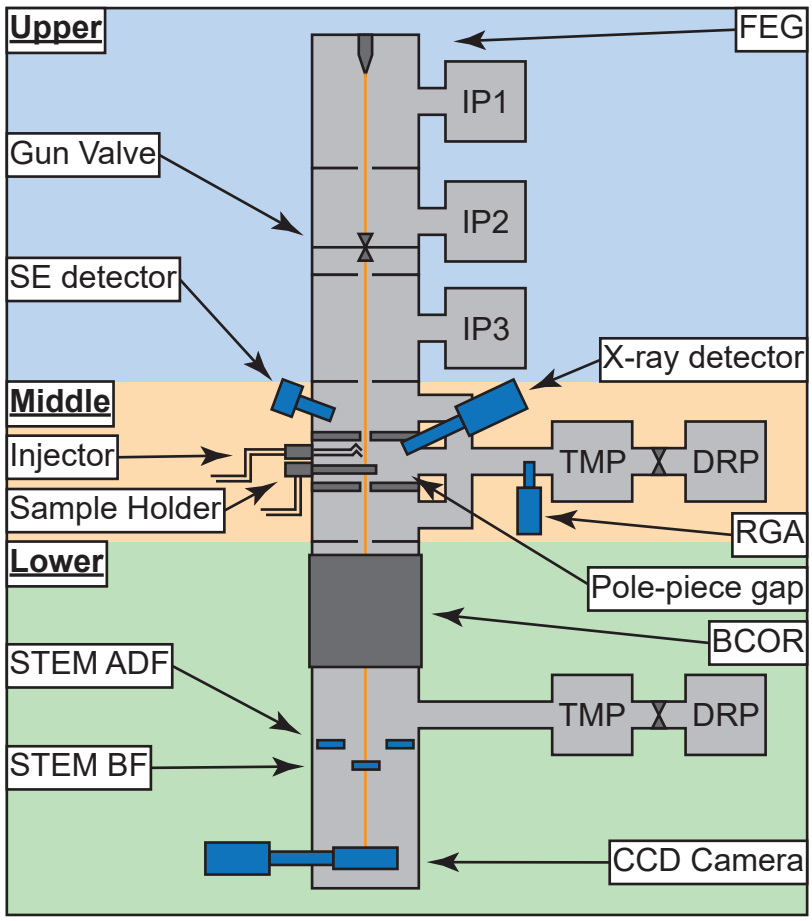

Figure 3.7: A schematic of the environmental transmission electron microscope at Lund University. The schematic is splitting the microscope into three parts: Upper, middle and lower.

Figure 3.7 shows a schematic of the environmental transmission electron microscope that

has been used throughout the work presented in this thesis. For convenience, the schematic is split into three parts that will be discussed (somewhat) separately. The schematic is mostly focused on the available equipment, so most lenses and technical details about the lens systems have been omitted. More technical details about the microscope have been summarized by Hetherington et. al.[105]

3.2.1 Upper environmental transmission electron microscope

In the upper part of the environmental transmission electron microscope, the first thing we find is the electron gun. In this case, the microscope is equipped with a cold FEG, as discussed previously. Now, a FEG is quite sensitive to the vacuum of the microscope,‡ and an important aspect of the open cell configuration is that the microscope has a significantly higher internal pressure during experiments than any normal TEM (up to several Pa).[105] In order for the gun to survive this, an extra ion pump (IP) has been installed on the column, so as to make sure that the gun operates under vacuum while gases are supplied to the column. Figure 3.7 shows three IPs on the upper part of the column, and they all work to remove gases that make it up towards the gun. A common gas used in experiments is H_2, which is small enough to diffuse up to the gun in a substantial amount. Normally, a FEG should not need to be flashed (cleaned with a high current) more than after a restart of the microscope. However, during experiments, the gun is flashed (at a lower current) every ten minutes or so, due to the H_2 degrading its performance. One way to mitigate this effect is to close the gun valve, which of course means that no electrons reach the sample, so this is only done during waiting time.

3.2.2 Middle environmental transmission electron microscope

Continuing downwards in Figure 3.7 we arrive at the middle section, which evidently is quite crowded. This is where the sample is situated, mounted on one of the sample holders that will be discussed later. We can also find the injector, which is one way to supply gas into the microscope. Both of these important pieces of the system are situated in what is commonly referred to as the pole-piece gap of the objective lens, which is the gap between the upper and lower pole pieces that make up the full objective lens. Within the pole-piece gap, the tip of the XEDS detector is also situated, so that x-rays can be collected. The middle section also contains a secondary electron detector, which can detect secondary electrons generated from the sample, useful when surface morphology of samples are to be analysed in STEM mode. Here, there is also a turbomolecular pump (TMP) connected to a dry rotation pump (DRP), which are responsible for removing most of the gas that

‡According to Williams and Carter,[78] operation of a FEG requires an ultra high vacuum (UHV) on the order of 10^{-9} Pa, as compared to conventional thermionic LaB_6 filaments for which 10^{-6} Pa is sufficient.

is supplied to the microscope (they are much more powerful than the IPs). Close to the sample there is a pressure gauge measuring the pressure in the chamber, which is calibrated so that the pressure at the sample can be calculated (not shown in Figure 3.7). A similar pressure gauge is situated further towards the TMP. At this position there is also a residual gas analyzer (RGA), which can measure the relative amount of gases present in the chamber through ionization. This is mainly used to monitor if the gas is supplied properly, and if the gas contains any contaminants.

3.2.3 Lower environmental transmission electron microscope

The first equipment we see in the lower part of the microscope is the image aberration corrector, BCOR. The BCOR system is capable of measuring the aberrations in the lens system, by tilting the beam and measuring the diffraction pattern of an amorphous film, and analysing the contrast transfer. By using a series of correction lenses it can correct for aberrations present in the system, so that spatial resolution can be improved. Further down there is another connection to the TMP and DRP before we reach the main imaging detectors. The STEM ADF and BF detectors are inserted during STEM operation, depending on which signal is desired, and the CMOS camera (Gatan OneView IS) is used to record images and movies in conventional TEM mode.

3.2.4 A discussion on sample holders and the injector

There are several different holders available for the environmental transmission electron microscope depending on the type of experiment to be conducted. The two holders that have been mainly used in the work presented here are the "double tilt" and "double gas" holders, illustrated in Figure 3.8. The two key concepts in their names is "tilt" and "gas", where specimen tilt will be discussed firstly.

Tilting of the sample is often necessary when analyzing crystalline samples, as it allows the alignment of the atomic columns to the optical axis. *In-situ* tilting of nanowires is used to view various aspects of their growth and will be discussed further in Chapter 4. The simplest method of tilting the sample is to rotate the entire sample holder about its axis. This is often termed α tilt, and both the "double tilt" and "double gas" holders allow an α tilt of $\pm$ 10 °. However, tilting about the other axis, termed β tilt, is more complicated and requires specific modifications to the holder tip. The "double tilt" holder has the capability of $\pm$ 9 ° of β tilt, while the "double gas" holder lacks this functionality. This is due to the spatial limitations within the holder tip caused by the specific solution for gas delivery implemented in the "double gas" holder.

There are two ways of supplying gas into the microscope, where the first option utilizes a

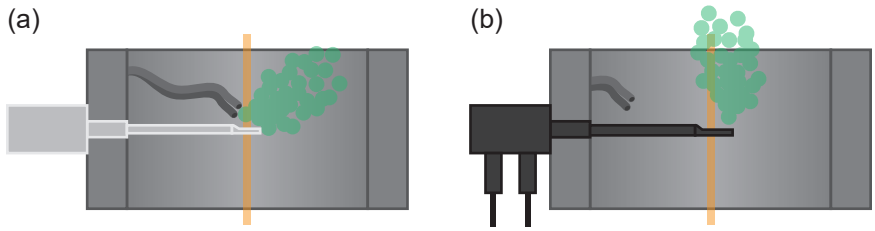

Figure 3.8: Schematic diagrams of the two holders, "double tilt" (a) and "double gas" (b), mostly used for the work presented in this thesis. For work using the "double tilt" holder, the precursor gas is supplied through the injector, while when using the "double gas" holder, the gas is supplied through the holder.

side port injector, which has two gas lines protruding into the column, separate from the holder. This is the construction used when operating the microscope with the "double tilt" holder inserted. The alternative is to supply the gas through the holder. The advantage of supplying the gas through the holder is that the gas will enter the growth chamber very close to the chip, independently of the sample holder tilt. This ensures that the delivery of gas is easier to predict in terms of its arrival within the microscope. However, transferring gas through a holder can potentially result in a lot of vibrations if the typical stainless steel tubing is used, which is detrimental to any HRTEM work. Therefore, the solution is to use special quartz and polymer (PEEK-SiL) tubes that connect to the gas handling system. These capillaries are more flexible and smaller, and transfer less vibrations, than stainless steel. However, this brings the problem of gas exchange rate. Right before the tubing that delivers gas into the microscope there is a "dead volume", where there can be a build-up of pressure. Since the capillaries are smaller than stainless steel tubing, the pressure in this volume typically reaches higher values when using the "double gas" holder. This means that when switching gas compositions, there will be a delay in the exchange of gas composition in the "dead volume", and subsequently in the microscope.

Supplying gas through the injector on the other hand means that when the sample is tilted there will be a change in the delivery of gas to the sample area. The effect of this has to be calculated based on the angle and the pressure inside the chamber.[106] However, the "double tilt" holder overall provides more flexibility and ease of use than the "double gas" holder, as it is less bulky and therefore affects the magnetic fields within the microscope to a lesser extent.

3.3 The gas handling system

One of the essential parts of the environmental transmission electron microscope is its gas handling system (GHS), capable of supplying a range of different gases to the microscope, through either the side port injector or the "double gas" holder, as discussed previously. In

essence, the gas handling system is very similar to how a typical MOCVD system operates, with the same types of containers for precursors and similar setup for flows. A big difference to more conventional systems, however, is how manual its operation is. With that in mind, we will here go through the system in detail.

3.3.1 What parts do we have?

The GHS at the Lund University environmental transmission electron microscope can supply several types of gases, including metal-organic and hydride precursors, as well as some usual process gases. This is very similar to what is available for a conventional MOCVD system. The metal-organic sources include tri methyl aluminum (TMAl), tri methyl gallium (TMGa), tri methyl indium (TMIn) and tri methyl antimony (TMSb). These are all precursors that contain methyl side-groups, and that are supplied using H_2 as a carrier gas, since they are stored as liquids or solids in bubblers (as discussed in Chapter 2). For hydrides, there is arsine, AsH_3 and phosphine, PH_3, which are both gaseous, do not need carrier gas to be delivered and are kept in gas cylinders. The process gases include H_2 as already mentioned, N_2 and O_2, which are also stored in gas cylinders. N_2 is often used as a relatively inert gas for flushing the system during internal cleaning, while O_2 is available for oxidation experiments. Importantly, the gas handling system is split into one group III line and one group V line, meaning that TMAl, TMGa and TMIn are available in one line and AsH_3, PH_3 and TMSb are available in the other, with the process gases available for both lines. However, it is possible for the gases to (accidentally) be mixed between the lines, and caution has to be taken at all times when operating the gas handling system to prevent this. We will get back to this aspect when we discuss mixing of gases further on in this chapter. A simplified schematic of the gas handling system, omitting N_2 and O_2 is shown in Figure 3.9.

From the sources, the initial flow is set by MFCs, just like in the conventional MOCVD discussed in Chapter 2. These operate at flows in the unit of standard cubic centimeters per minute (SCCM), and will control the flow of pure gas from gas cylinders or the flow of H_2 through the bubblers in the case of the metal-organic sources. MFCs are also used to determine the final flows of the group III and V lines into the microscope further downstream.

On both of the gas lines there are pressure controllers (PCs). Instead of trying to supply a fixed flow of material, as is the case for the MFCs, the PCs will only let material pass after a certain pressure is reached on the upstream side of the controller. For a pure gas, such as the hydride sources, this has no effect on the gas supplied through the PC, and any pressure can essentially be set. For the metal-organic sources on the other hand, which are dependent on the H_2 carrier gas and the vapor pressure of the precursor, the pressure set by the PC will influence the upstream gaseous composition.

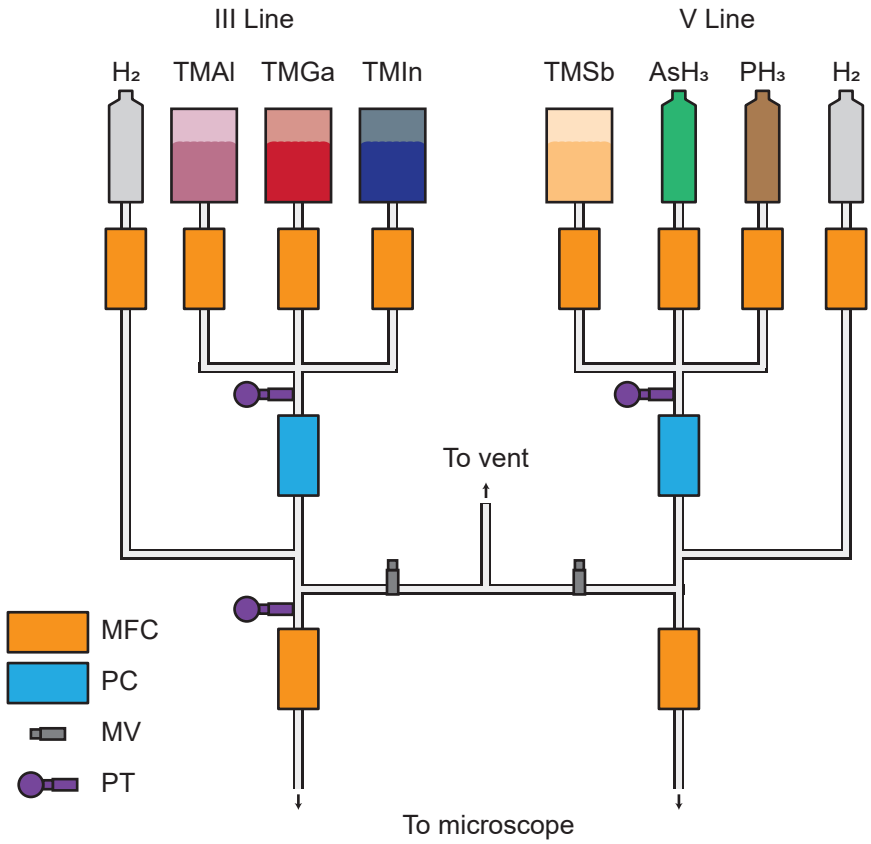

Figure 3.9: A schematic of a simplified view of the GHS used in connection to the environmental transmission electron microscope. Most importantly, the split between the group III and group V line, and the point where they meet, is illustrated. The H_2 lines that enter each bubbler separately have been omitted for clarity.

Other than the different controllers mentioned above, the system also contains a large number of pressure transducers (PTs). These are used to monitor the pressure in different parts of the gas handling system, so that, for example, stability and potential back flows can be monitored. To ensure that gas is only present in the areas where we wish it to be, there are a number of "open/close" valves throughout the system (not drawn in Figure 3.9), as well as a few manual valves (MV). The MVs are used during the experiment and gas-flow setup to prevent gas pressure build-up, by sending material to a separate vent-line.

As a side note it can be worth to mention that our gas handling system is overdimensioned for its intended usage, with MFCs capable of supplying hundreds of SCCM when we realistically stay in the $0.1 - 20$ SCCM range in most cases. This is because the system was designed with a conventional MOCVD system in mind, where operation is carried out with a high background pressure of H_2, which therefore requires a higher flow of the

precursors to achieve sufficient partial pressures. Similarly, the needle valves that allow gas to be removed through the vent line are extremely delicate and need to be tweaked to be barely open if you want to contain any gas at all within the system!

3.3.2 How do we know what the GHS supplies?

The bubblers are usually kept at standard temperatures, which will determine the relative concentration received in line based on their vapor pressure at this temperature and the set pressure in the line. The pressure is set by the PCs and when the pressure in the line is reached, the amount of material pushed through the PC is determined by the input flow. From a separate line, H_2 dilution is supplied to further dilute the precursors (usually only for metal-organics). After this, a flow into the microscope is set, while the rest of the gas is bypassed out to vent, to prevent a pressure buildup in the line.

Within the microscope there are also separate PTs that measure the resulting pressure based on the flow supplied. An experimentally determined correction factor is used to calculate the pressure at the actual sample, since, due to the geometry of the chamber, the sample pressure will be different than what the pressure transducers measure. When using the "double tilt" holder and the side port injector, there is also an additional correction factor for specimen tilt, since the tilt affects the distance from the injector tube to the sample. All of this is encompassed in a nifty excel sheet we use to determine the partial pressures of the precursors within the column, which can of course be translated to a commonly used V/III ratio.

As already mentioned, further towards the exhaust of the microscope sits an RGA which can measure the composition of the gas that is leaving the microscope via the pump system. The RGA works by ionizing the gaseous species and determining their mass, resulting in a representation of pressure as a function of mass over a defined range. This enables us to see when precursors have successfully been injected into the microscope column, and roughly follow when they have reached stable levels. The RGA also typically detects intermediates in the gas composition (intermediate compounds from the pyrolysis of the precursors, such as di methyl molecules (e.g. di methyl gallium, DMGa) and mono methyl molecules (e.g. mono methyl gallium, MMGa), for instance) and isotopes, giving us a more complete understanding of our gas composition. Importantly, the RGA is also used to check for leaks in the gas line connections, by supplying and measuring He levels from an external gas cylinder.

3.3.3 Advanced mixing of gases part I: two group III elements

As can be seen in the schematic of the GHS, Figure 3.9, there are two lines leading into the microscope, one for group III and one for group V elements. This means that when more than one element from either group is desired, the precursors will have to mix at a point far upstream the gas lines, making control of the ratio more difficult than when the two lines only contain one type of precursor each. Most importantly, one has to ensure that there is no backflow of material into any of the precursor sources, contaminating them with the other precursor. As an example we will here focus on the group III line, and the mixing of TMIn and TMGa.

The first step when mixing these two group III element precursors is to ensure that the pressure in both bubblers is close to the set pressure established in the line by the PC. Over time, the pressure in the line upstream from the MFC for each bubbler will reduce when the bubblers are not in use, but by setting a pressure after the bubbler and supplying an adequate flow through the MFC, the pressure in the line can be increased. To ensure that there is no backflow of precursor material, this procedure is done individually for both the precursors. The full process is shown schematically in Figure 3.10.

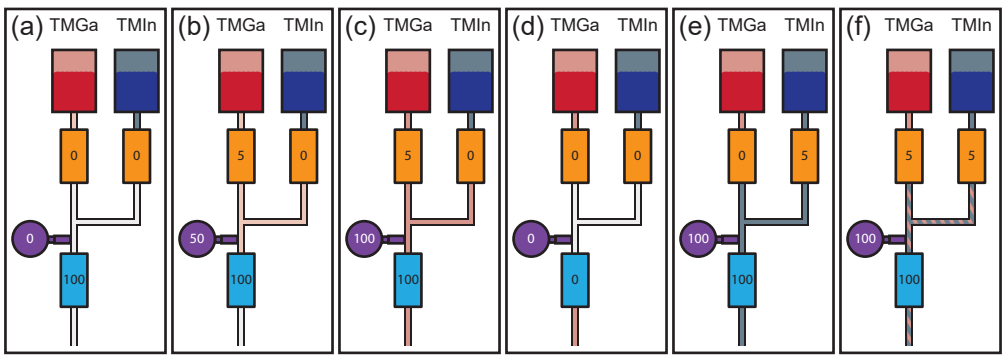

Figure 3.10: A schematic detailing the process when mixing TMGa and TMIn. (a) No flow occurs through either bubbler and the set pressure in the line is set to 100 on the PC (blue rectangle). This is the target pressure for the bubblers. (b) A flow is set on the MFC (orange rectangle) for the TMGa bubbler, and the resulting pressure in the line is measured by the PT (purple circle) to be 50. Therefore, the pressure needs to be increased before any material is allowed past the PC. (c) A pressure of 100 is reached, so material is passing the PC. (d) The flow is now set to 0 again, and the line is emptied by setting the PC to 0. (e) The PC is set to 100 and a flow is set on the MFC for the TMIn bubbler. The measured pressure is 100, so the PC allows material through. (f) Finally, a flow is set on the TMGa MFC and we get a mixture of TMGa and TMIn through the PC.

When both sources have been equilibrated, the amount of respective source supplied will be determined by the set flow and the vapor pressure of the source (as explained previously). An important aspect, however, is that most of the material supplied from the bubblers is H_2, meaning that there are three separate flows of H_2 in the group III line who all contribute to the dilution of the group III precursor and hydrogen mixture. Therefore,

careful balancing of the flows is needed in order to reach an adequate amount of group III material to match the amount of group V material supplied. An example might be in order: consider a situation where growth of pure GaAs growth has been achieved at a certain growth rate by supplying TMGa diluted with H_2 through the group III line and pure AsH_3 through the group V line. To initiate the growth of InGaAs, the approach might then be to simply supply a flow of TMIn through the group III line and hope for the best (assuming that proper equilibration of the bubbler pressures was done beforehand). If the flow of TMGa is then kept to the same flow as was used during the growth of GaAs, the dilution of the group III line from the H_2 supplied with the TMIn precursor will result in a much reduced amount of TMGa supplied to the microscope. Together with the fact that TMIn is generally kept at a temperature that results in a lower vapor pressure, the total amount of group III element supplied to the microscope during the InGaAs growth will be much less than during the GaAs growth and consequentially, the V/III ratio will increase. This means that if one wishes to keep the V/III ratio constant, the flow of TMGa will have to be increased. Then again, there is nothing saying that InGaAs will grow well at the same conditions as GaAs, so trying to exactly match the V/III ratio is likely futile. Nevertheless, this cross-dependence means that for any changes of the precursor flows, the effect it has on the other precursor has to be considered, which makes the tailoring of the growth parameters more complex when using more than one precursor from the same group.

3.3.4 Advanced mixing of gases part II: hydrogen dilution on both lines

As already stated, the metal-organic sources are often diluted in order to more carefully control the amount supplied into the microscope. This is all well when growing for example GaAs or indium phosphide, InP, where only the group III line contains a metal-organic source. The reason why this is preferable is that when diluting the line, there will in general be a large total amount of gas present, and not all of it should go into the microscope. That is why a portion of the gas is removed by sending it to a vent line, which ensures a stable pressure within the primary gas line and a stable flow into the microscope.

The problem with the vent line setup is that the vent line is shared between the group III and group V primary lines. Therefore, if a material such as GaSb is to be grown, where both precursors are metal-organic, both lines are diluted and both have to be open to the same vent line. This is one of the few places within the gas handling system where mixing of the two groups of precursors is possible, before being supplied into the microscope. This means that when the dilution is set up, great care has to be taken so that there is no back flow from one primary line to the other. This is typically achieved by ensuring that there is some overpressure on both lines before they are opened up to vent.§ The problem with

§In reality it is quite complicated and usually involves a bit of fast button pressing and occasional swearing.

this current setup is that the pressure within the group III line is readily available, while for the group V line it is not, due to the lack of a conveniently placed PT after the PC (see the schematic in Figure 3.9). This has of course not deterred us from growing GaSb within the microscope.

3.4 The Norcada heating chips

In terms of consumable equipment, the most important piece is the microelectromechanical system (MEMS) heating chips supplied by Norcada, that are used as substrates for the growth. The MEMS chips are Si-based, and have a few important components detailed in Figure 3.11. As can be seen in Figure 3.11 (a), there are four contact pads that electrically connect to the sample holders when the chip is inserted. These are primarily used to supply heat to the reaction area, which is situated at the center of the chips. The reaction area is heated resistively through a tungsten (W) coil that forms a spiral in a film of SiN_x. The SiN_x film is electron transparent, and forms the support for material deposited on the chips. The part of the SiN_x encircled by the W coil contains 19 wells of thinner SiN_x film, which consequently is more electron transparent than the surrounding, thicker, film. These 19 wells make the scene where material and reactions can be observed with atomic resolution. Within each well there is a hole in the film. Ideally, all imaging is being done on material that is sticking out into the holes, since in those regions there is no substrate interacting with the electron beam. When growing nanowires, the predeposited nanoparticles will be observable on the thin SiN_x film, and ideally the nanowires grow out into the holes to ensure the best imaging conditions. The growth of nanowires on these chips, and the methods we use to extract further information, will be the focus of the next chapter.

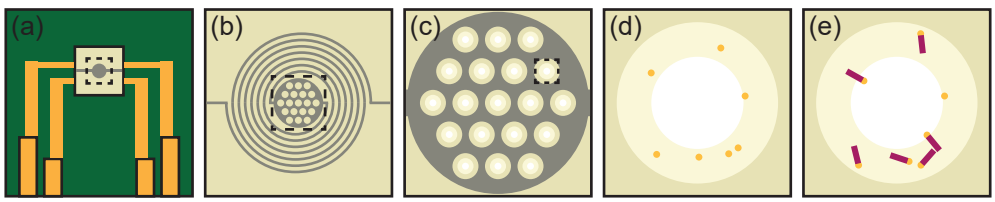

Figure 3.11: A series of schematic diagrams illustrating the MEMS chips, where the dashed squares indicate which region is highlighted in the consecutive panel. (a) The chip with contact pads and the central area visible. (b) The W coil embedded in SiN_x film, with 19 wells in the center. (c) The central area, showing that the wells consist of thicker SiN_x, thinner SiN_x and eventually a hole in the film. The W heating coil forms a matrix surrounding the wells. (d) A single well, showing the deposited Au nanoparticles on the thin SiN_x. (e) Same as panel (d) but after nanowire growth initiation. Some nanowires grow into the hole in the film, where ideal conditions for imaging are met.

Chapter 4

Nanowire growth within the environmental transmission electron microscope

Now that a solid background on nanowire growth and ETEM has been established, it is time to start combining the two. In this chapter, micrographs will be used in order to illustrate the appearance of nanowires grown within the microscope, and procedures used to facilitate the growth will be discussed. Microscopy techniques, specific information attained and ways of post-processing the data are introduced. This is meant to be an overview of some of the general techniques used in this work, and will facilitate the discussion that will be held in the final chapters of the thesis, where more concrete results are presented.

4.1 Nucleation and initial growth of nanowires

The formation of the initial nucleus from a nanoparticle is of course essential to any nanowire growth performed in a particle assisted growth mode. As such, nucleation is central to all the papers discussed within this thesis even if it has not been explicitly and thoroughly described in any of them.

To nucleate a nanowire, the nanoparticles have to be heated and a flow of precursors into the reaction chamber is required. The nanoparticles used throughout this thesis are 30 nm nominal diameter Au nanoparticles, created and deposited onto the MEMS chips as an aerosol before the chips are inserted into any ETEM holder.[107] At this size, the melting

point of Au nanoparticles is similar to the melting in bulk, so well above 1000 °C,[108] but by alloying (mainly) with group III elements the melting temperature is brought down to a few hundred degrees. All of the nanowire nucleations and growths conducted within the scope of this thesis were carried out at VLS conditions, where the nanoparticle is in a liquid state, at around 400 °C. The temperature is essentially chosen based on a few factors including the time it takes for the nanoparticles to nucleate, the growth rate of the produced nanowires and the amount of surface growth observed. Importantly, we try to keep the temperature to some value that works for the material system, and then not change it. This is because the temperature can have a large effect on many of the processes we observe, and of course affects the efficiency of the precursor cracking. Each precursor has its own precursor cracking efficiency curve that is not only difficult to find in literature, but also can depend on temperature, gas composition and substrate material.[36] This is why changing the flow of the respective precursors during experiments is often preferred, rather than adjusting the temperature. In general, different conditions are used for the nucleation of the material than for the actual growth, since the formation of the initial nucleus requires a higher supersaturation to overcome the initial barrier, while steady-state growth can be facilitated at lower flows.

Depending on the growth conditions it may take a few minutes, up to an hour, from the gas supply initiation to the nucleation of nanowires. Especially if good nucleation conditions have not yet been found for the material system, entire experiments are typically spent on achieving reliable and reproducible nucleation. Once nucleated, the initial crystal formation is often chaotic, as the nanoparticle needs to form and find preferred facets. This is a process of energy minimization, where the interface energy between the nanoparticle and the formed solid is different for different facets, but the supersaturation is so high during the nucleation event that many different facets may form. In many cases, the chaotic initialization of the nanowire growth can be controlled by finding good growth conditions. Figure 4.1 shows an image sequence detailing the nucleation process.

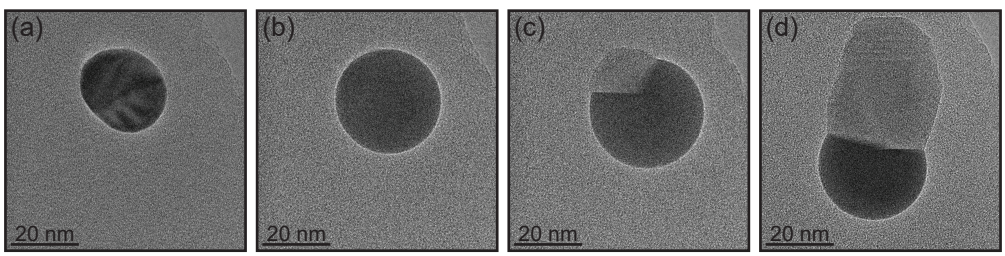

Figure 4.1: A nucleation event observed in the environmental transmission electron microscope. (a) A solid Au nanoparticle residing on a substrate. (b) The nanoparticle is now liquid due to alloying with growth species at elevated temperatures. (c) The nucleus has formed and the nanoparticle is wetting several facets. (d) The crystal is starting to look like a nanowire, as the nanoparticle has decided on a facet for the continued growth.

4.2 Growth of GaAs

Au-seeded GaAs is the most studied III-V material in the Lund University environmental transmission electron microscope so far.[37,49,54,58,103,109] One of the reasons for its popularity is its technological relevance,[110] while another is the relative ease with which it can be grown.* This has rendered GaAs a model system that is often compared to, when, for example, growth behavior and composition is investigated for other materials.

The growth of GaAs is relatively straight forward: heating up the Au nanoparticles on the MEMS chip to 420 °C, you supply both TMGa and AsH_3 simultaneously, and within a few minutes many of the nanowires will have nucleated and started growing. Importantly, the growth conditions should at this point be altered slightly, since we often observe an increased radial growth when the nucleation conditions are kept.† Hopefully a few of the nanowires grow out into the holes in the SiN_x film, so that there are several candidates that can be studied.

The reason why I discuss the growth of GaAs nanowire growth here is twofold: For one, the GaAs nanowires are in many cases used as stems for continued growth of the other materials discussed in the papers included in this thesis. A stem can help in getting properly aligned nanowires of other materials without having to optimize the growth parameters for nucleation from a pure nanoparticle on the amorphous substrate. Nucleating on top of the GaAs stem is in many cases easier, since the substrate in this case is crystalline. The other reason why GaAs is important to discuss is that it gives a baseline for what we strive to achieve in the other material systems, by optimizing growth parameters with regards to growth rate, aspect ratio and stability, among other things.

4.3 Growth of GaSb from GaAs stems

For the growth of GaSb nanowires, an established method of growing from GaAs stems was used.[111] This means that at the start of the experiment, nucleation and growth of GaAs is initiated as described earlier, before performing a switch of growth conditions to facilitate the GaSb growth. After several experiments of tailoring the growth conditions it was possible to improve the heterostructure formation from what is shown in Figure 4.2 (a) to what is presented in Figure 4.2 (b). The main difference between the two cases is that a higher partial pressure of both precursors resulted in a much better growth of GaSb.

*Besides, you have got to start somewhere, right?

†To put some numbers on this: An example would be nucleation at supplied partial pressures of $2.75e^{-4}$ Pa TMGa and $2.13e^{-1}$ Pa AsH_3, giving a V/III ratio of 777. Then for continued growth, both the precursors are increased, giving partial pressures of $5.47e^{-4}$ Pa TMGa and $6.38e^{-1}$ Pa AsH_3 and a V/III ratio of 1165.

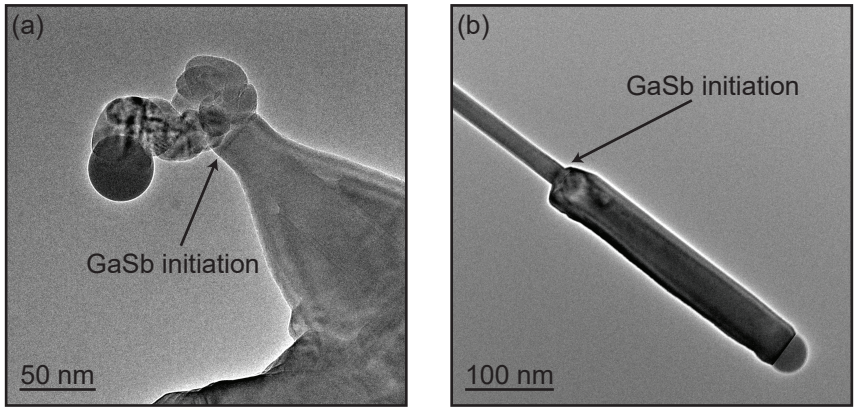

Figure 4.2: Two cases of GaSb growth from GaAs stems. (a) Early GaSb growth before growth parameter optimization. (b) GaSb growth after growth parameter optimization.

For the final growth conditions, the same temperature was used for both GaAs and GaSb growth (420 °C).

The reason why we resorted to growth of GaSb from a GaAs stem is that there is a large amount of literature showing that direct nucleation of GaSb from Au droplets is challenging, related to increased droplet wetting of the substrate caused by antimony, and growth from stems is the usual solution.[112,113] Naturally, we of course had to try to see if we could achieve the direct nucleation, which in the end became a large part of the master's thesis of Aidas Urbonavicius.[114] To summarize, the Au-based nanoparticles typically increased to a few hundred nanometers in diameter, through alloying with Ga (mainly), before nucleation was achieved, unless specific methods of temperature control were employed. In the end, nucleation of GaSb nanowires from GaAs is in many ways simpler, but it is good to have the possibility to nucleate and grow pure GaSb nanowires as well.

Since we are creating heterostructures between GaAs and GaSb, the nature of said heterointerface is important to investigate. Therefore much effort was put towards making the ternary transition region short. Initially, the growth rate was low, and achieving pure GaSb growth was challenging, since there was always some As lingering in the chamber or the group V line from the GHS. By increasing the flows of TMGa and TMSb we were not only able to increase the growth rate of the nanowires to a range where it is comparable to *ex-situ* growth,[113] but ternary regions of less than 100 nm were also consistently observed. The growth rate and growth dynamics of GaSb will be discussed further in Chapter 6.

4.4 Growth of InGaAs

In order to grow the InGaAs nanowires, Au nanoparticles were, as usual, deposited onto a MEMS chip and heated under gas flow. For many of the growths InGaAs was nucleated directly from Au, by supplying all three precursors (TMIn, TMGa and AsH_3) simultaneously to initiate the experiment. For some growths the InGaAs segments were instead grown after initial growth of a GaAs stem, as this allowed a more careful study of the initiation of In incorporation into the nanowires (which was most important in **Paper III**, as we will see in Chapter 5). In contrast to previously discussed growths, InGaAs nanowire segments were always nucleated and grown at a temperature of 380 °C. This temperature was found to be optimal in terms of In incorporation, based on a short study on In uptake for pure Au nanoparticles, where the trend alluded to a difficulty of incorporating In at the more frequently used 420 °C (see Figure 4.3).

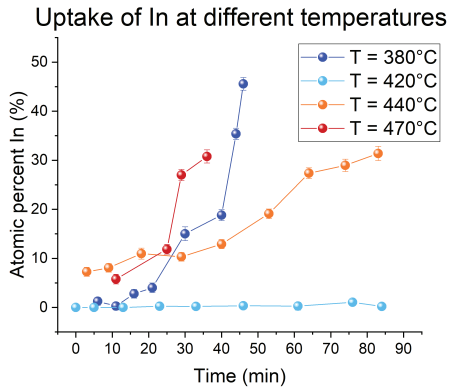

Figure 4.3: Study of the In incorporation in Au nanoparticles at different temperatures. As can be seen, the trend for T = 380°C shows the steepest increase of In concentration over time, while T = 420°C results in little to no incorporation. Gas supply was initiated at time = 0 min.

Even for growth schemes where no intentional GaAs stem was grown, the nucleation endeavors often resulted in the nucleation of close to pure GaAs nanowires. After nucleation, the growth conditions were in this case typically altered to increase the amount of indium in the vapor phase, so as to speed up the incorporation of indium into the nanoparticle and subsequently the nanowire.

4.5 Finding a good nanowire: tilting and viewing directions

After the nanowires have nucleated, they tend to grow in seemingly random directions on the chip. Now it becomes a waiting game in order to find a nanowire that grows out into

the openings of the SiN_x film, where we ideally want to image them. Not all nanoparticles are situated close to the holes in the film, so this process can take several hours, and is essentially luck based.

When nanowires growing into the vacuum are found, one must ensure that it fulfills the desired imaging conditions. Although the SiN_x film is relatively flat, the nanowires might grow with a slight tilt away from the horizontal plane. For this, the microscope and holders are equipped with tilting functionality, so that the sample can be tilted roughly $\pm$ 10° in one or two directions, as described in Chapter 3. The idea is that in many cases, one would wish to observe the nanowire growth perpendicular to the viewing direction, since this way we can find high symmetry orientations where the atomic columns within the nanowire are aligned along the optical axis, see Figure 4.4 (c). These high symmetry orientations are called zone-axes, and are useful for gaining atomic information about the growth. Sometimes, however, a high symmetry orientation can not be reached due to the limitations in the tilt amount. Then a birds eye view of the growth can be obtained instead, as shown in 4.4 (a), which might in some cases be beneficial. Importantly, the "double gas" holder is not equipped with β tilt, which means tilt is only possible in one direction. This puts some limitations on which nanowires can be used if a high symmetry direction is desired, and often one has to make do with an off-axis nanowire. Figure 4.4 (b) shows a nanowire that is being imaged edge-on, but the tilt around the nanowire axis was not sufficient to allow zone-axis conditions. Here, the in-plane information is lost, while the individual layers in the nanowire can still be resolved. This was often the case for the InGaAs experiments, which were carried out with the "double gas" holder, and hence, only α tilt functionality.

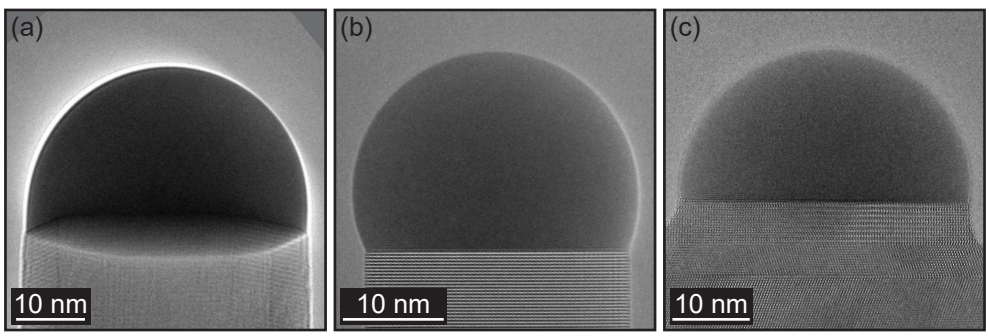

Figure 4.4: Micrographs detailing different viewing directions of nanowires. (a) An off-axis (birds-eye) view of a nanowire, where the interface between the nanowire and nanoparticle therefore is viewed at an angle. (b) A nanowire viewed edge-on, allowing the individual layers to be resolved. (c) A nanowire viewed edge-on allowing the atomic columns to be resolved. The difference between (b) and (c) is that (c) is tilted to a high symmetry orientation, where the atoms line up in the viewing direction, forming clear columns that can be imaged.

4.6 Measuring the composition during growth

One of the core strengths of performing nanowire growth *in-situ* is the possibility of measuring the nanoparticle composition during growth. While the composition of the solid nanowire can be assumed to be unchanging after the initial solidification, the nanoparticle composition changes readily throughout the growth. When growing ternary nanowires, the compositional relationship between the liquid nanoparticle composition and the solid nanowire composition that is formed is important to investigate, to further understand how the nanoparticle dictates the nanowire composition. This aspect is further discussed in Chapter 5, and **Paper II** and **III**.

When measuring the compositions, one could think to create a compositional map using STEM XEDS, since then the nanoparticle and nanowire composition could be recorded simultaneously. However, we have to consider the temporal aspect: ideally STEM XEDS maps are acquired over many minutes up to a few hours to get enough signal. During this time the nanowire will grow, which will result in pixels in the map containing information from both the nanoparticle and the nanowire, over time. Efforts have been made to decrease the time it takes to form an adequate compositional map (**Paper vii**), however some special precautions and post-processing have to be made to make use of it. Instead, throughout this thesis, XEDS spectra have been recorded in conventional TEM mode. By focusing the beam to just contain the area/phase of interest, one can record accurate spectra with high enough counts within a couple of minutes. Measuring the nanoparticle composition involves focusing of the electron beam at the edge of the nanoparticle opposite to the nanowire, and tracking it as the nanowire grows. This is illustrated in Figure 4.5 (a) and (b), however not dynamically. This type of routine measurement has been essential for the work presented in **Paper I-IV**.

When growing ternary composition nanowires we are also interested in the solid composition being formed, and there is a set of ideal conditions that ensures that the compositional measurement is as accurate as possible. Firstly, the number of layers being illuminated by the electron beam should be as few as possible, to make sure that the compositional information recorded is local. This is because any spectrum received is a sum spectrum of the whole area currently being illuminated by the electron beam, so the highest spatial resolution is given when few layers contribute to the spectrum. For this, the stigmators of the condenser lens system are typically used to shape the beam to a flat oval instead of a circular beam, as shown in Figure 4.5 (a) and (c). This might seem unconventional, but it serves its purpose to increase the accuracy of the XEDS measurements. A second consideration is to ensure that the nanowire composition is recorded as close to on axis as possible. If not, there can be illumination of more layers than intended, in projection. Figure 4.6 illustrates this point.

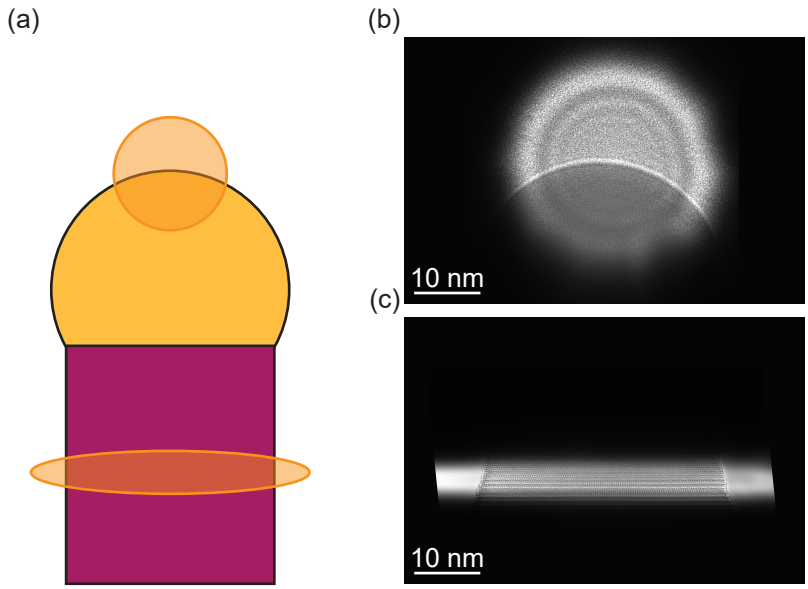

Figure 4.5: (a) A schematic detailing how the XEDS investigation of nanoparticle and nanowire is carried out, by focusing the electron beam in different spots. (b) A micrograph from a nanoparticle XEDS measurement. (c) A micrograph from a nanowire XEDS measurement. Condenser astigmatism is induced when measuring the nanowire, so that fewer layers are measured, and entire layers are illuminated. When performing studies correlating the composition of nanoparticle and nanowire, the nanowire measurement is typically carried out as close to the nanoparticle as possible.

For **Paper II** and **III** the composition of nanoparticles and nanowires were analyzed over time for Au-seeded InGaAs nanowires. Here, a procedure was followed to ensure that a similar time was spent between recording the nanoparticle and nanowire concentrations throughout the experiments. Usually, a nanoparticle XEDS spectrum was followed by flashing of the electron gun, a process that lasts for a few minutes. After the flash, an image was recorded before the recording of the nanowire XEDS spectrum. For the nanowire XEDS, the goal was often to record the composition of the nanowire as close to the nanoparticle as possible, so as to get information that can be correlated to the measured nanoparticle composition. In order to ensure that the collected signal only came from the nanowire, and not from the nanoparticle, the Au level in the spectrum was carefully monitored. The full cyclic process takes about 8-12 minutes. As we will see later in Chapter 5, the compositional data is then presented as an In/III ratio, to illustrate how the In changes in respective phase in relation to the total amount of group III elements.

When working with compositional data from XEDS it is also important to consider how much material is expected, in comparison to the sensitivity of the method. In general, the group V elements dissolve to a very low extent in the Au-based alloys investigated here, with the exception of Sb, and estimations show that As is likely never present in a

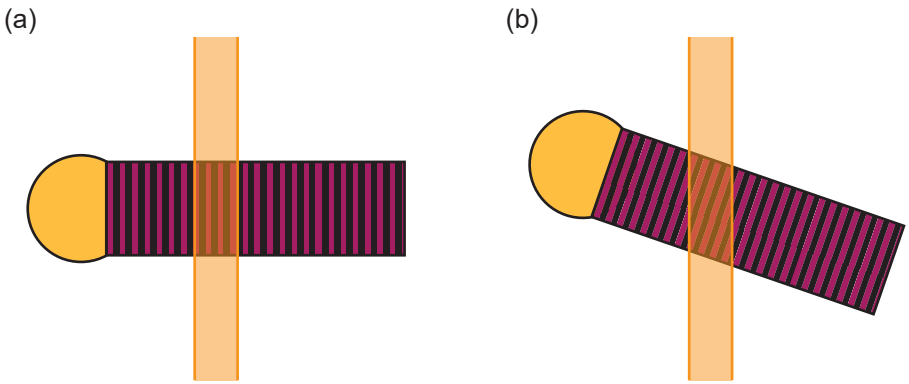

Figure 4.6: Schematic of nanowire illumination during the XEDS acquisition, detailing an on-axis nanowire (a) and a tilted nanowire (b). The nanowire is striped to illustrate the atomic layers. In (a), four purple lines are illuminated, while in (b) six different purple lines are partially illuminated. This illustrates that the XEDS information will be more localized if the nanowire is illuminated on-axis.

higher quantity than about 1 at.% (and likely even lower).[49] This puts As below the level of accurate detection from XEDS, which is roughly 1 at.%. Therefore, as we will see in the coming chapters, simulations or models are needed to determine the amount of As in the nanoparticle.

4.7 High temperature XEDS and strobe peak measurements

Since we operate at elevated temperatures and measure the composition using XEDS, it is important to know how the temperature influences the x-rays emitted from the sample. This has been extensively investigated by Tornberg et. al. and the results show that temperature can affect the emitted x-rays in mainly two ways.[106] Firstly, an elevated temperature can increase the intensity of the measured x-ray peaks. However, the effect is minimal below 550 °C. The exception is the strobe peak, or noise peak, which appears for very low x-ray energies (below 1 keV), and shows a clear increase with increasing temperature. The reason this peak increases is likely due to increased black body radiation from the sample.

The second effect is related to the deadtime of the XEDS detector. The deadtime is the time between the detector collecting x-rays and processing the data, before new x-rays can be collected, which increases if more signal is arriving at the detector per unit time. A higher deadtime gives a higher probability of sum peaks appearing in the spectrum, that are constructed when the two signals are detected at the same time by the detector, and the resulting energy will be that of the two detected energies. The effect has been observed to result in a shift and broadening of the peaks, again, especially the strobe peak. As before, the effect is small below 550 °C for other peaks. As stated earlier, the temperature we typically

use when growing nanowires is around 400 °C, so the effect on the measured signal by the elevated temperature is minimal.

As it turns out, we can utilize the shift in the strobe peak position as a means for temperature calibration. By normalizing the intensity of the strobe peak and comparing between experiments, we can measure the strobe peak at different temperatures to find which temperature matches. Therefore, this shift can be used in a constructive manner in order to make sure that the temperatures used between the experiments is similar. The results from this has shown that often a shift in temperature between 5 and 15 °C up or down has to be implemented to match separate experiments. Occasionally, chips require as much as 60 °C shifting in order to get a good match.

4.8 The droplet volume and number of atoms

Sometimes it can be beneficial to know roughly the volume of the liquid nanoparticle residing on top of the nanowire. This is also necessary in order to calculate the number of atoms in the nanoparticle. The volume can be estimated by fitting a circle to the circumference of the nanoparticle, when the nanowire is viewed edge on, as is schematically illustrated in Figure 4.7.‡

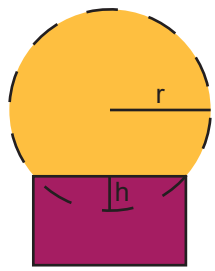

Figure 4.7: A schematic of a nanowire, where the circumference of the liquid nanoparticle is approximated by a circle of radius r. The height of the missing spherical cap, caused by the the nanoparticle not being a full sphere, is indicated by h.

The equation used for the estimation of the volume, V, is shown in Equation 4.1, where r is the radius of the droplet and h is the height of the missing spherical cap due to the presence of the nanowire. The first term equals to the full volume of the droplet, while the second term removes the volume of the missing spherical cap.

$$V = \frac{4\pi r^3}{3} - \frac{\pi h^2(3r - h)}{3} \tag{4.1}$$

‡Sometimes the droplet is more ellipsoidal rather than spherical. In those cases the height of the droplet also has to be measured separately. See supplementary information of the paper by Tornberg et. al. for further details. [109]

When the volume of the droplet has been calculated, the number of atoms of the different species in the droplet can be estimated based on compositional data from XEDS. This is done by using the average density, ρ_{avg}, and molar mass, M_{avg}, based on the composition, as shown in Equation 4.2.

$$N_x = \frac{N_A c_x V \rho_{avg}}{M_{avg}} \tag{4.2}$$

In Equation 4.2, N_x is the number of atoms of a specific species, while N_A is the Avogadro constant and c_x is the concentration of the species. Equation 4.2 is then applied to each species present in the droplet to get the total number of atoms.

4.9 Fast fourier transform

Fast fourier transform (FFT) is a post-processing analysis technique that can be used on the micrographs acquired in the TEM. Essentially it is a mathematical process that translates the image to frequency space through a fourier transform. The information is therefore very similar to what can be found from a diffraction pattern, meaning that a representation of, for example, crystal structure and defects in crystalline materials can be easily formed after an experiment, from the real-space images. An example of real space images and their corresponding FFT patterns are shown in Figure 4.8.

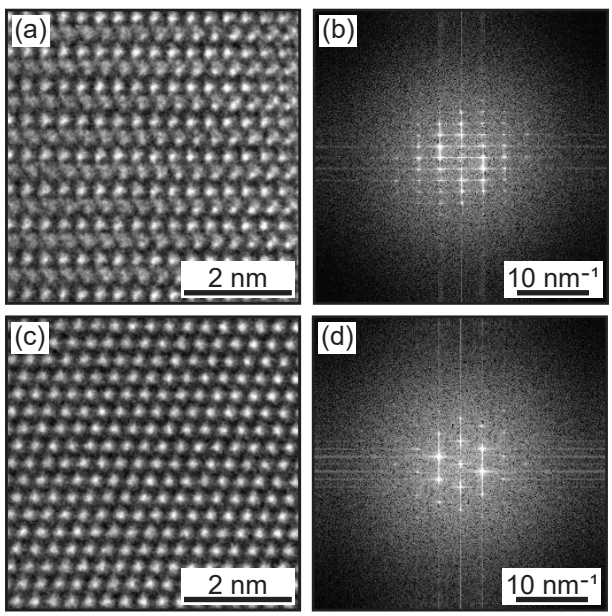

Figure 4.8: FFT patterns of crystal structures. (a) A segment of WZ imaged using HRTEM, with its corresponding FFT shown in (b). (c) A segment of ZB imaged using HRTEM, with its corresponding FFT shown in (d).

When performing *in-situ* TEM experiments, FFT can be an invaluable technique as it can be used to study the crystal structures present during fast phase transformations, where conventional diffraction is too slow and does not provide simultaneous real space images. [102] In the work presented here, FFT has mostly been used when studying interplanar distances in ternary nanowires, as will be discussed below.

4.10 Measuring interplanar distances

The different III-Vs have, as was discussed in Chapter 2, different lattice parameters for the same crystal structure, stemming from the size of the participating atoms. When growing ternary nanowires, an idea of how the composition varies can therefore be gained by measuring the interplanar distance between the layers in the axial direction. As mentioned earlier, the most common growth directions of nanowires are the $[\bar{1}\bar{1}\bar{1}]$ direction in ZB and the [0001] direction in WZ. If you then know the lattice parameters of your two binary compounds, say InAs and GaAs, you can at least qualitatively follow changes in composition between different segments by calculating the interplanar distance of the binaries in the growth direction and comparing to the interplanar distance found in the image of the nanowire. For quick measurements, even during *in-situ* experiments, the interplanar distance can be found by measuring the variation in contrast along the nanowire, typically averaged for a portion of the nanowire width. This can be directly done within the Digital Micrograph software used in conjunction with the camera, producing histograms where the interplanar distance can be measured (as shown in Figure 4.9 (a)). However, for visualization, geometric phase analysis (GPA) is used, as it can produce a color map of the interplanar distances for an entire image.

GPA is a method developed by Hÿtch et. al., [115] and has been readily used to measure strain in nanowires. [17,116,117] For that, the FFT pattern is used to reconstruct an image using specific spots, so that variations in spatial frequencies in the image can be highlighted. This can produce maps of the strain in the material in different directions, which is especially useful when investigating nanowire heterostructures. In the work presented here, GPA is used in a more crude way, as optimal orientation of the nanowires is often not achieved during growth and the main interest lies in the variations along the nanowire growth direction. Figure 4.9 shows a micrograph (a), its FFT (b) and the resulting GPA map of the interplanar distances (c).

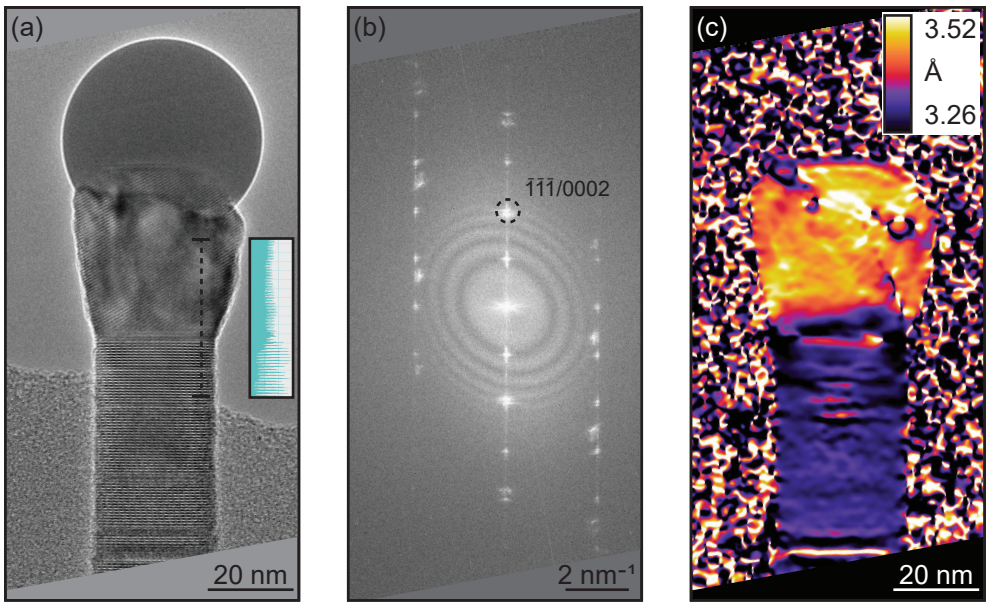

Figure 4.9: Lattice spacings of a GaAs-GaSb heterostructure. (a) The real HRTEM micrograph of a GaAs (bottom) to GaSb (top) heterostructure. The dashed line across the interface indicates the region where the histogram in the inset is constructed from. From the histogram, lattice spacings can be measured directly in the Digital Micrograph software. (b) The corresponding FFT pattern of the micrograph shown in (a). Indicated is the spot, in the growth direction of the nanowire, used to map the lattice parameter through GPA shown in (c). The color of (c) is related to the lattice spacing in the axial direction of the nanowire, where the limits roughly correspond to the interplanar distance of bulk ZB GaAs (3.26 Å) and GaSb (3.52 Å) in the [$\bar{1}\bar{1}\bar{1}$] direction.

Chapter 5

Nanowire morphology and composition imposed by the nanoparticle

The nature of VLS growth suggests that the nanoparticle has a large effect on the resulting nanowire. It is expected that what is solidified at the growth front of the nanowire has gone through the nanoparticle in some way, and therefore the internal conditions in the nanoparticle will affect the growth results. One can also tweak the diameter of the grown nanowires by changing the initial nanoparticle size, ultimately affecting the properties of the grown nanowire. In this chapter we will firstly discuss a dynamic diameter modulation observed for GaSb nanowires, where the morphology of the nanowire changes based on how much Ga is supplied and dissolved into the nanoparticle. This is the focus of **Paper I**. Then we will look at the effect the composition of the nanoparticle can have when growing ternary nanowires, in this case consisting of InGaAs, which is the focus of **Paper II** and **III**.

5.1 Nanoparticle composition affecting nanowire morphology

As has already been discussed previously, one of the core aspects of nanowires is that they exhibit a high aspect ratio and can essentially be thought of as one dimensional nanostructures. This requires control of the diameter of the grown nanowire, which will affect its usefulness in applications. For example, a common problem in nanowire growth is tapering, where radial overgrowth causes the final nanowire structure to be thick at the bottom

with gradual thinning towards the top. This occurs when there is some preference for material to solidify directly from vapor onto the nanowire surface, and is usually related to the diffusion length of the different species. This process is to a large extent governed by temperature and material flow and was mostly present throughout the studies of the InGaAs material system presented in **Paper II, III and VI**.[118]

A typical, standard nanowire will have a constant diameter along its length, since this will produce predictable properties. This is necessary, as some properties are strongly affected by the nanowire diameter.[119,120,121] However, ideally one would want to be able to control the diameter along the nanowire in order to create specific nanostructures for e.g. enhanced light absorption.[122] When studying the GaSb nanowire system, we realized that we could achieve such a diameter modulation by altering the flows in the environmental transmission electron microscope. This was the subject of **Paper I** and will be discussed here.

5.1.1 The Au-Ga-Sb nanoparticle composition and size

Our main study of the Au-seeded GaSb system involved controlled adjustments of the precursor flows and the observation of the resulting effects this created. One such aspect that has been discussed previously is the nanoparticle composition. By our initial trials we knew that steady and stable nanowire growth could be achieved with nanoparticle compositions where Ga was around 70 at.%. In order to get a deeper understanding of the stability of the growth, we wanted to investigate how this composition changed with the precursor flows and what the limits were in terms of continued axial growth. We therefore decided to make two flow series, one for the TMGa flow and one for the TMSb flow, where the composition of the nanoparticle would be followed as either of the precursor flows was changed. Throughout the series, the flow of the other precursor would be held constant, and the system was allowed to stabilize for 10-15 minutes after any changes were made to the gaseous composition before any spectra were acquired. The results of the study of the composition can be seen in Figure 5.1.

As can be seen in Figure 5.1 (a), the two flow series follow each other closely when plotting the results with respect to the supplied V/III ratio. If we only consider the TMGa series firstly (striped markers in Figure 5.1 (a)), we will see that there are four separate experimental datapoints showing the composition of the nanoparticle at different TMGa flows, with stationary TMSb flow. As expected, the Ga concentration in the nanoparticle increases for an increasing TMGa flow, with the lowest measured concentration being around 70 at.% and the highest being above 95 at.%. At the same time, the Sb concentration remains relatively unchanged, measured to be between 3 and 5 at.%. This representation of the nanoparticle fails to highlight two important aspects: for one, the nanoparticle is swelling towards lower V/III ratios, for most of the range studied. This effect will be discussed further in this chapter. Secondly, due to the swelling, the absolute number of atoms

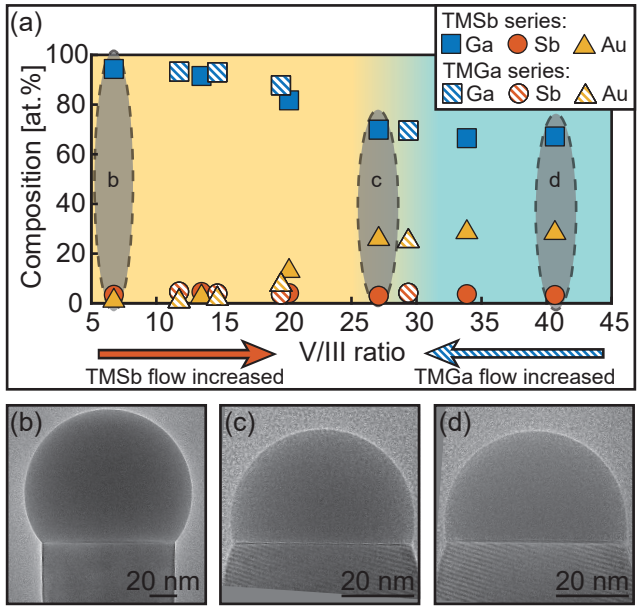

Figure 5.1: Au-based nanoparticle composition and size depending on the supplied V/III ratio, for Au seeded GaSb nanowires. (a) The composition measured via XEDS throughout the two flow series. The graph is divided into a regime of stable composition (cyan) and a regime of dynamic composition (yellow). (b)-(d) The size of the nanoparticle as it changes throughout the TMSb series, where the frames are acquired under the V/III ratios illustrated by the shaded areas in (a). Figure adapted from **Paper I**.

can change drastically within the nanoparticle for different flows, even if the concentration appears to be similar. This will be important to study further in Chapter 6, where we will discuss the layer dynamics of the GaSb nanowire growth in light of the results presented in **Paper IV**.

If we again look at the TMGa series presented in Figure 5.1 (a), we will see that the range investigated is smaller than for the TMSb series. This is in part due to the fact that in the range of flows we were investigating, the GHS did not allow as small (controlled) changes to the TMGa flow as compared to the TMSb flow. However, for lower TMGa flows we did not observe axial growth of the nanowire, and for higher flows the nanoparticle was depinning from the top facet due to its size. This means that even if the stable growth could be pushed slightly further to the extremes of the graph (as for the TMSb series) we investigated most of the useful range achievable for our growth parameter space.

Looking instead at the TMSb series in Figure 5.1 (a), we see that a part of the series is within the yellow region of the graph, while a part is within the cyan region. This distinction was made in order to separate the V/III ratios where we observed changes to the nanoparticle in terms of size and composition (yellow), and the V/III ratios where such attributes were mostly stable (cyan). The stable and dynamic regimes will frequently be referred to when

discussing the observed effects in the GaSb growth system, both in this chapter and Chapter 6.

In the yellow region, we see a similar behavior to the decrease of TMSb as we observed for an increase in TMGa: the nanoparticle swells, as is illustrated by Figure 5.1 (b) and (c). However, throughout the cyan region the nanoparticle is stable in volume, even though the TMSb flow is further increased (compare Figure 5.1 (c) and (d)). Now, since the main part of the nanoparticle consists of Ga, a hypothesis that can be made at this point is that the flow of TMSb influences the ability for the nanoparticle to accumulate Ga. As will be discussed in Chapter 6, another explanation could be related to a shift from nanoparticle assisted growth to increased surface growth and radial growth as TMSb is increased.

5.1.2 Nanowire diameter imposed by the nanoparticle

As we discussed in the previous section, the nanoparticle volume readily changed with the flows of precursor materials. This change in volume imposed a similar change in nanowire diameter, which adjusted to accommodate the nanoparticle. As was discussed in Chapter 2, the wetting angle of a nanoparticle on a substrate will be strongly affected by the surface energies of the system, but in the case of nanowire growth, the nanoparticle is also pinned and limited by the nanowire diameter. The energetics of such a system has been investigated previously, and is obviously more complex than for a nanoparticle on a flat surface.[109,123] On a flat surface, the force the nanoparticle exerts on the substrate only changes the extent of the nanoparticle, while in the case of a nanowire this can force the diameter of the interface to expand.

The resulting nanowire diameter change as a function of V/III ratio in the two series, measured at the nanoparticle-nanowire interface, is presented in Figure 5.2 (a). In a similar fashion as for Figure 5.1, the graph is split into two regions representing dynamic and steady nanowire diameter, respectively. As the nanowire changed we observed the quick formation of mostly straight side facets as the system stabilized, which can be seen in Figure 5.2 (b) and (c), where the nanowires of the two series are shown at the end of the experiment. What was interesting was how these facets would remain stable even as the growth progressed at new growth conditions, enabling us to create the diameter modulated nanowire structures shown in Figure 5.2 (b) and (c).

Although the GaSb showed a modulated resulting structure, the initial GaAs nanowire stem was often overgrown during growth. Such preferential overgrowth can be interesting for certain applications.[124] However, in our case, it was unwanted and observed to occur to a larger extent for higher V/III ratios. This can be related to the constant diameter regime in Figure 5.2 (a), where the surrounding growth conditions seem to induce a preference for GaAs overgrowth. This will be discussed further when the growth dynamics of GaSb are

presented in Chapter 6.

In summary, we have here explored how nanoparticle composition and volume can be affected by the precursor gas supply, and how this, in turn, can affect the nanowire morphology. In this case, the effect on the nanowire was governed by the increase in the nanoparticle volume, as it pulled the sides of the nanowire, changing its diameter.

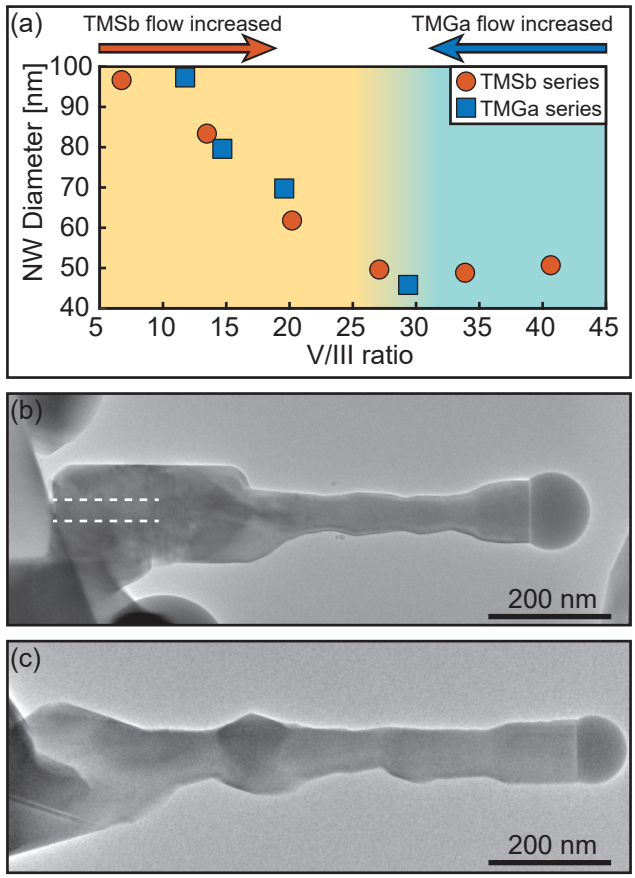

Figure 5.2: Diameter at the nanoparticle-nanowire interface for steady-state conditions during Au seeded GaSb growth. (a) The diameter dependency on V/III ratio, divided into a stable diameter regime (cyan) and a dynamic diameter regime (yellow). (b)-(c) The appearance of the nanowires investigated throughout the TMSb (b) and the TMGa (c) flow series. The dashed lines in (b) indicate the position of the initial GaAs segment, which was overgrown throughout the TMSb flow series. Figure adapted from **Paper I**.

5.2 Nanoparticle and nanowire compositional relationship

For ternary semiconductor nanowires containing more than one group III or group V element, the composition throughout the nanowire is important as it dictates its electrical and optical properties, as discussed in Chapter 2.[72,125,126] For specific applications, a stable ternary composition, or inclusions with controlled composition, is required throughout the nanowire. For ternaries containing two group III elements, such as InGaAs, the resulting composition is expected to be especially influenced by the nanoparticle composition, as the group III elements have a high solubility in Au and may therefore linger in the nanoparticle even after the supply of the element is turned off.

To investigate the compositional relationship between the nanoparticle and the nanowire, InGaAs nanowires have been studied in **Paper II** and **III**. **Paper II** highlights the compositional trends seen for a large number of nanoparticles and their associated nanowires, and will be discussed firstly. For **Paper III** specific nanoparticles and their resulting nanowires were studied in detail in terms of the compositional evolution from growth initiation, and compared to thermodynamic simulations. This will be discussed towards the end of the chapter.

5.2.1 Compositional trends in Au-seeded InGaAs nanowires

In order to study the trends of compositional evolution for ternary InGaAs nanowires, InGaAs was nucleated directly from Au, as described in Chapter 4, and studied as the growth progressed. By carefully following the procedure of compositional measurements outlined in Chapter 4, the nanoparticle and nanowire compositions were measured in a careful manner as the growth evolved, eventually resulting in the graph presented in Figure 5.3.

Figure 5.3 shows the nanoparticle In/III composition on the y-axis with the nanowire In/III composition on the x-axis. This representation is convenient to illustrate the relative amounts of In as compared to Ga in the two respective phases, and has been used in several earlier theoretical investigations of ternary InGaAs nanowires.[75,127,128,129,130] Firstly, it becomes evident that a large amount of the total group III in the nanoparticle has to be indium in order for any indium to be incorporated into the growing nanowire. This can be clearly seen in the left side of Figure 5.3, where the In/III ratio in the nanowire stays below 0.1, while the nanoparticle spans most of the compositional range. At about 0.8 in nanoparticle composition, the first real incorporation of In into the nanowire is seen. At this point, the nanoparticle composition almost plateaus, showing little increase while the nanowire composition instead spans most of the compositional range. For higher nanowire compositions there is again a slight increase in nanoparticle composition to push the growth towards pure

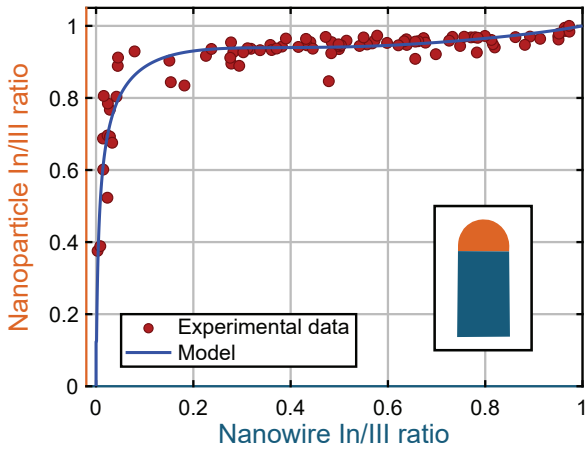

Figure 5.3: The compositional relationship between nanoparticle and nanowire for Au-seeded InGaAs. The y-axis shows the In/III ratio for the nanoparticle, while the x-axis shows the In/III ratio for the nanowire, color coded similarly to the schematic inset. In the graph, both experimental data (red circles) as well as model results (blue line) are shown. Figure adapted from **Paper II**

InAs growth. In terms of real compositional quantification from XEDS, the In content in the nanoparticle typically reaches 30-40 at.% before any significant incorporation into the nanowire occurs.

The overall trends of the curve shown in Figure 5.3 are in good agreement with the earlier theoretical studies.[75,127,128,129,130] However, one of the important aspects of the trend observed in Figure 5.3 is the fact that we observed compositions across the entire compositional range. From a pure thermodynamic perspective, most of the intermediate compositions in InGaAs should be unstable, due to the presence of a miscibility gap at temperatures lower than 543 °C.[75] Since the growth here was carried out at 380 °C, there should therefore be no homogeneous compositions between roughly 0.2 and 0.9 in nanowire compositions. Of course, such compositions have been observed before in InGaAs nanowires,[72] so the fact that solid compositions that are unstable in bulk can be achieved in the nanowire morphology is not new. That being said, the demonstration of compositions across the entirety of the compositional range is important for our understanding of the compositional control.

Since the earlier theoretical models had predicted the experimental trends, we wanted to see if we could construct a new model that had an ever better match to the experimental data. The new model was based on the model presented by Leshchenko et. al.[127] The resulting model is indicated by the blue line among the experimental datapoints in Figure 5.3, and reproduces the experimentally determined compositional relationship to a high degree. The equation for the model is shown in Equation 5.1.

$$\frac{1-x}{x} = K\frac{1-y}{y}\,\frac{1-e^{-\Delta\mu_{GaAs}+\sigma_{GaAs}}}{1-e^{-\Delta\mu_{InAs}+\sigma_{InAs}}} \tag{5.1}$$

In Equation 5.1, x and y are the solid and liquid In/III ratios, respectively, K is the ratio between attachment coefficients of GaAs and InAs pairs, the $\Delta\mu$ are supersaturations and the σ are surface energy terms, where the list of values and expressions used can be found in the Supplementary Information of **Paper II**.

There are a few important aspects about the model that enables it to accurately represent the experimental data. For one, a main component of the model is the ratio between attachment coefficients which essentially is a kinetic aspect of the nanowire growth rather than a thermodynamic. Several earlier studies have reported on the suppression of miscibility gaps when predicting the solid composition based on attachment rates, rather than only considering the composition of the critical nucleus based on thermodynamics.[128,130] Therefore it made sense to include such an aspect also here, as experimentally determined compositions were regularly found to be within the miscibility gap. Another implemented aspect was a composition dependent As concentration, c_{As}, that changes with the amount of dissolved indium in the nanoparticle, as given by Equation 5.2 where y again is the liquid In/III ratio.

$$c_{As} = 10^{-4}\, e^{2.8y^2} \tag{5.2}$$

The possibility of achieving any solid composition in the ternary nanowire is important from a device perspective, where specific compositions can be used to achieve tailored properties such as bandgap matching. However, from a growth perspective, the fact that the entire range of intermediate compositions in Figure 5.3 forms under very similar nanoparticle compositions is a problem. This indicates that the system could be very sensitive to small fluctuations in flow, that translates into nanoparticle composition and eventually into nanowire composition.

An important aspect of the results presented here is the interplay between the two group III elements in the nanoparticle. That such a high amount of In is needed in the nanoparticle in order to see any incorporation into the nanowire indicates that the chemical potential increase with addition of In in the nanoparticle is small. Alternatively, one can see this as In having an effect on the supersaturation of GaAs: when more In is incorporated, GaAs becomes more supersaturated and therefore grows out, leading to a decrease in Ga concentration in the nanoparticle. The nanoparticle really needs to be rid of most Ga in order to grow pure InAs, while pure GaAs can be achieved with as much as 80 % of the total group III being In. Such aspects are explored further in **Paper III** and the rest of this chapter.

5.2.2 Temporal evolution of singular InGaAs nanowires

While a statistically large set of correlated compositions between nanoparticle and nanowire can give us insights about the trends, there is also value to further investigate individual cases. This was the main topic of **Paper III**, where further details of the growth of ternary InGaAs nanowires could be extracted by carefully following the growth of individual nanowires over time, as they transitioned from GaAs rich to InAs rich. The InGaAs nanowires were grown from GaAs stems as outlined in Chapter 4, but, as will be shown later, the nanoparticles often contained some amount of In prior to the initiation of the In supply. The resulting data from a specific nanowire that will be discussed extensively is shown in Figure 5.4.

Firstly, we will discuss some general aspects of Figure 5.4 and its related nanowire. All plots are related by their common x-axis representing time, and denote how the specific attribute evolves over time. In this case, the nanowire was investigated for roughly 7000 s, where time 0 indicates when the gas supply was changed from only providing TMGa and AsH_3 for GaAs growth to also include TMIn for ternary InGaAs growth. This timescale might seem arbitrary, however we must remember the nature of the *in-situ* investigations used throughout the thesis: the time for possible investigation of a single nanowire is not infinite during growth. In this case, the nanowire was lost by means of collision with surrounding material growing on the surface. Around the time when the gaseous composition was changed, the temperature was also changed from 420 °C to 380 °C.

Figure 5.4 (a) shows the nanoparticle composition as it evolves over time. Importantly, the nanoparticle already contained around 10 at.% In at the start of the measurements. Ideally, the nanoparticle should have been clean from any In at the start of the experiment, but it turns out that In is an efficient contaminant and can linger for weeks in the system. One of the temporal aspects we wanted to investigate was the build-up of indium in the nanoparticle over time, which was complicated by this lingering property of In. However, since the amount of In seemed to be too low for any incorporation into the nanowire to occur, as is shown in Figure 5.4 (d), we could still work around the contamination issue.

If we follow the composition presented in Figure 5.4 (a) over time, we see that the Ga level steadily decreases until around 4000 s where it starts to stabilize. Simultaneously, the amount of dissolved In increases. This can be explained by an exchange mechanism in the nanoparticle, where Ga is removed so that more In can be incorporated. Eventually, Ga reaches a stable value, while In continues to accumulate. The exchange of group III material and further accumulation of indium results in an increase in nanoparticle volume as can be seen in Figure 5.4 (b).

In **Paper II** an expression for the concentration of As in the nanoparticle was derived, since the As amount in the nanoparticle is too low to be measured experimentally. The same

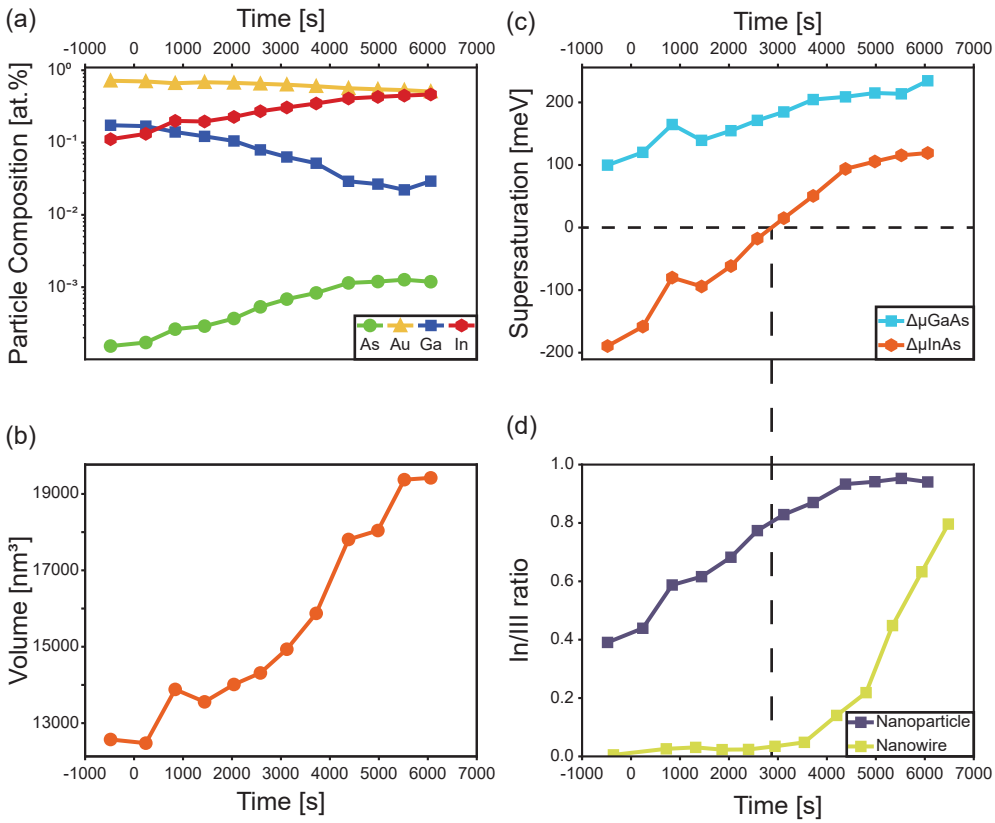

Figure 5.4: A study of a singular InGaAs nanowire grown from a GaAs stem over time, where time 0 indicates the start of the TMIn supply (while keeping TMGa and AsH_3 on). (a) The composition in the nanoparticle as it evolves over time. As can be seen, the nanoparticle already contained some In at the start of the investigation. (b) The volume of the droplet over time. (c) The calculated supersaturation for the two III-V binaries. (d) The In/III ratio in both nanoparticle and nanowire as it evolves. As can be seen, the nanowire was pure GaAs at the start of the experiment.

expression was used in the construction of Figure 5.4 (a), which shows that As therefore increases steadily with the amount of In in the nanoparticle. This is important when considering Figure 5.4 (c), where the calculated supersaturation of the binary compounds dissolved in the nanoparticle with respect to the solid species is shown. In this graph, we show how the supersaturations $\Delta\mu$GaAs and $\Delta\mu$InAs change over time, depending on the measured composition (calculated in the case of As). Notably, the GaAs supersaturation is always larger than the InAs supersaturation, indicating that there is always a higher driving force for GaAs to solidify. However, as can be seen in Figure 5.4 (d), where the In/III ratio in nanoparticle and nanowire is shown, the nanowire will eventually incorporate InAs. Our temporal resolution (minutes between measurements and measurements that are averages over a few minutes) hides the finer details of how the supersaturation varies during the step-flow and incubation growth processes, but at least gives an idea of the supersaturation

level.

If we again look at Figure 5.4 (c), we see that around 3000 s the InAs supersaturation surpasses 0 meV, effectively showing that there is a driving force to incorporate InAs into the growing solid. The same time is marked in Figure 5.4 (d). What can be seen in Figure 5.4 (d) is that the nanowire has not incorporated any In for times below 3000 s, but when the supersaturation passes 0 meV the nanowire starts to incorporate In shortly after. At this point the nanoparticle has surpassed an In/III ratio of about 0.8, as can be seen in Figure 5.4 (d). The fact that the nanoparticle requires an In/III ratio higher than 0.8 in order for any In to be incorporated into the nanowire is already known from earlier in this chapter and **Paper II**. However, the current investigation shows the onset of In incorporation in a more quantifiable manner, through the use of supersaturations.

In Figure 5.5 another nanowire has been studied in a similar way as was demonstrated in Figure 5.4, with the intent of analyzing the nanoparticle and nanowire stabilization process. Here, only the supersaturation and the In/III ratios are presented, in Figure 5.5 (a) and (b), respectively, and the x-axis in both cases shows the grown nanowire length.

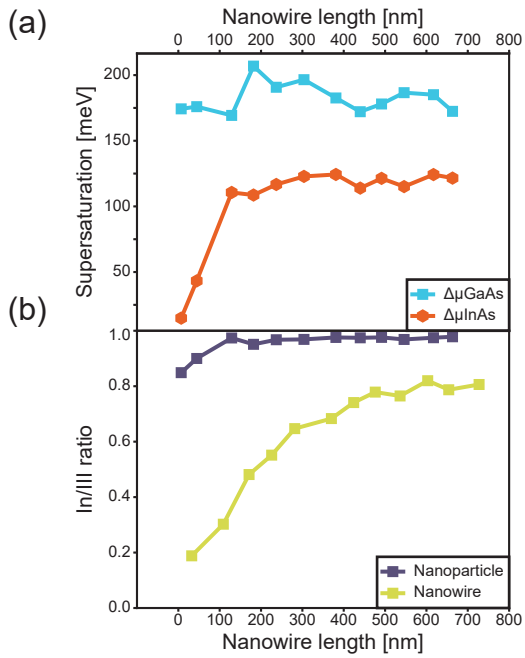

Figure 5.5: A study of the evolution of a nanowire as it is growing, presented as a function of the grown length. (a) The supersaturation of GaAs and InAs. (b) The In/III ratios measured in the nanoparticle and nanowire.

In Figure 5.5 (b), it can be seen that the nanoparticle already contains In at the start of the experiment (giving an In/III ratio of more than 0.8), and the nanowire also contains a low

amount of In. However, the nanoparticle composition was not yet stable at the start of the experiment, as can be seen in the InAs supersaturation curve in Figure 5.5 (a). This changes quickly, and the supersaturation stabilizes after little more than 100 nm. Importantly, the stabilization of the nanoparticle InAs supersaturation occurs at a point where the nanowire only has achieved an In/III ratio of about 0.4. The nanowire then continues to become more In rich over the course of the next 300-400 nm, eventually stabilizing around an In/III ratio of 0.8. Throughout this period, the supersaturation shows a relatively stable behavior. This indicates that, other than the momentary nanoparticle composition and supersaturation, there may exist another factor influencing the solidified compositions in the nanowire. We expect that this factor is related to the compositional history of the nanowire, where the strain imposed by the preceding layers plays a role. In order to investigate this, simulations of the nanowire growth were also carried out.

5.2.3 Simulating the compositional evolution of InGaAs nanowires

The evolution of InGaAs nanowires was simulated using the simulation framework developed by Mårtensson et. al. [131] The simulation considers the transport of individual atoms within the system as they move between the present vapor, liquid and solid phases. The system constantly evaluates the probability of any process occurring by performing the change, calculating the change in Gibbs free energy and then comparing the results to find which process is the most likely to occur. It then uses random numbers to decide the outcome, which effectively emulates real growth results. This way, the growth of InGaAs nanowires can be studied in great detail, with full disclosure of the movement of atoms and the resulting influence on, for example, composition within the nanoparticle and nanowire. A full description of the model can be found in. [131,132]

The present simulation was performed with the intention of studying the evolution of an InGaAs segment as the surrounding conditions were changed from pure GaAs growth conditions, similarly to the experiments discussed in the previous section. As such, pure GaAs was grown for 10 s, before a supply of In was activated. Figure 5.6 (a) illustrates the evolution of the supersaturation, while Figure 5.6 (b) shows the composition in the nanoparticle and Figure 5.6 (c) details the In/III ratio in nanoparticle and nanowire. A major difference between the experimental investigation and the simulation, is that the surrounding conditions have been set so as to promote faster changes and growth in the simulation. The major reason for this decision is the long computation times, owing to the sequential determination of every single atomic-scale process that occurs in the system. Therefore, similar growth times as the experimental investigation are not feasible.

When comparing the compositional evolution of the nanoparticle in the simulation, as shown in Figure 5.6 (b), to the experimentally measured nanoparticle composition in Figure 5.4 (a), many similarities are found. Both graphs show a build-up of In in the nanoparticle,

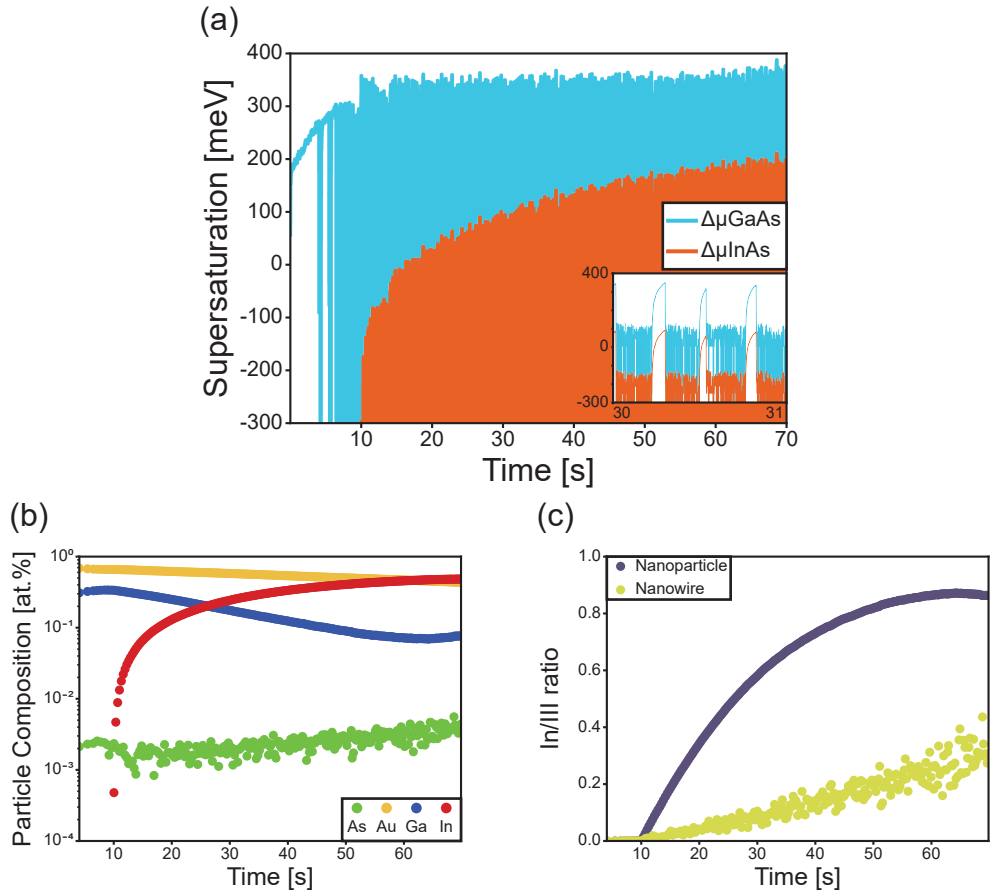

Figure 5.6: Simulation results of the evolution of Au-seeded InGaAs nanowires, grown from GaAs stems. The In supply was initiated at t = 10 s. (a) The supersaturation of GaAs and InAs. The inset shows the same range, but for a magnified timescale. (b) The nanoparticle composition. (c) The nanoparticle and nanowire In/III ratios. The data in (b) and (c) are plotted for nucleations, while the data in (a) is plotted in a continuous manner.

while the amount of Ga diminishes. As In increases, the concentration of As follows. In both cases, the Ga concentration eventually stabilizes. The simulated nanoparticle composition gives rise to the InAs and GaAs supersaturation behavior presented in Figure 5.6 (a). Here, the InAs supersaturation sharply increases initially, after which a slower increase is seen until it flattens towards the end of the simulation. The GaAs supersaturation mostly appears flat once In is supplied to the system. The inset shows a magnified view of the supersaturation, for a single second of simulation. Here, sharp peaks in the supersaturation of both binary compounds are seen, with "flat" regions in between. The peaks correspond to incubation periods, whereas the regions in between correspond to the step-flow. Once nucleation occurs (the sharp decrease from the peaks), the supersaturation drops significantly, as the nanoparticle is depleted of As and relies on further supply from the vapor. Such fine

details of the supersaturation behavior were of course impossible to record experimentally.

Finally, the composition in the nanoparticle and nanowire as presented by the In/III ratio is detailed in Figure 5.6 (c), where the stabilization of the nanoparticle composition once again can be seen. As more In is being dissolved in the nanoparticle, the In/III ratio in the nanowire starts to increase. The onset of In incorporation into the nanowire occurs for a lower In/III ratio in the nanoparticle in the simulation than what was observed experimentally in Figure 5.4 (d). However, the used growth conditions in the simulation lead to the supersaturation crossing the 0-value already when the In/III ratio is about 0.2 in the nanoparticle. This is expected to be caused by the high As flow in the simulation, which results in a high growth rate, but also higher supersaturation. The incorporation of In into the nanowire shows a similar behavior as was shown experimentally in Figure 5.5 (b), with a relatively low amount of In incorporated even as the supersaturation starts to stabilize. Interestingly, the grown layers start to show significant spread in composition as the composition progresses deeper into the miscibility gap of InGaAs.

The simulation and experiments demonstrate similar results regarding the compositional evolution of InGaAs nanowires. An interesting aspect of the simulation framework is that it comes with several optional rules that can be enabled for the growth. There are two etching rules, the layer etching rule (LER) and the propagation etching rule (PER), where LER prevents etching of completed layers and PER prevents etching of any atomic pair except the one that was added to the growing layer the latest. There is also an optional strain factor, which can be tweaked in magnitude, that emulates a strain acting on each layer based on the composition of the previous 8 layers in the nanowire with diminishing effect. For the simulations presented here, all three rules were used. Simulations were also performed were either only PER was enabled or only PER was disabled. The simulation with only PER resulted in similar results as shown in Figure 5.6, but with a more narrow spread in solid compositions formed deeper in the miscibility gap. The simulations without PER instead show a sharp increase in solid compositions once In is supplied, followed by a long region where the solidified compositions do not change significantly. It was concluded that the simulation presented in Figure 5.6 is the most accurate, since the change in composition follows the experimentally observed trends, while showing a significant spread in solidified compositions for similar supersaturations.

5.2.4 Concluding remarks on compositional control in InGaAs nanowires

Paper II and **III** both demonstrate important aspects of the compositional behavior of InGaAs nanowires. While the investigation carried out in **Paper II** is more simple and straightforward, it demonstrates the important aspect that a high In/III ratio is needed in the nanoparticle in order to see high incorporation of In into the growing nanowire. **Paper III** takes this one step further, and identifies that a clear onset of In incorporation can

be observed as the supersaturation of InAs in the nanoparticle increases to positive values. However, through the study of the growth of individual nanowires experimentally and through simulations, **Paper III** demonstrates that the supersaturation in the nanoparticle is not the only aspect determining the solidified composition. Since the supersaturation was found to stabilize while the nanowire was still evolving in composition, the conclusion is that the rest of the solid nanowire also influences the composition being solidified. Ideally, more simulations should be carried out in order to investigate also the stabilization of the nanowire composition. Importantly, the *in-situ* experimental investigation can give valuable input into how the simulation parameters should be changed for the simulation to give valuable results that are comparable to real growth.

Chapter 6

Layer growth dynamics in nanowires

The layer-by-layer growth process of nanowires as described in Chapter 2 might seem simple enough: material is accumulated into the nanoparticle until a sufficient driving force for solidification is achieved. However, the process is in reality quite intricate and the time needed to complete the two sub-processes, incubation and step-flow, depends on all the experimental parameters we have discussed up until now. In order to get a deeper understanding of the nanowire growth process, the layer dynamics have therefore been studied in detail in **Paper IV, V** and **VI**. As we will see throughout this chapter, the layer-by-layer growth process can change in many ways when individual precursor flows are varied, or when different crystal structures or crystallographic defects are formed. Sometimes, a deviation from the traditional layer-by-layer growth has also been observed, leading to multilayer growth, which can impact the compositional and morphological control discussed in the previous chapter. We will start by discussing the layer growth dynamics of GaSb nanowires, highlighting the main results from **Paper IV**.

6.1 Experimental study of GaSb nanowire growth behavior

The growth of GaSb has already been described in Chapter 4 and discussed in Chapter 5, where in the latter, the focus was on the nanoparticle volume, composition and the resulting diameter modulation of the GaSb nanowires. The investigation showed, among other things, that the nanoparticle switched between a stable and dynamic composition regime as the V/III ratio was changed. Videos were also recorded throughout the experiments, where the step-flow and incubation times, and their dependency on the two precursor flows, could be followed for steady-state conditions. The resulting step-flow and incubation times are

shown in Figure 6.1.

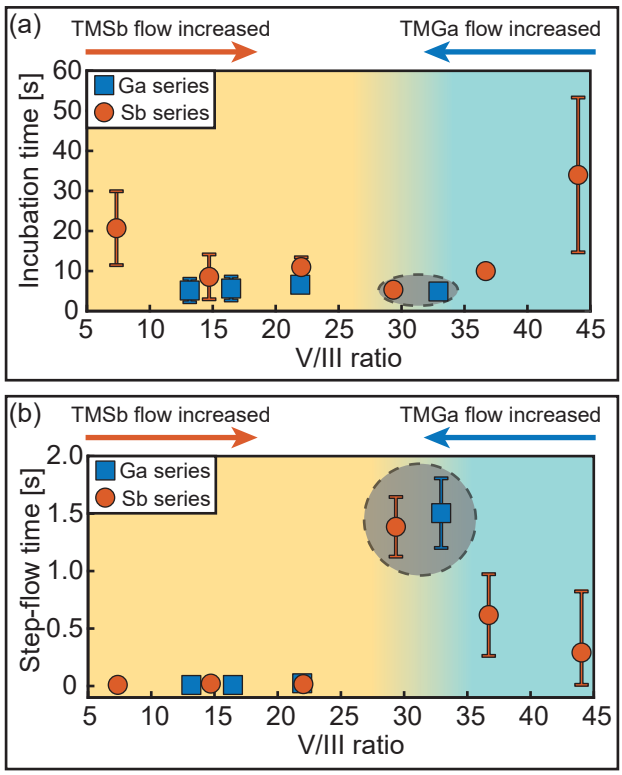

Figure 6.1: The step-flow and incubation data from the Au-seeded GaSb experimental investigation. (a) The incubation data for the two investigated flow series. (b) The step-flow data for the two investigated flow series. Both graphs are color coded based on the aforementioned stable (cyan) vs dynamic (yellow) diameter and composition regimes (Chapter 5). The gray ovals in both graphs indicate where the growth conditions for the two series should overlap based on flows, with a slight discrepancy in V/III ratio based on growth chamber geometry in the two experiments.

What can be seen in Figure 6.1 is that when the precursors are varied independently of each other, the produced trend in incubation and step-flow with V/III ratio is very similar. The incubation time shown in Figure 6.1 (a) seems to be stable around 10 s for intermediate V/III ratios, but increase for both low and high V/III ratios, even throughout the stable composition regime. The step-flow, shown in Figure 6.1 (b), on the other hand has a peak at the border between the two regimes, and decreases on both sides. Interestingly, the step-flow time decreases so much towards lower V/III that our camera could not temporally resolve the step-flow process (operated at 100 frames per second (FPS)), forcing us to deem it as instant.

The increase in incubation time for lower V/III ratio in the TMSb series is easy to understand: as the TMSb flow is decreased, less material is supplied to the nanoparticle and it therefore takes longer time to reach supersaturation. In this regime the incubation is there-

fore Sb supply limited, and a longer time is needed to overcome the supersaturation barrier. For high V/III, in the stable regime, we have to consider other effects that occurred on the chip. As was mentioned in Chapter 5, we observed overgrowth of GaAs for high V/III ratios. This would be a material sink, and could therefore lead to the increase in incubation time observed in the stable composition regime, even though Sb should be abundant and intuitively decrease the incubation time. Since the overgrowth would also consume the available Ga in the system, it is difficult to discern whether the incubation is limited by TMSb or TMGa at high V/III ratios.

In order to understand the emergence of the instant step-flow, we have to consider the nanoparticle. We already know from **Paper I** that the concentration of Sb is low, on the order of a few percent, but we also know that the volume of the nanoparticle changes a lot throughout the dynamic composition regime. The volume of the nanoparticle throughout both flow series is shown in Figure 6.2 (a). As the volume is changing, the number of atoms in the nanoparticle will also change, an aspect that may be hidden by only looking at the compositional data. Therefore, we use the volume to translate the composition shown in Figure 5.1 (a) to number of atoms, as displayed in Figure 6.2 (b) (normalized to the number of Au atoms). The calculation was carried out in the same manner as presented in Chapter 4.

In Figure 6.2 (b) we see that the number of atoms is comparable throughout the stable composition regime, but increases rapidly across the dynamic composition regime. This shows that even though the concentration of Sb in the nanoparticle appeared constant in Figure 5.1 (a), the absolute number of Sb atoms changes dramatically as the volume of the nanoparticle changes. Step-flow has, for GaAs, been shown to be a process that is dependent on material availability, where the step-flow will be initially fast until the nanoparticle is depleted, upon which it has to rely on the continued delivery of material from the vapor.[58] This suggests that there needs to exist a sufficient amount of dissolved elements in the nanoparticle to facilitate instant step-flow. We know that Ga exists in a surplus, however, the amount of Sb in the nanoparticle for high V/III ratios is relatively low. We therefore expect the nanoparticle to become "depleted" of Sb during the step-flow process in the stable composition regime. It is therefore not thermodynamically favorable for the nanoparticle to lose more of its dissolved Sb, and the continued step-flow therefore has to rely on material delivery from the surrounding vapor in order to complete the step-flow. This would also explain the decrease in step-flow, when the V/III ratio is increased from 30 to 45 (see Figure 6.1 (b)). The nanoparticle contains roughly the same number of Sb atoms, but the delivery of material is higher for the higher V/III ratio cases, effectively decreasing the step-flow time.

By calculating the ratio between the number of Sb atoms present in the nanoparticle and the amount needed to fill a full layer we can get a more clear picture of how much Sb is needed to produce an instant step-flow. This is presented in Figure 6.3, both in relation to

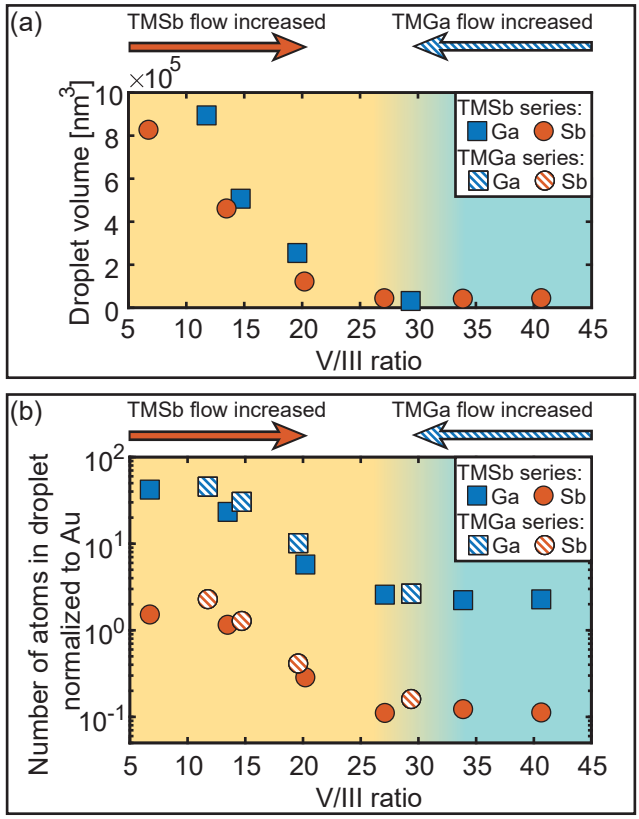

Figure 6.2: (a) The volume of the nanoparticle as a function of V/III ratio for Au-seeded GaSb growth. (b) A recalculation from concentration to number of atoms dissolved in the nanoparticle. The values are normalized to the amount of Au. The graphs are color coded based on the aforementioned stable (cyan) and dynamic (yellow) diameter and composition regimes.

the V/III ratio (a) and the step-flow time (b). Figure 6.3 (b) shows that there likely needs to be at least 15 times more Sb present in the nanoparticle than what is needed to complete a full layer, for the step-flow to become instant.

The discussion so far has shown that the experimental investigation suggests that incubation is largely TMSb limited, with some unclear effects happening at the high V/III ratios, possibly due to surface growth. Step-flow has been shown to depend on Sb availability, where instant step-flow is seen when there is a sufficient amount of Sb dissolved in the droplet. For higher V/III ratios, in the constant regime, the amount of available Sb is lower, and the step-flow will here instead rely on the delivery of Sb from the vapor, resulting in a decrease in step-flow for higher V/III ratios. In order to establish and further explore the trends observed experimentally, the growth of GaSb nanowires was also studied through simulations, as shown in the next section.

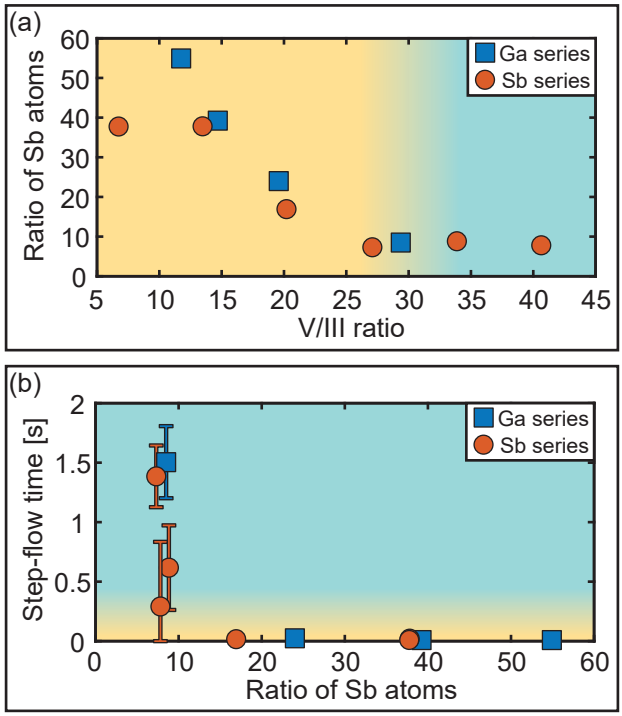

Figure 6.3: The ratio between the number of Sb atoms present in the nanoparticle as compared to the amount needed to cover the entire liquid-solid interface with a full solid layer. (a) The ratio as a function of V/III ratio. (b) The ratio related to the resulting step-flow time. Both graphs are color coded based on the aforementioned stable (cyan) vs dynamic (yellow) diameter and composition regimes.

6.2 Modeling of GaSb nanowire growth

As a complementary study, the layer-by-layer growth of GaSb was also studied by means of a Monte Carlo-based nanowire growth simulation in **Paper IV**. The simulation is based on the framework built by Maliakkal et. al., where the growth of GaAs was simulated and compared to *in-situ* experimental results.[58] The simulation works by calculating the impingement of Ga and Sb into the nanoparticle based on impingement rates, and then calculating the probability of forming a new layer based on nucleation theory. The simulation then uses random numbers in order to determine the outcome. This way, the growth of the GaSb nanowires is evaluated in set time steps, typically 1 ms, and the evolution of several different properties can be followed, as will be shown below.

6.2.1 Inputs to the simulation and ensuring stability

Any simulation framework operates under a number of input parameters that can be tweaked based on the results or to fit experimentally acquired data. In our case, we wanted to accurately model the growth based on the conditions used, and the results observed, during the experiments, where the goal was always to measure the step-flow, incubation, etc. under steady-state conditions. The experimentally measured concentrations, with the number of Au atoms calculated to give a baseline for the actual number of atoms, were used as input for the model. The total number of atoms determines the volume of the nanoparticle, which was always compared to the experimentally determined volume to make sure that they were similar. In the end, the actual concentrations had to be slightly adjusted based on the resulting droplet volume and the stability of the simulated growth. An assumption was also made to keep the number of Au atoms constant when simulating the two flow series, as there is no supply of Au and we do not expect any incorporation of Au into the nanowire that would significantly change the size of the system.[43] Overall, it seems like the experimental XEDS quantification estimates an increasing amount of Au atoms as the nanoparticle increases in size, which is attributed to measurement error. Keeping the Au stable throughout the simulated series is therefore scientifically sound. Another input was of course the experimentally determined nanowire radius, since it, as discussed previously, determines the amount of atoms needed to complete a full layer. Other parameters include an evaporation factor and net impingement of the atomic species (as will be discussed later), and surface energies. The surface energies used were based on theoretically determined surface energies, but fitted based on the results of the simulation, while the evaporation factor was assumed to be the same as for the GaAs growth in the original version of the model.[58]

6.2.2 Step-flow and incubation results from the simulation

In general, the simulation successfully reproduced many of the trends observed experimentally with regards to the step-flow and incubation behavior with changing V/III ratio, as shown in Figure 6.4.

If we again start with the incubation, Figure 6.4 (a), we can see that the incubation time in general is around 10 s, while increasing for low V/III, as expected from the experiments. However, for high V/III ratios, the incubation time seems to decrease rather than increase, as observed experimentally. Since the model does not include any radial overgrowth of nanowires, this strengthens our previous hypothesis that the radial overgrowth acts as a material sink in the experiments, increasing the incubation time drastically. Regarding the step-flow times, as shown in Figure 6.4 (b), the trend with increasing step-flow time for intermediate V/III ratio, at the border between the two regimes, is correctly reproduced by the model. The difference here is that the step-flow time increases more in the model, to

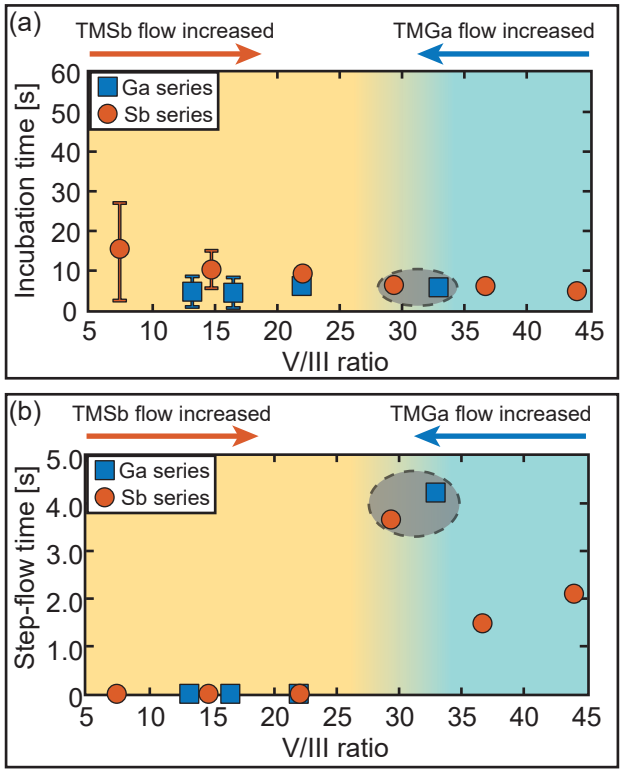

Figure 6.4: The incubation (a) and step-flow (b) data retrieved from the GaSb simulation, displayed as a function of the experimental V/III ratios. Both of the graphs are color coded based on the stable (cyan) and dynamic (yellow) regimes observed experimentally. The gray ovals in both graphs indicate, again, where the growth conditions for the two experimental series should overlap based on flows, with a slight discrepancy in V/III ratio based on growth chamber geometry in the two experimental datasets.

about 5 s instead of 2 s as observed experimentally. However, as the trend is the same, more effort was not put into further optimizing the increase in step-flow time. For higher V/III ratios, the step-flow decreases in a similar way as shown experimentally. The important aspect, and most interesting, is the emergence of a region of instant step-flow for lower V/III ratios, just as the experimental observations indicated.

The overall investigation of the step-flow and incubation times confirmed many of the observations made during the experimental growth of GaSb. However, in order to explain specific aspects shown, a more detailed analysis is required. For this, the simulation is capable of providing a detailed breakdown of many aspects of the growth, as will be shown in the next section.

6.2.3 Comparison between different simulation results

In Figure 6.5, number of atoms and supersaturation are shown for a subset of four different simulations, corresponding to V/III ratios spanning the full investigated range in the TMSb series. We will start by discussing the number of atoms in Figure 6.5 (a), where the simulation corresponds to a V/III ratio of 44.03, i.e. far into the stable regime. It can be seen that the number of atoms forms a sort of sawtooth shape, that is flat between the peaks. The rise of the sawtooth indicates a build-up of material in the nanoparticle, corresponding to the incubation period. Once sufficient supersaturation is reached, as shown in Figure 6.5 (b), nucleation (onset of step-flow) will occur, leading to a sharp decrease in both supersaturation and number of atoms. Importantly, the decrease stops abruptly and the curve continues in a horizontal manner. Here, the nanoparticle is depleted of growth material, and therefore relies on mass flow from the vapor in order to facilitate the growth. This fits with the previously presented theory that the amount of material in the nanoparticle is not sufficient to facilitate instant step-flow in the stable regime, as shown in Figure 6.3.

In Figure 6.5 (c), which corresponds to a V/III ratio of 29.35 at the border between the two regimes, we see a similar shape for the number of atoms, where the "flat" regions of the curves are longer. This can be explained by the fact that the influx of Sb is lower in this lower V/III ratio case. When the nanoparticle becomes depleted and starts to rely on delivery of Sb from the vapor phase, the arrival rate of Sb is in this case lower and the step completes at a lower rate, increasing the step-flow time. The overall result is that the growth in Figure 6.5 (a) proceeds with a higher nucleation rate than the growth presented in Figure 6.5 (c), resulting in the lowering of incubation time with increasing V/III ratio in the stable regime, as shown in Figure 6.4 (a). Notably, the growth in both cases is very regular, as was also observed experimentally for the intermediate V/III ratio case, where both incubation and step-flow in Figure 6.1 show small standard deviations for a V/III of 29.

By further decreasing the V/III ratio into the dynamic regime (22.03), the number of atoms show the behavior as presented in Figure 6.5 (e). Here, the sawtooth shape persists, but lacks the flat regions in between. This means that there now is enough dissolved material in the slightly larger nanoparticle to facilitate complete layer growth, once nucleation has occurred, resulting in instant step-flow. Still, the growth is very regular as seen in the supersaturation plot in Figure 6.5 (f).

In all the cases discussed until now, the nucleation event results in a significant decrease in number of atoms, and therefore supersaturation, in the nanoparticle. This results in a nanowire growth process that becomes clearly periodic, as indicated by the sawtooth shapes discussed previously, where the build-up of material during incubation determines the time of the next nucleation event. The resulting variation in incubation and step-flow time, as indicated by the error bars in Figure 6.4 (a) and (b), is therefore small. By further decreasing the V/III ratio to 7.35, however, the simulation produces the results presented in Figure

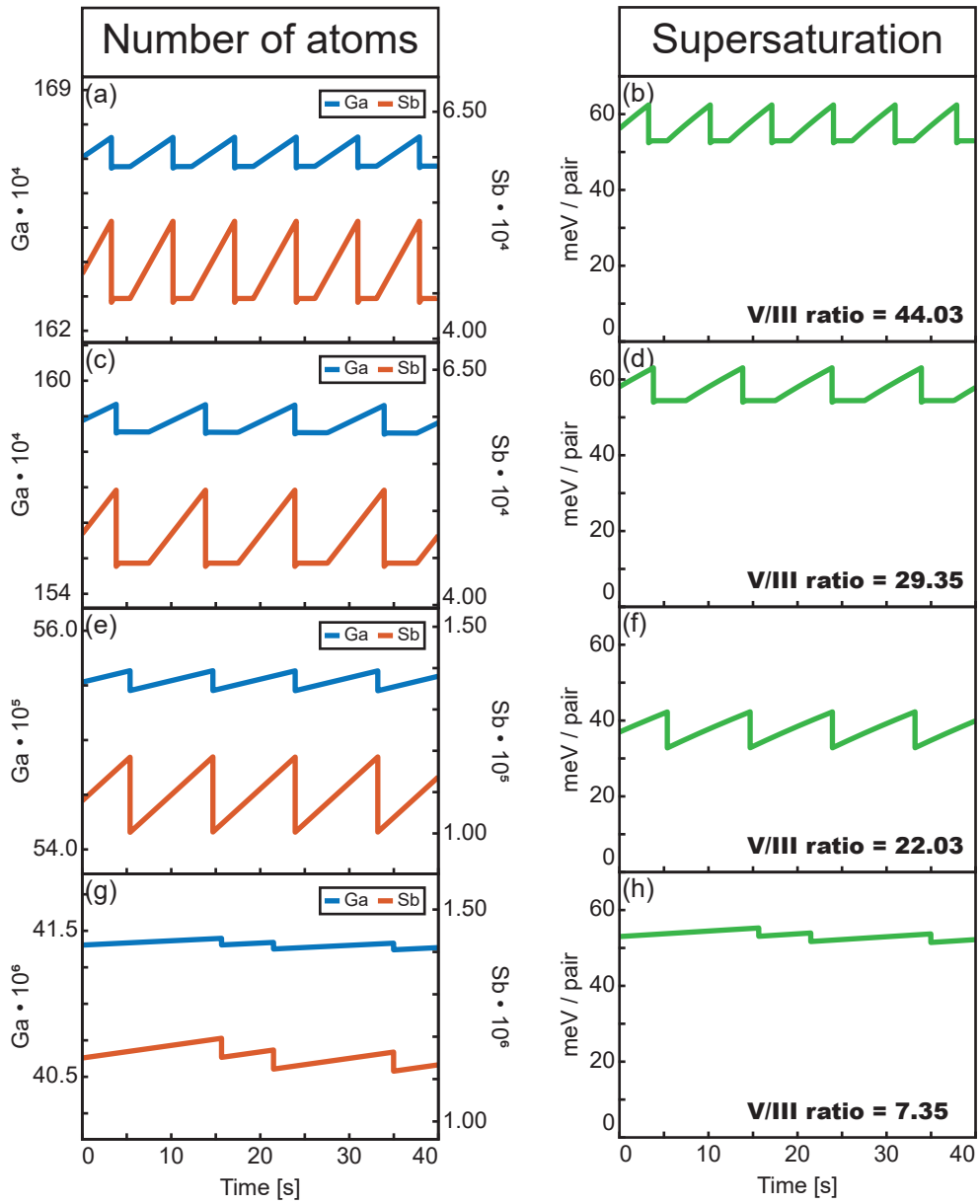

Figure 6.5: Further data extracted from four of the GaSb simulations. The graphs show how the number of atoms for Ga and Sb and the supersaturation changes over time for a subset of the simulations (full length is 300 s). The cases are from the TMSb flow series, spanning V/III ratios of 44.03 (a)-(b), 29.35 (c)-(d), 22.03 (e)-(f) and 7.35 (g)-(h).

6.5 (g) and (h), where the growth becomes irregular. The periodic sawtooth shape is here lost, in favor for a more erratic behavior. Notably, the change in supersaturation during step-flow is very small, since the absolute change in number of atoms of either Sb and

Ga is very small for this much larger nanoparticle. The smaller change in supersaturation upon nucleation can lead to several nucleations occurring in close succession, with short incubation, since the nucleation probability will still be high. However, there is a trade-off in the fact that the build-up of supersaturation will be very slow, since adding Sb to the large nanoparticle does not change the composition much, and the flow of Sb is overall lower in this case due to the low V/III ratio. The erratic growth behavior results in a large spread in incubation data, as shown by the error bar for V/III ratio of 7.35 in Figure 6.4 (a), which corresponds well to the experimental results from the same growth shown in 6.1 (a). This demonstrates that the Monte Carlo aspect of the growth model accurately simulates the non-deterministic nature of nanowire growth.

6.2.4 Comparing the growth behaviors of GaSb and GaAs

Since the original version of the simulation was made to simulate GaAs growth,[58] it is natural to compare the results from the two systems. The most notable differences between the growth of GaAs and GaSb stem from the big difference between the two group V elements. Sb has a much lower vapor pressure and higher solubility in the Au-Ga liquid alloy than As, which leads to it accumulating to a few atomic percent during the growth. Arsenic, as mentioned earlier, is expected to remain below 1 at.% (more often < 0.1 at.%) in the liquid phase. This makes As very quickly reach a stable composition within the droplet during incubation, and therefore Ga is found to largely limit the nucleation process. The amount of dissolved As is also never enough to facilitate instant step-flow for GaAs in the parameter space explored, so the nanoparticle always has to rely on the mass flow of As to complete the layer. However, the growth of GaAs is usually operated at very high V/III ratios where the surrounding vapor is abundant of available As, leading to a step-flow that is fast, in general.

Another difference between the two systems is the amount of dissolved Ga observed during growth, where the amount is typically much less for GaAs. For GaAs, the amount of dissolved Ga observed was between 25 and 55 at.%,[58] while in the GaSb case the Ga was never less than about 70 at.%. Therefore, a big difference both in the experimental results and the simulation is the volume of the droplet and the resulting radius of the nanowire, which are more dynamic in the growth parameter range investigated in the GaSb case. However, some swelling is also observed towards the low end of V/III ratios investigated in the GaAs case, associated with an increase in both step-flow and incubation time.

6.2.5 A discussion on atomistic pathways

In the simulation, one of the main inputs is the precursor partial pressure. This value was used in order to emulate the supply of growth material to the nanoparticle. Importantly, no

aspects of the precursor pyrolysis or material delivery in the vapor phase is considered, so the value is scaled by a factor from the experimentally determined partial pressures, so as to decrease the magnitude of condensation. While simulating the different experiments, it was discovered that the best results were found when the TMSb supply was made to follow the experimentally determined partial pressures (scaled by a factor), while the TMGa supply was tailored so as to match the resulting material delivery of Sb. The following text aims to explain this necessary simplification.

The material supply from the vapor will here be referred to as condensation. The condensation scales with temperature and several other factors, but most importantly for this discussion, the supplied partial pressure and the surface area of the nanoparticle. Once material has condensed into the nanoparticle, there are two separate paths of removal. For one, there is evaporation from the nanoparticle back to the vapor phase, which scales in the same way as the condensation and is calculated based on several thermodynamic parameters. The evaporation was in all cases found to be low for Ga and Sb, leading to a very small magnitude of this removal path. This leaves the other removal path, solidification to the nanowire, which will depend on the growth rate of the nanowire and of course the area of the nanowire-nanoparticle interface, which is the same as the cross-sectional area of the nanowire. The solidification therefore scales with the radius of the nanowire, but is also complex to describe since both Sb and Ga are involved in the growth rate of the nanowire. All of these paths and important factors are presented in Figure 6.6, for the case of a high V/III ratio (a) and a low V/III ratio (b).

The high V/III ratio case will be discussed firstly, in the context of the results from the TMSb series, where the largest range of V/III ratios were used. By adjusting the partial pressures of both Ga and Sb (as well as several other fitting parameters), conditions can be found where the volume, incubation and step-flow all correspond well to the experimental conditions intended to be reproduced. In this case, since evaporation is negligible, stability in the system is achieved when the supply of Ga and Sb are equal, since the only path of removal is through solidification, where a stoichiometric compound of equal amounts of Ga and Sb is formed. Material should also be solidified at a comparable rate to the experiments, with appropriate step-flow and incubation times. Once such conditions are found, the ideal case would be to change the surrounding experimental parameters and conditions to simulate the low V/III case, and the results should be equally well matched to the low V/III experiment. This means that the radius of the nanowire and the size of the nanoparticle should increase, while the Ga partial pressure should remain constant and the Sb partial pressure should decrease (when considering the TMSb series).

Adjusting the size of the system has several effects. By increasing the size of the nanowire, we make sure that the solidification pathway increases, increasing material consumption. Simultaneously, the nanoparticle surface area is increased, so condensation increases. Similarly, the Sb supply is lowered, so growth rate will decrease (we have already seen that

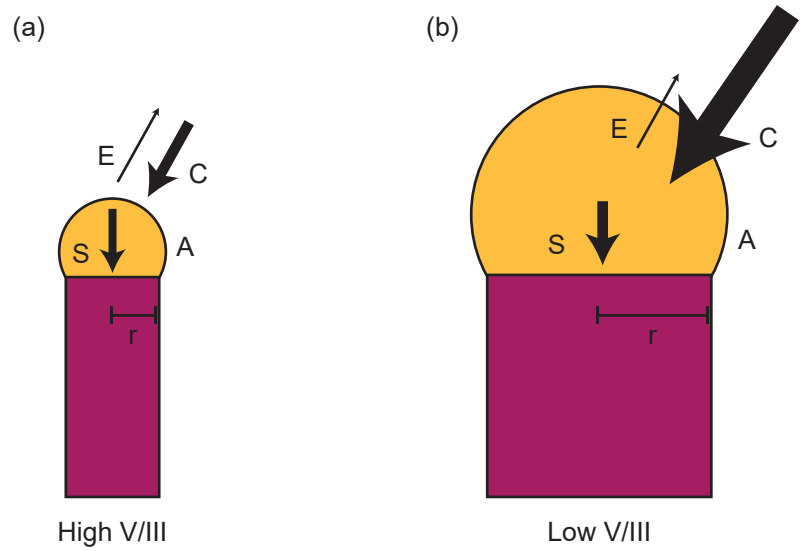

Figure 6.6: A schematic detailing atomistic pathways in the model. (a) A high V/III ratio case. (b) A low V/III ratio case. In the figure, E stands for evaporation, C for condensation, S for solidification, A for the surface area of the nanoparticle and r indicates the nanowire radius.

incubation is significantly longer for the low V/III case). Overall, this results in a great increase in total Ga delivery, while the delivery of Sb is low, and total material consumption is low. When Ga is significantly higher than Sb, the nanoparticle will swell at each timestep of the simulation, which further increases the nanoparticle area, increasing the condensation of Ga and so on.

Evidently, there is a stabilization mechanism missing in the simulation, that could handle such a situation described above. Importantly, we know that the conditions used as input for the simulation are experimentally determined steady-state conditions, so stability should be achievable. One suggestion for improvement is that there is something missing from the expression of evaporation. However, it is expected that evaporation should affect Sb to a greater extent than Ga, which would only worsen the problem presented above (Sb would evaporate more from the low V/III case with the larger nanoparticle surface area). Therefore, it is more likely that something is missing regarding the supply or removal of Ga to the nanowire. A possibility is that Ga is leaving the nanoparticle through an out-diffusion mechanism, giving a path for removal of Ga that scales with the radius of the nanowire.[133] However, when this was implemented, it appeared to affect the smaller nanowires to a greater magnitude, leading again to the opposite effect. Another possibility is the assumption that diffusion, rather than direct impingement, controls the arrival of Ga atoms to the nanoparticle. This has been explored by Mårtensson et. al., where it was found that the material delivery scales with the radius of the nanowire and that smaller

nanowires therefore experience a higher effective V/III ratio if the group V material is delivered through direct impingement.[57] The implementation of such a diffusion dependent Ga delivery could therefore be a way to improve the simulation.

The conclusion of this discussion is that it is expected that the arrival of Ga atoms to the nanoparticle is overestimated in the current implementation of the simulation, and that this parameter scales especially poorly with size of the system. The simplest solution to this problem was therefore to manually scale the Ga supply on a case by case basis, which resulted in a need to increase the Ga supply in the TMSb series as the "V/III ratio" was increased. In the TMGa series however, the best results were found when TMGa, similarly to TMSb, was not changed at all between the different experimental conditions. This is interesting, as this suggests that roughly the same impingement of material per unit area can result in steady-state growth for a wide range of nanoparticle and nanowire sizes. This might give a clue for the scaling of the Ga delivery, when future iterations of the model are constructed.

6.3 The impact of defects in GaAs nanowire layer dynamics

Crystallographically speaking, GaSb is a rather simple system. Compared to phosphides and arsenides, that can grow in both the ZB and the WZ crystal structures, there is a lack of reports of GaSb growing in the WZ crystal structure.[62] Even forming crystallographic defects or twins seems to be difficult in the GaSb material system. So what happens to the layer growth dynamics when growing nanowires in growth regimes resulting in imperfect crystal structures? That will be the topic of this section and **Paper v**, where the growth of twinned GaAs was studied.

6.3.1 *In-situ* investigation of twin formation

Twins were introduced in Chapter 2 as rotations in the crystal around the $[\bar{1}\bar{1}\bar{1}]$ axis, where the stacking sequence in ZB appears to reverse. In some instances twins are sought after, for example when forming twinned superlattices, but oftentimes they are avoided as they affect the properties of the crystal.[134,135] In our case, GaAs was purposefully grown using growth conditions where twinning occurs, so that the growth dynamics during twinning could be studied and compared to the growth dynamics of regular GaAs layers, grown under the same conditions. As a general procedure, many regular, non-twinned, layers were measured in terms of incubation and step-flow, for the same nanowire under the same conditions, so that the times could be compared to those of the twinned layers formed in the structure. This procedure was repeated for nanowires of different diameters, over a range of

experimental conditions.* A general example of a measured nanowire, the twinning process and the resulting step-flow and incubation times is shown in Figure 6.7 (a) and (b).

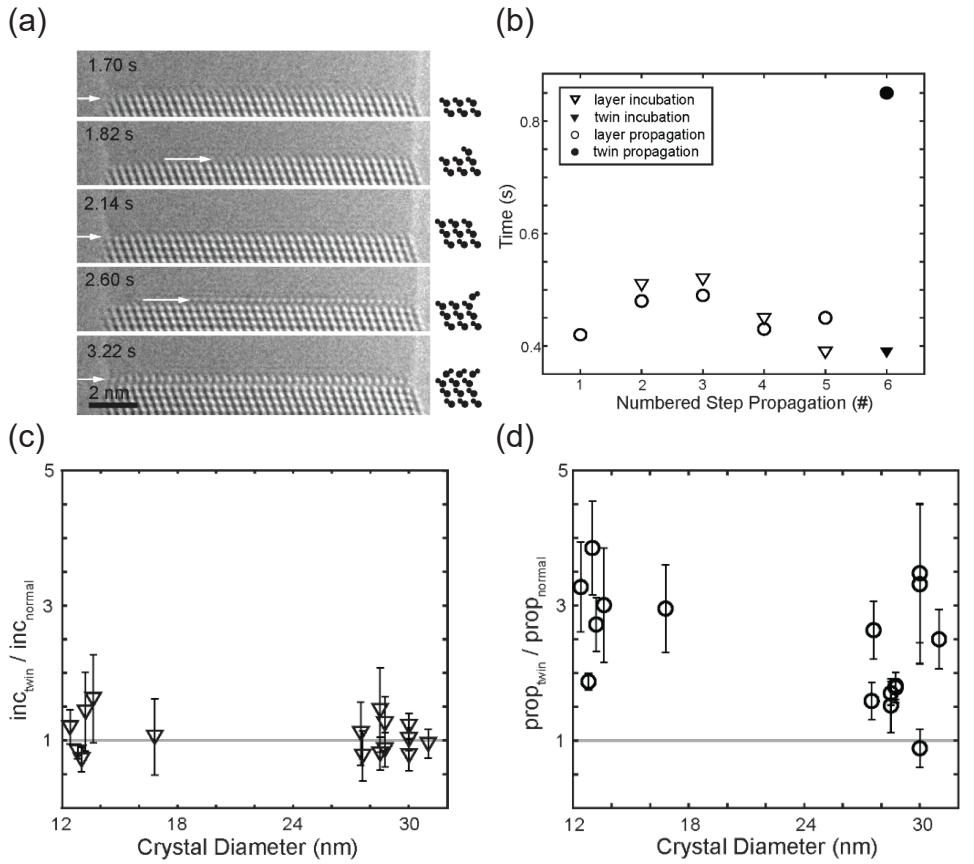

Figure 6.7: Twin formation dynamics in Au-seeded GaAs. (a) A twin formation event across five frames, further illustrated by the schematic. The arrows are pointing to the growth fronts of the layers, where the twinned layer nucleates in the fourth frame. The time stamps are correlated to the time in the movie supplied as Movie S1 in the original publication. (b) The incubation and step-flow (propagation) times of the layers preceding, and including, the twinned layer. (c) A collection of incubation times of twinned layers, that are related to the incubation time of non-twinned layers by a ratio. The gray line indicates when the ratio is equal to 1, where the incubation therefore is equal in time in the two cases. (d) A similar ratio as (c), but for step-flow time (propagation time) instead. The gray line indicates when the ratio is equal to 1. Figure adapted from **Paper v**.

As can be seen in Figure 6.7 (a), the emergence of a twinned layer can be easily observed when the nanowire is imaged in the $[1\bar{1}0]$ viewing direction. Figure 6.7 (b) shows how the incubation and step-flow time varies for the five measured layers (empty shapes) leading up to the twinned layer (filled shapes). Evidently, the incubation time appears to be largely unchanged across the entire sequence, while the step-flow time for the twinned layer has increased compared to those of the non-twinned layers. In Figure 6.7 (c), the ratio between

*Naturally, the growth conditions have to be adjusted in order to achieve sufficiently twinned structures when the nanowire diameter is changed.

the incubation time of twinned layers and the averaged incubation time of several preceding non-twinned layers is plotted as a function of nanowire diameter. As can be seen, for this larger dataset, the previously observed stability of the incubation time is present here as well, and in general incubation is as long for twinned as non-twinned layers (the ratio equals to 1). This indicates that the actual nucleation energy barrier for forming a twinned layer is similar to the non-twinned case. Figure 6.7 (d), however, shows the same investigation of the step-flow times. Here it can clearly be seen that the step-flow time increases for twinned layers, as compared to non-twinned layers. This would indicate that there is a thermodynamic barrier for further additions to the growing twinned nucleus, that is larger than that of non-twinned layers. Both Figure 6.7 (c) and (d) illustrate that there is no strong trend with nanowire diameter.

6.3.2 Thermodynamic modeling of the twin formation

In order to qualitatively compare the growth of normal and twinned layers, a thermodynamic model was constructed. The idea behind the model was to treat the twin formation as normal ZB with added energy terms based on the interfaces it forms to the rest of the phases, and evaluate the difference in formation energy, ΔG_j (where $_j$ is either regular or twinned layers), for different supersaturations, $\Delta\mu_{ZB}$. The equation used for the model is shown in Equation 6.1.

$$\Delta G_j = \Delta\mu_{ZB}\, N + \sigma_{iL,j}\, l_{iL} + (\sigma_{iV} - \sigma_{LV}\, \sin(\beta)) l_{iV} + \Delta\gamma_j A \tag{6.1}$$

In Equation 6.1, the first term is the supersaturation multiplied by the number of atoms added to the growing layer, N. The second term is related to the edge energy $\sigma_{iL,j}$ of the island, $_i$, facet interfacing the liquid phase, $_L$, with length l_{iL}. The edge energy is assumed to be slightly different for the twinned and non-twinned cases. Similarly, the third term is related to the interface between the island and the vapor, $_V$, where the length, l_{iV}, is multiplied with a positive energy term, σ_{iV}, for the formation of the interface and a negative energy term $-\sigma_{LV}\sin(\beta)$ for the removal of the previously existing liquid-vapor interface. The last term is only needed for the twinned case, where a surface energy, $\Delta\gamma_j$, between the twinned layer and the underlying ZB is multiplied by the area of the island, A. By evaluating the formation energy for the twinned and non-twinned cases for different supersaturations, Figure 6.8 was constructed.

The results show that for higher supersaturation (55 meV), the difference between the twinned and non-twinned case is small. Two main differences arise: the critical nucleus size is larger for the twinned case (making nucleation of twins less probable) and the energy gain by continued addition after the critical nucleus is reached is smaller for the twinned case (less steep slope). Both of these differences make sense from the experimental observa-

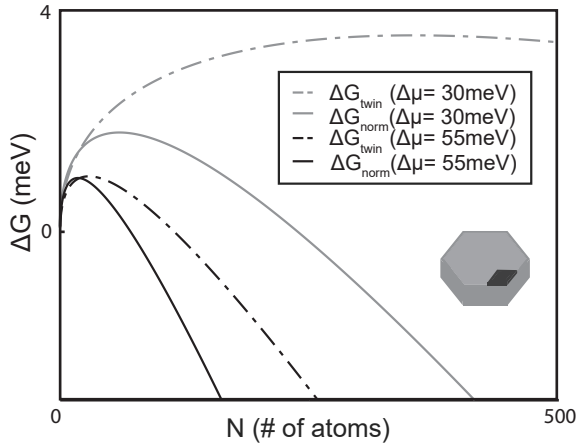

Figure 6.8: A model illustrating the nucleation of twinned and non-twinned layers of GaAs. The change in Gibbs free energy is plotted as a function of number of atoms for different supersaturations. The inset illustrates the assumed shape of the nucleus on the top facet. Figure adapted from **Paper v**.

tions, since fewer twinned layers form than non-twinned, and the step-flow of the twinned layers is slower. However, the difference in appearance is not so great when only considering the 55 meV case in Figure 6.8. At this point it is important to consider the nature of the nanowire growth cycle: as we saw for the layer-by-layer growth of GaSb earlier in this chapter, the supersaturation changes throughout the step-flow process. Consider for example the supersaturation plots in Figure 6.5; we see that the supersaturation can drop by approximately 10 meV during the step-flow for GaSb, which means that GaAs could behave in a similar way. It has been theorized in earlier studies that ZB growth in GaAs is favorable for supersaturations between roughly 30 and 55 meV, which is why we have plotted the two extremes of this range in Figure 6.8.[48] The 30 meV case in Figure 6.8 has a very different appearance than the 55 meV case, and displays much larger differences between the twinned and the non-twinned case. If a twin layer therefore nucleates when the supersaturation is 55 meV, which, again, is likely, since the difference between twinned and non-twinned here is small, the nucleus might reach critical size and become stable even if the supersaturation decreases throughout this process. With the decreasing supersaturation, however, the shape of the curve will gradually change to be more similar to the 30 meV case, and therefore lead to a slower step-flow than predicted by the 55 meV curve.

6.3.3 Multilayer growth in GaAs nanowires

An interesting finding that was made throughout this study was the emergence of multiple nucleation events within a single step-flow time, meaning that two or more layers could be growing simultaneously. This sometimes occurred in conjunction with the formation of

twins, as can be seen in Figure 6.9.

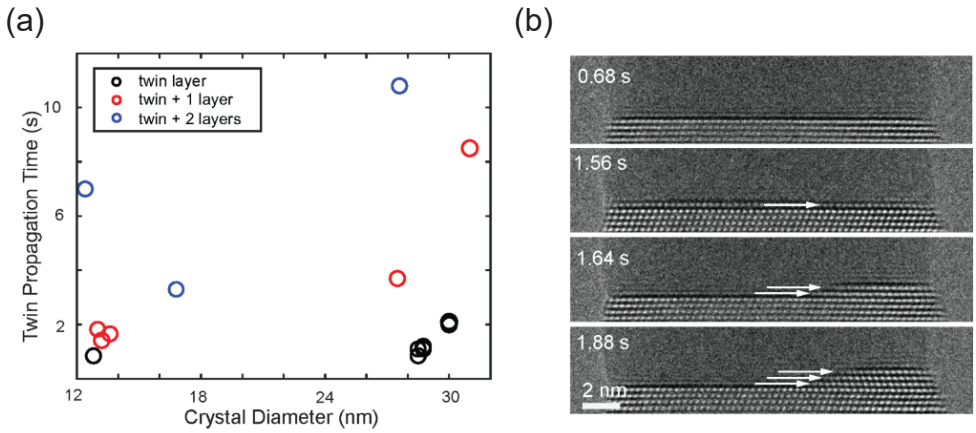

Figure 6.9: Multiple nucleation events observed in conjunction with the formation of twins in GaAs. (a) A collection of several observations where one or two layers nucleate before the twinned layer is completed, for various investigated nanowire diameters. (b) One such example, where the arrows point to the growth fronts of the individual layers and the time stamp is related to Movie S3 in the original publication. Figure adapted from **Paper v**.

The emergence of this multilayer growth is unexpected, since nanowire growth has always been predicted theoretically, and shown experimentally, to occur in a layer-by-layer growth mode. [58,136] An explanation can be gotten from the supersaturation discussion from earlier: if a twin nucleates for high supersaturation and the supersaturation then decreases, the step-flow might become so slow that the nanoparticle can start building up material during the step-flow, increasing its supersaturation again. If the supersaturation then increases sufficiently this might make the nucleation of a non-twinned new layer a competing process. This process however likely has a low probability, as it is so seldom observed.

6.4 Multilayer growth in InGaAs nanowires

The observation of multilayer growth introduced lastly in the previous section was a surprise, and interesting from a growth dynamics perspective. However the technological implications of multilayer growth in pure GaAs are small, since the crystal in the end still is pure GaAs and multilayer growth seems to only occur in conjunction with twins. If, on the other hand, a ternary nanowire or a nanowire heterostructure is to be grown, the emergence of multilayer growth can possibly affect the composition within the nanowire. As it turns out, multilayer growth can occur for InGaAs nanowires as well, and the observation and discussion of multilayer growth in InGaAs is the topic of **Paper vi** and the rest of this chapter.

6.4.1 Different occurrences of multilayer growth

As was presented in the previous section, multilayer growth can occur in the presence of crystallographic twins in GaAs. Figure 6.10 (b) shows a case where this is also true for InGaAs. In this case, the amount of In in the solid nanowire is quite low, only about 10 at.% giving roughly a composition of $In_{0.2}Ga_{0.8}As$.

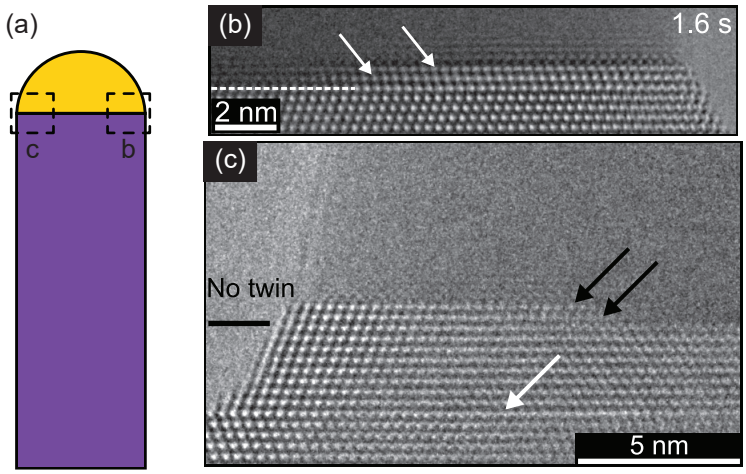

Figure 6.10: Multilayer formation in Au-seeded InGaAs nanowires. (a) A schematic illustration where the dashed boxes illustrate the respective regions that are displayed in (b) and (c). (b) An example of multilayer nucleation in conjunction with the formation of a twin. (c) A case where multilayer growth occurs without the presence of a twin. A twin further down the nanowire is pointed out in (c), while the rest of the arrows point to the growth fronts of the individual layers. Figure adapted from **Paper VI**.

In the case presented in Figure 6.10 (b), the argumentation for the emergence of multilayer growth can be the same as for the pure GaAs case, namely that the twin leads to a slower growth which can promote further nucleation. However, multilayer growth has also been observed when there is no twin present, as is shown in Figure 6.10 (c). Since multilayer growth therefore can occur without the presence of twins, there has to be another factor affecting the energy balance. A possibility is the compositional distribution within the nanowire and the compositional relationship between the nanoparticle and nanowire. It has been suggested, for example, that nucleation for InGaAs occurs through an In rich initial nucleus.[131] However, the consumption of either of the two group III elements will naturally affect the supersaturation of the other, and small changes are expected to have large effects on the growth.

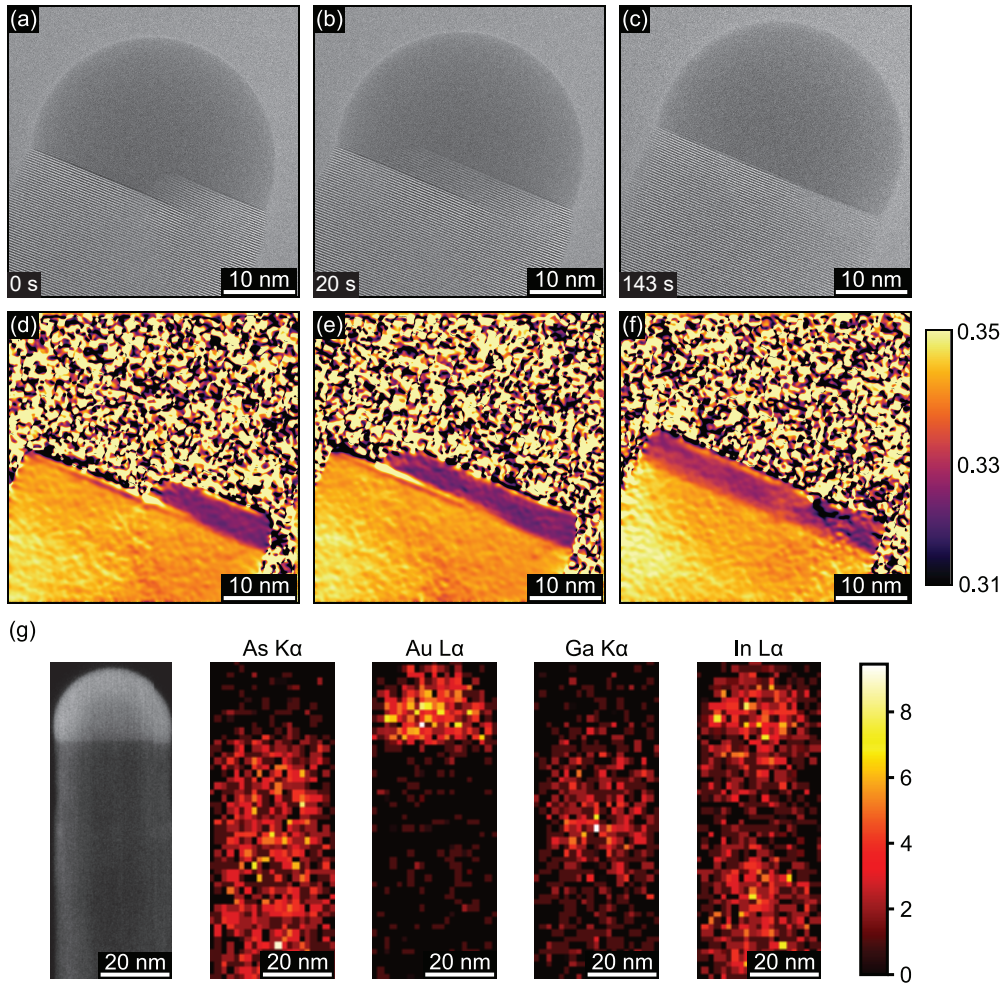

Figure 6.11: Multilayer growth at a sharper compositional heterostructure, as a consequence of altered growth conditions. (a)-(c) The evolution of the multilayer over time, where the timestamp in the bottom left corners indicate the time in seconds from the frame presented in (a). (d)-(f) The same frames as in (a)-(c) after GPA treatment. The color scale is chosen so as to represent more In rich as orange and more Ga rich as purple. (g) The STEM XEDS results, confirming that the nanowire segment grown in the multilayer growth mode is more Ga rich than the rest of the nanowire. Figure adapted from **Paper VI**.

By introducing a sharp switch in the surrounding conditions, we have observed that multilayer growth can in some instances be induced. In this case, the surrounding conditions were changed to be more In rich, which sparked the rapid formation of a more Ga rich multilayer segment, as can be seen in Figure 6.11, where the micrographs show the process and the GPA treatment qualitatively indicates the composition based on the lattice parameter variation. It might seem backwards that an increase in In flow could lead to the formation of a more Ga rich segment, but the supersaturation behavior shown in Figure

5.4 (c) can help clarify this. In this experiment, it was observed that the supersaturation of GaAs, which always is higher than InAs, increases with increasing concentration of In, even if the concentration of Ga simultaneously decreases. If more In is suddenly available for the nanoparticle, we therefore expect this process to occur more rapidly, resulting in a quick increase in GaAs supersaturation and the nucleation of a more GaAs rich nanowire segment. What this means is that the initial formation of the multilayer stack is rapid, but we also see from the timestamps in Figure 6.11 (a)-(c) that its completion is very slow. At this point we must remember that even though we have shown that we can grow most solid compositions of InGaAs in Chapter 5, there is still a thermodynamically derived miscibility gap in bulk InGaAs, meaning that the binaries prefer to segregate. This can be the explanation for the multilayer segment continuing to grow as GaAs rich instead of incorporating more InAs in the left half of the stack, as can be seen in Figure 6.11 (c) and (f). We also confirmed the compositional changes by performing STEM XEDS on the segment after growth interruption, as can be seen in Figure 6.11 (g). The quantification shows that the nanowire composition changed from $In_{0.8}Ga_{0.2}As$ to $In_{0.3}Ga_{0.7}As$ in the multilayer segment.

6.4.2 Dynamic behavior of multilayer growth in InGaAs nanowires

What we have observed about multilayer growth in InGaAs, is that the number of layers involved can be much larger than for pure GaAs, and that the number of layers can change back and forth throughout a multilayer growth event. This is illustrated in Figure 6.12, where a multilayer growth event is followed from start to finish by means of three separate videos recorded in sequence with short interruptions in between. In this case, the composition of the nanowire is around $In_{0.6}Ga_{0.4}As$.

We start by discussing the results from Video 1, corresponding to Figure 6.12 (a)-(c). Figure 6.12 (a) shows a frame from the video where a single layer is growing, and a magnified version is found in Figure 6.12 (b). Figure 6.12 (c) details the growth throughout the entire video, where the growth times of individual layers, marked by their start and end times, are plotted. Alongside is also plotted a cyan bar chart, detailing how many layers are growing simultaneously. As can be seen, after about 45 s, layers start to overlap and the beginning of the next layer occurs before the end of the previous one. The behavior here is already very different from the twinned GaAs case, where an extra layer could only form after a twinned layer was grown. Here, for many layers in a row, nucleation occurs before step-flow is complete. Since it is highly unlikely that every layer is twinned with respect to the previous, we therefore expect that the composition in the nanowire layers is affecting the thermodynamic balance, leading to the multilayer growth behavior shown here.

Looking instead at the results from Video 2, we see that the stack of multilayers in many cases increases to larger than two simultaneously growing layers, but also occasionally de-

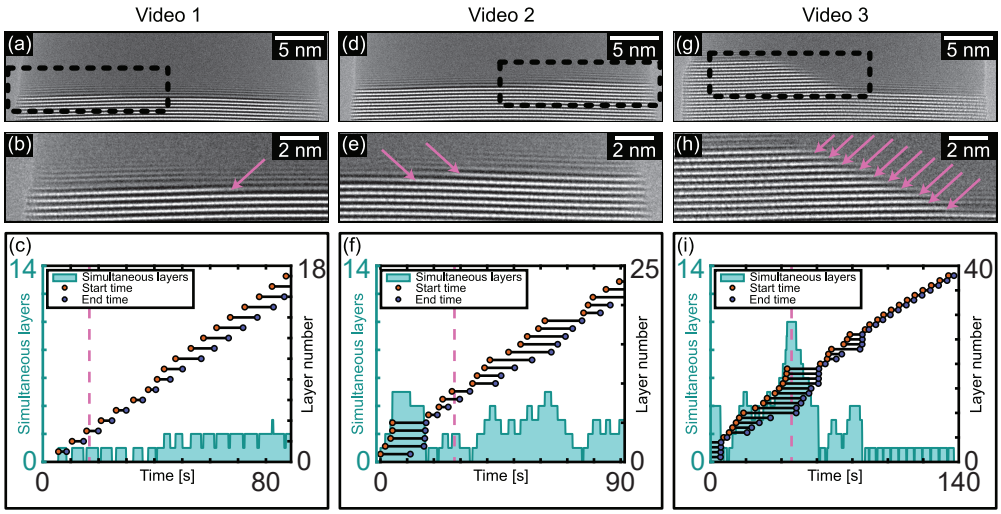

Figure 6.12: A detailed description of a long, dynamic, multilayer growth event, split across three recorded videos, arranged into columns. (a), (d) and (g) show frames extracted from respective video, where the dashed boxes indicate the region of the magnified versions shown in (b), (e) and (h), respectively. Growth fronts of individual layers are marked by pink arrows. (c), (f) and (i) show start and end times of all layers observed growing in the respective videos, along with total number of concurrently growing layers, as a function of time. The dashed pink lines indicate the time in the videos from where the frames are extracted. The videos in question (in a shortened format) can be found in the Supplementary Information of the original publication. Figure adapted from **Paper VI**.

creases back to one (or even zero growing layers). In Video 3, the largest stack of multilayers observed in the entire segment is shown in Figure 6.12 (g) and (h), where ten layers are growing simultaneously. Towards the end of this video the nanowire returns to regular layer-by-layer growth again.

The constantly changing size of the multilayer stack throughout the entire growth event presented in Figure 6.12 highlights the dynamic nature and complexity of multilayer growth. However, it is not only the size of the multilayer stack that changes throughout the multilayer growth process; the individual layers are also dynamic, and grow and shrink throughout the growth. The determined processes are presented in Figure 6.13, which shows frames extracted from Video 2 introduced in Figure 6.12.

Process (1) illustrated in Figure 6.13 (a) is the simplest of the observed processes. Here, the growth front of all layers in the multilayer stack move forward. Obviously, there is a competition for material between the layers, which means that the individual growth fronts move forward at a slower rate than what they would if they were growing alone. Importantly, the expansion of upper layers is limited by the expansion of the lower ones, producing a sort of staircase-like growth front of the entire stack. This can be seen in the micrographs presented in Figure 6.13 (b) and (c), where the Process (1) is illustrated. However, it is also important to mention that there does not seem to be a strong preference for a specific facet formed by the growth fronts, and the angle the steps form can change

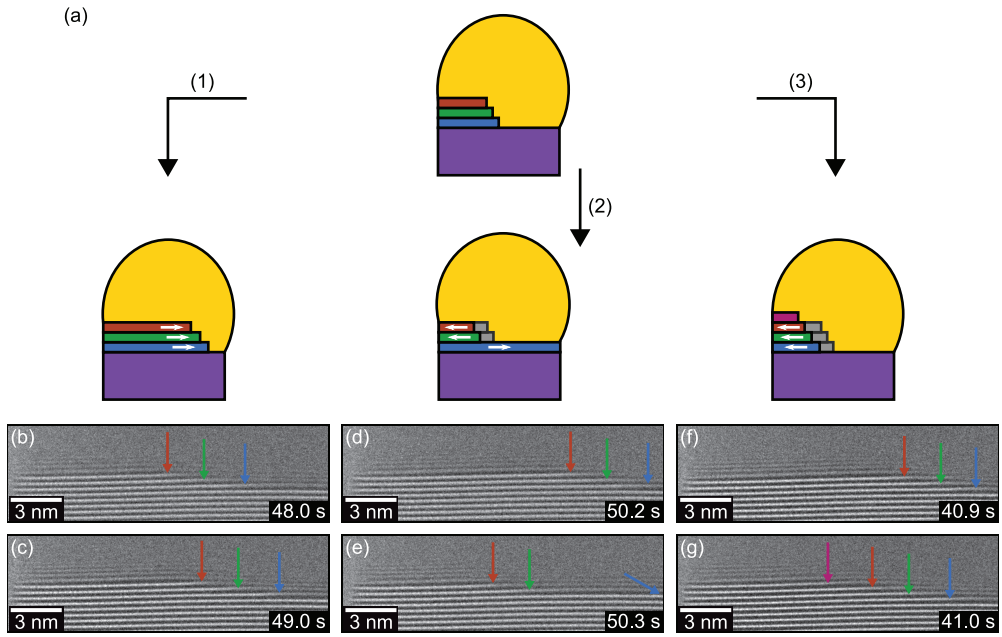

Figure 6.13: (a) Three processes observed to occur for multilayer stacks. (b)-(c) Process (1), where all involved layers grow simultaneously. (d)-(e) Process (2) where the bottom most layer rapidly finishes. (f)-(g) Process (3) where a new layer nucleates on the stack. The timestamps indicate the time from the start of the video from which these frames were extracted, and illustrate the relative rates of the processes. The arrows point to the growth fronts of the individual layers, when possible. Figure adapted from **Paper VI**.

with relation to the horizontal plane.

Process (2) and (3) highlight more dynamic cases of the multilayer propagation, where the interaction between the layers becomes important. In Process (2), as shown in Figure 6.13 (a), the bottommost layer of the multilayer stack rapidly grows to completion. This process is shown in the micrographs in Figure 6.13 (d) and (e), where the layer completion occurs within the temporal resolution used for the recording (10 FPS). As is illustrated by the colored arrows in Figure 6.13 (d) and (e), the rapid completion of the layer leads to a retraction of the other layers in the multilayer stack (the corresponding arrows move to the left between Figure 6.13 (d) and (e)). Similarly, Process (3) illustrates the nucleation of a new layer on the multilayer stack, which also results in a retraction of the other layers in the stack, as shown schematically in Figure 6.13 (a) and through micrographs in Figure 6.13 (f) and (g).

Both process (2) and (3) illustrate an important point: already solidified material can be redissolved from classically viewed stable layers as a consequence of the interaction between individual layers in multilayer stacks. This means that the compositional relationship becomes more complicated, but also that multilayer growth can act as a way for the nanowire

to, for example, smooth out compositional changes as it grows.

Despite the dynamic nature of the multilayer growth, it was found that the overall growth rate was unchanged in this case of intermediate composition InGaAs. Each individual layer of course exists for longer, giving more opportunity to exchange material with the other layers, but the overall number of layers formed over time is similar when comparing segments grown in the multilayer and the layer-by-layer growth modes. This was not the case when multilayer growth was observed in conjunction with a distinct change in composition, as presented in Figure 6.11, which proceeded at a slow rate. In that case, however, it seemed like the transfer of material and equilibration of composition was too difficult for the nanowire to achieve, and the energetically favorable route was to await the refilling of Ga into the droplet to grow a more homogeneous segment. This is likely because the rapid formation of the large multilayer stack created a relatively stable crystallite, making the dissolution of the layers more difficult. As we will see in the next section, the formation of such a large multilayer segment can sometimes be detrimental to continued growth.

6.4.3 Multilayer growth and kinking at sharp heterostructures

Multilayer growth has been observed to occur as a step before a nanowire kinks or loses its nanoparticle, as shown in Figure 6.14 (a)-(c). This bears a large resemblance to the type of growths observed by paladugu et. al., when investigating the growth of sharp heterostructures between GaAs stems and InAs segments, where the nanoparticle is displaced and the growth continues down along the side of the nanowire.[137] Indeed, such cases have been observed *in-situ* as well, when attempting the formation of sharp GaAs-InAs heterostructures, as shown in Figure 6.14 (d).

Several attempts at forming sharp GaAs-InAs heterostructures followed the procedure outlined below. Standard GaAs stems were grown, and before changing the gaseous environment to contain TMIn, a ramp down in temperature was performed, and the TMGa supply was interrupted. At low temperatures (< 150 °C), axial growth is completely interrupted. Therefore, the gaseous composition can be changed so as to replace the TMGa with TMIn in a controlled manner, without the growth continuing. A prerequisite for this is that the AsH_3 supply is kept on, since otherwise the nanowire might etch away the solidified layers. The temperature decrease also makes the nanoparticle solid, and leads to a loss of Ga from the nanoparticle. Once the RGA showed low levels of TMGa and high levels of TMIn in the gaseous environment, the temperature was gradually increased until effects were seen on the nanowire. Typically, this resulted in the growth of an InAs multilayer segment from the still solid nanoparticle, as shown in Figure 6.14 (e)-(g).

This investigation highlights that multilayer growth is likely something that affects the heterostructure formation in *ex-situ* growths in a similar manner, even though the low temper-

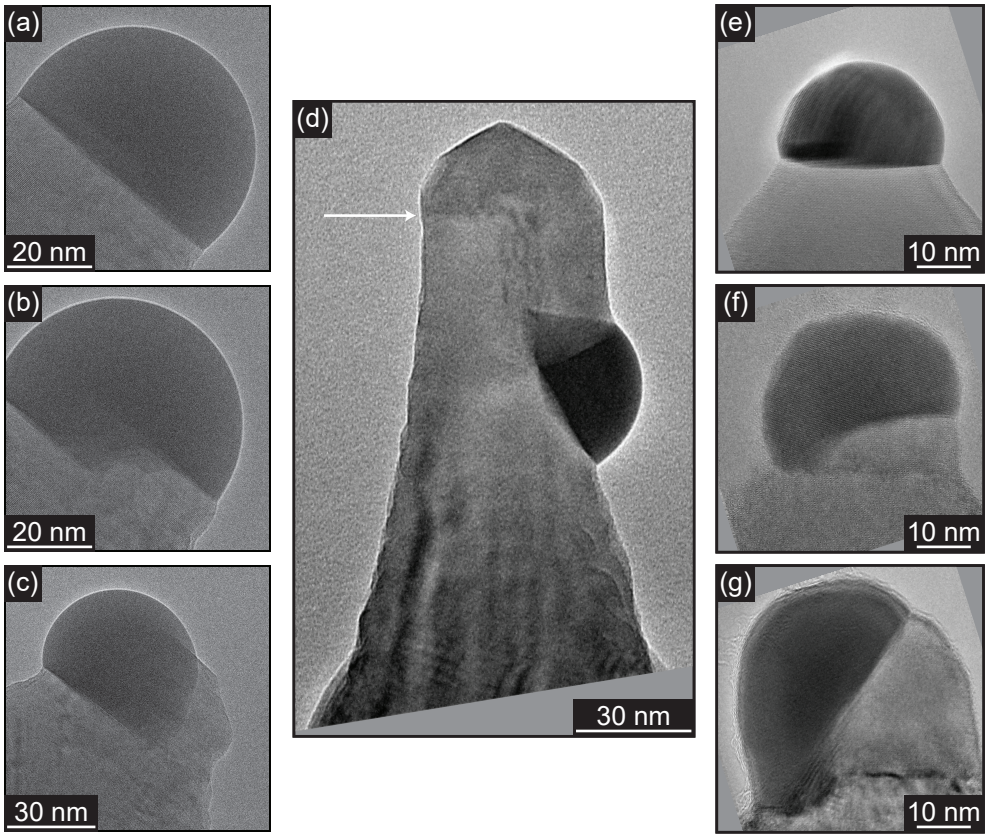

Figure 6.14: Three different cases of kinking in nanowires. (a)-(c) The process of kinking through multilayer growth, with a liquid nanoparticle. (d) A nanoparticle growing down the side of a nanowire. The arrow points to a difference in contrast, signifying that the composition changes before the nanoparticle slides off the nanowire top facet. (e)-(g) The process of kinking through multilayer growth when the nanoparticle is solid. The multilayer island consists of InAs, while the rest of the nanowire is GaAs. Panels (a)-(c) adapted from **Paper VI**.

ature procedure utilized here might be unconventional. There are a few reports on successful formation of GaAs-InAs heterostructures, utilizing either larger nominal nanoparticles in MOCVD or smaller nominal nanoparticles in MBE.[17,70] However, sufficient control of this process is lacking, and should therefore be investigated further.

Chapter 7

Conclusions and Outlook

With this thesis I hope I have been able to accurately demonstrate how and why we study the growth of semiconductor nanowires *in-situ*, using ETEM. All the studies included in this thesis work have been conducted with the goal of increased understanding of the nanowire growth process in mind. The results shed light on the intricate processes responsible for affecting the morphology, composition and growth of individual atomic layers and segments that eventually form a complete nanowire. The ultimate goal would of course be to use this deepened understanding to precisely control the growth on a layer (or even atom) basis, deciding every aspect of the final nanowire structure. There are, of course, more steps needed before we get there, and I would therefore like to highlight some aspects in this chapter.

Starting with GaSb, studied in **Paper I** and **IV**, I believe that the diameter modulation shows great prospects of becoming something technologically important. However, for the modulation to be useful it must be realized *ex-situ* in conventional growth systems. What was not discussed within the thesis, but in **Paper I** itself, was that we investigated the possibilities of producing similarly diameter modulated nanowires *ex-situ*. What we found, however, was that the overall diameter of the GaSb segment (grown from GaAs stems) was decided by the conditions intended to produce the largest diameter, if two different conditions were used for the GaSb growth. We suspect therefore that within the parameter space used for the *ex-situ* growth, the overgrowth was significantly more pronounced than for our *in-situ* study. Worth mentioning here is that it is very difficult to translate exact growth parameters even between different *ex-situ* setups. Despite this result, I am confident that if a large separate study were to be conducted with the intention of producing the diameter modulated structures *ex-situ*, it would be possible. The diameter

modulation could also be investigated in other material systems, both *in-situ* and *ex-situ*, to compare trends.

Another aspect of the GaSb material system is the crystal structure. Throughout the investigations conducted here, GaSb always grew in the ZB crystal structure, with possibly stacking defects present at the nucleation stage before the nanowire growth reaches steady-state. Earlier investigations have hinted at the possibility of forming defects in GaSb during stable growth, which could indicate that the formation of a WZ phase is possible.[62] For such investigations, the environmental transmission electron microscope is a magnificent tool, since growth conditions can be changed on the fly. If the growth conditions are altered to either increase or decrease the V/III ratio, and the formation of defects is observed, the user can continue to push the system further up or down in V/III to see if this promotes the formation. This sort of instant feedback is very useful when mapping growth parameters, and will likely lead to more investigations of this kind.

Regarding the InGaAs material system, all the investigations concern to some extent compositional control. In **Paper II** one of the most interesting aspects shown is the fact that kinetically limited models seem to have made correct predictions regarding the compositional relationship between the nanoparticle and the nanowire. What we see is that the nanoparticle needs a lot of In in order for any incorporation of In into the nanowire can occur, but when that is achieved, roughly the same nanoparticle composition can facilitate most of the range of solid compositions. However, **Paper III** suggests that the nanowire itself might also influence the solidifying composition. Simultaneously, GaAs in general shows a much higher supersaturation than InAs, so as long as there is Ga, its incorporation will be favorable. When the Ga supply is decreased in order to make a sharp heterostructure, however, kinking often follows, as shown in the last part of Chapter 6. The complexity of the system might therefore speak favorably for the exploration of other seed particle materials or growth methods for InGaAs nanowires. For example, SAG grown InGaAs nanowires have shown promising results regarding compositional control.[138]

The multilayer growth phenomenon discussed in **Paper V** and **VI** is not helping when trying to achieve control with atomic precision. The growth of several layers at once is likely to affect the smallest achievable number of layers when creating, for example, small and sharp inclusions of GaAs in a nanowire that is predominantly consisting of InAs. In the case of pure GaAs the multilayer growth cannot affect the composition, but if dopants are supplied to change the electronic properties locally, their distribution might be affected by the multilayer growth phenomenon. Regardless of the effects, I would like to see theoretical models that deal with the possibility of multiple nucleation events, as this is a phenomenon that has classically never been considered in nanowire growth models.

In many of the studies presented here, the theoretical models and simulations have played a large complementary role to the *in-situ* experimental investigations. The models and

simulations help in enforcing points about the experimental data and in many cases provide more information that is not as easily accessible experimentally. The model that I have spent most time with is the GaSb simulation developed from an existing GaAs framework.[58] At this point in time, there are two additions that would significantly improve it. For one, it would be beneficial to explore and implement material delivery through diffusion, in order to see if it scales properly with the size of the system, as discussed in Chapter 6. The second addition is a dynamic nanowire diameter, based on the swelling of the nanoparticle. These two additions would allow the model to move from only simulating steady-state growth, to actually being able to simulate changes to the system as a result of altered growth parameters. However, I believe that accurately modeling the expansion of the nanowire will be complex, and therefore a very difficult task to undertake.

In the end, all kinds of investigations, whether *ex-situ*, *in-situ* or computational, are pieces of a massive puzzle with the common goal of creating more and more intricate and atomically controlled nanostructures. From the *in-situ* studies, we have already been able to experimentally observe and measure aspects of the nanowire growth that can both be applied for the construction of better growth models, but also that can have direct technological importance when achieved (or avoided) *ex-situ*. For these reasons I believe that the *in-situ* observation of crystal growth will continue to be a sought after and highly utilized technique to further our understanding of the dynamics at the nanoscale, one atom at a time.

References

[1] L. E. Smart and E. A. Moore, *Solid State Chemistry*. CRC Press, apr 2016.

[2] S. Kasap and P. Capper, *Springer Handbook of Electronic and Photonic Materials*. Springer Handbooks, Cham: Springer International Publishing, 2nd ed., 2017.

[3] K. Tomioka, M. Yoshimura, and T. Fukui, "A III–V nanowire channel on silicon for high-performance vertical transistors," *Nature*, vol. 488, pp. 189–192, aug 2012.

[4] O.-P. Kilpi, J. Svensson, J. Wu, A. R. Persson, R. Wallenberg, E. Lind, and L.-E. Wernersson, "Vertical InAs/InGaAs Heterostructure Metal–Oxide–Semiconductor Field-Effect Transistors on Si," *Nano Letters*, vol. 17, pp. 6006–6010, oct 2017.

[5] R. R. Zamani and J. Arbiol, "Understanding semiconductor nanostructures via advanced electron microscopy and spectroscopy," *Nanotechnology*, vol. 30, p. 262001, jun 2019.

[6] M. Levinshtein, S. Rumyantsev, and M. Shur, *Handbook Series on Semiconductor Parameters*, vol. 2. WORLD SCIENTIFIC, nov 1996.

[7] U. W. Pohl, *Epitaxy of Semiconductors*. Graduate Texts in Physics, Berlin, Heidelberg: Springer Berlin Heidelberg, 1 ed., 2013.

[8] J. Carlin, A. Rudra, and M. Ilegems, "Quantitative study of the incorporation of group III elements in chemical beam epitaxy of GaInAsP alloys," *Journal of Crystal Growth*, vol. 131, pp. 387–394, aug 1993.

[9] C. Thelander, P. Caroff, S. Plissard, and K. A. Dick, "Electrical properties of InAs1−xSbx and InSb nanowires grown by molecular beam epitaxy," *Applied Physics Letters*, vol. 100, p. 232105, jun 2012.

[10] J. J. Hou, F. Wang, N. Han, F. Xiu, S. Yip, M. Fang, H. Lin, T. F. Hung, and J. C. Ho, "Stoichiometric Effect on Electrical, Optical, and Structural Properties of Composition-Tunable InxGa1−xAs Nanowires," *ACS Nano*, vol. 6, pp. 9320–9325, oct 2012.

[11] L. Hrachowina, Y. Chen, E. Barrigón, R. Wallenberg, and M. T. Borgström, "Realization of axially defined GaInP/InP/InAsP triple-junction photovoltaic nanowires for high-performance solar cells," *Materials Today Energy*, vol. 27, p. 101050, jul 2022.

[12] M. Karimi, V. Jain, M. Heurlin, A. Nowzari, L. Hussain, D. Lindgren, J. E. Stehr, I. A. Buyanova, A. Gustafsson, L. Samuelson, M. T. Borgström, and H. Pettersson, "Room-temperature InP/InAsP Quantum Discs-in-Nanowire Infrared Photodetectors," *Nano Letters*, vol. 17, pp. 3356–3362, jun 2017.

[13] P. Laferrière, E. Yeung, L. Giner, S. Haffouz, J. Lapointe, G. C. Aers, P. J. Poole, R. L. Williams, and D. Dalacu, "Multiplexed Single-Photon Source Based on Multiple Quantum Dots Embedded within a Single Nanowire," *Nano Letters*, vol. 20, pp. 3688–3693, may 2020.

[14] R. Oshima, Y. Ishitsuka, Y. Okano, and T. Sugaya, "Growth of InGaAs Solar Cells on InP(001) Miscut Substrates Using Solid-Source Molecular Beam Epitaxy," *physica status solidi (a)*, vol. 217, p. 1900512, feb 2020.

[15] Y. Zhang, W. Si, Y. Jia, P. Yu, R. Yu, and J. Zhu, "Controlling Strain Relaxation by Interface Design in Highly Lattice-Mismatched Heterostructure," *Nano Letters*, vol. 21, pp. 6867–6874, aug 2021.

[16] N. Akopian, G. Patriarche, L. Liu, J.-C. Harmand, and V. Zwiller, "Crystal Phase Quantum Dots," *Nano Letters*, vol. 10, pp. 1198–1201, apr 2010.

[17] D. V. Beznasyuk, E. Robin, M. D. Hertog, J. Claudon, and M. Hocevar, "Dislocation-free axial InAs-on-GaAs nanowires on silicon," *Nanotechnology*, vol. 28, p. 365602, sep 2017.

[18] K. A. Dick, P. Caroff, J. Bolinsson, M. E. Messing, J. Johansson, K. Deppert, L. R. Wallenberg, and L. Samuelson, "Control of III–V nanowire crystal structure by growth parameter tuning," *Semiconductor Science and Technology*, vol. 25, p. 024009, feb 2010.

[19] J. Johansson, J. Bolinsson, M. Ek, P. Caroff, and K. A. Dick, "Combinatorial approaches to understanding polytypism in III-V nanowires," *ACS Nano*, vol. 6, pp. 6142–6149, jul 2012.

[20] M. Heiss, S. Conesa-Boj, J. Ren, H.-H. Tseng, A. Gali, A. Rudolph, E. Uccelli, F. Peiró, J. R. Morante, D. Schuh, E. Reiger, E. Kaxiras, J. Arbiol, and A. Fontcuberta i Morral, "Direct correlation of crystal structure and optical properties in wurtzite/zinc-blende GaAs nanowire heterostructures," *Physical Review B*, vol. 83, p. 045303, jan 2011.

[21] J. Svensson, A. W. Dey, D. Jacobsson, and L. E. Wernersson, "III-V nanowire complementary metal-oxide semiconductor transistors monolithically integrated on Si," *Nano Letters*, vol. 15, pp. 7898–7904, dec 2015.

[22] I. Yang, S. Kim, M. Niihori, A. Alabadla, Z. Li, L. Li, M. N. Lockrey, D. Y. Choi, I. Aharonovich, J. Wong-Leung, H. H. Tan, C. Jagadish, and L. Fu, "Highly uniform InGaAs/InP quantum well nanowire array-based light emitting diodes," *Nano Energy*, vol. 71, p. 104576, may 2020.

[23] H. Sumikura, G. Zhang, M. Takiguchi, N. Takemura, A. Shinya, H. Gotoh, and M. Notomi, "Mid-Infrared Lasing of Single Wurtzite InAs Nanowire," *Nano Letters*, vol. 19, pp. 8059–8065, nov 2019.

[24] L. Hrachowina, N. Anttu, and M. T. Borgström, "Wafer-Scale Synthesis and Optical Characterization of InP Nanowire Arrays for Solar Cells," *Nano Letters*, vol. 21, pp. 7347–7353, sep 2021.

[25] F. Patolsky, G. Zheng, and C. M. Lieber, "Nanowire sensors for medicine and the life sciences," *Nanomedicine*, vol. 1, pp. 51–65, jun 2006.

[26] M. Leijnse and K. Flensberg, "Introduction to topological superconductivity and Majorana fermions," *Semiconductor Science and Technology*, vol. 27, p. 124003, dec 2012.

[27] T. D. Stanescu and S. Tewari, "Majorana fermions in semiconductor nanowires: fundamentals, modeling, and experiment," *Journal of Physics: Condensed Matter*, vol. 25, p. 233201, jun 2013.

[28] A. Krishnaraja, J. Svensson, E. Memisevic, Z. Zhu, A. R. Persson, E. Lind, L. R. Wallenberg, and L.-E. Wernersson, "Tuning of Source Material for InAs/InGaAsSb/GaSb Application-Specific Vertical Nanowire Tunnel FETs," *ACS Applied Electronic Materials*, vol. 2, pp. 2882–2887, sep 2020.

[29] E. Barrigón, M. Heurlin, Z. Bi, B. Monemar, and L. Samuelson, "Synthesis and Applications of III–V Nanowires," *Chemical Reviews*, vol. 119, pp. 9170–9220, aug 2019.

[30] P. C. McIntyre and A. Fontcuberta i Morral, "Semiconductor nanowires: to grow or not to grow?," *Materials Today Nano*, vol. 9, p. 100058, 2020.

[31] D. J. Dunstan, "Strain and strain relaxation in semiconductors," *Journal of Materials Science: Materials in Electronics*, vol. 8, pp. 337–375, 1997.

[32] J. N. Shapiro, A. Lin, P. S. Wong, A. C. Scofield, C. Tu, P. N. Senanayake, G. Mariani, B. L. Liang, and D. L. Huffaker, "InGaAs heterostructure formation in catalyst-free GaAs nanopillars by selective-area metal-organic vapor phase epitaxy," *Applied Physics Letters*, vol. 97, p. 243102, dec 2010.

[33] K. A. Dick, "A review of nanowire growth promoted by alloys and non-alloying elements with emphasis on Au-assisted III–V nanowires," *Progress in Crystal Growth and Characterization of Materials*, vol. 54, pp. 138–173, sep 2008.

[34] J. Wang, S. Plissard, M. Hocevar, T. T. T. Vu, T. Zehender, G. G. W. Immink, M. A. Verheijen, J. Haverkort, and E. P. A. M. Bakkers, "Position-controlled [100] InP nanowire arrays," *Applied Physics Letters*, vol. 100, p. 053107, jan 2012.

[35] M. Heurlin, M. H. Magnusson, D. Lindgren, M. Ek, L. R. Wallenberg, K. Deppert, and L. Samuelson, "Continuous gas-phase synthesis of nanowires with tunable properties," *Nature*, vol. 492, pp. 90–94, dec 2012.

[36] G. B. Stringfellow, *Organometallic Vapor-Phase Epitaxy : theory and practice*. Academic Press, 1999.

[37] C. B. Maliakkal, M. Tornberg, D. Jacobsson, S. Lehmann, and K. A. Dick, "Vapor–solid–solid growth dynamics in GaAs nanowires," *Nanoscale Advances*, vol. 3, no. 20, pp. 5928–5940, 2021.

[38] R. DeHoff, *Thermodynamics in Materials Science*. CRC Press, mar 2006.

[39] A. Dinsdale, "SGTE data for pure elements," *Calphad*, vol. 15, pp. 317–425, oct 1991.

[40] I. V. Markov, *Crystal Growth for Beginners*. WORLD SCIENTIFIC, aug 2003.

[41] R. S. Wagner and W. C. Ellis, "Vapor-Liquid-Solid Mechanism of Single Crystal Growth," *Applied Physics Letters*, vol. 4, pp. 89–90, mar 1964.

[42] B. Ohlsson, M. Björk, A. Persson, C. Thelander, L. Wallenberg, M. Magnusson, K. Deppert, and L. Samuelson, "Growth and characterization of GaAs and InAs nano-whiskers and InAs/GaAs heterostructures," *Physica E: Low-dimensional Systems and Nanostructures*, vol. 13, pp. 1126–1130, mar 2002.

[43] M. Bar-Sadan, J. Barthel, H. Shtrikman, and L. Houben, "Direct Imaging of Single Au Atoms Within GaAs Nanowires," *Nano Letters*, vol. 12, pp. 2352–2356, may 2012.

[44] R. T. Hallberg, S. Lehmann, M. E. Messing, and K. A. Dick, "Palladium seeded GaAs nanowires," *Journal of Materials Research*, vol. 31, pp. 175–185, jan 2016.

[45] M. J. Tambe, S. Ren, and S. Gradečak, "Effects of Gold Diffusion on n-Type Doping of GaAs Nanowires," *Nano Letters*, vol. 10, pp. 4584–4589, nov 2010.

[46] A. J. Tavendale and S. J. Pearton, "Deep level, quenched-in defects in silicon doped with gold, silver, iron, copper or nickel," *Journal of Physics C: Solid State Physics*, vol. 16, pp. 1665–1673, mar 1983.

[47] F. Glas, J.-C. Harmand, and G. Patriarche, "Nucleation Antibunching in Catalyst-Assisted Nanowire Growth," *Physical Review Letters*, vol. 104, p. 135501, mar 2010.

[48] E. K. Mårtensson, S. Lehmann, K. A. Dick, and J. Johansson, "Simulation of GaAs Nanowire Growth and Crystal Structure," *Nano Letters*, vol. 19, pp. 1197–1203, feb 2019.

[49] C. B. Maliakkal, D. Jacobsson, M. Tornberg, A. R. Persson, J. Johansson, R. Wallenberg, and K. A. Dick, "In situ analysis of catalyst composition during gold catalyzed GaAs nanowire growth," *Nature Communications*, vol. 10, p. 4577, dec 2019.

[50] V. G. Dubrovskii, *Nucleation Theory and Growth of Nanostructures*. NanoScience and Technology, Berlin, Heidelberg: Springer Berlin Heidelberg, 2014.

[51] H. A. Fonseka, P. Caroff, J. Wong-Leung, A. S. Ameruddin, H. H. Tan, and C. Jagadish, "Nanowires Grown on InP (100): Growth Directions, Facets, Crystal Structures, and Relative Yield Control," *ACS Nano*, vol. 8, pp. 6945–6954, jul 2014.

[52] A. M. Whiticar, E. K. Mårtensson, J. Nygård, K. A. Dick, and J. Bolinsson, "Annealing of Au, Ag and Au–Ag alloy nanoparticle arrays on GaAs (100) and (111)B," *Nanotechnology*, vol. 28, p. 205702, may 2017.

[53] R. Sjökvist, *Growth of InAsSb and GaAsSb Nanowires*. Master's Thesis: Lund University, 2018.

[54] C. B. Maliakkal, D. Jacobsson, M. Tornberg, and K. A. Dick, "Post-nucleation evolution of the liquid–solid interface in nanowire growth," *Nanotechnology*, vol. 33, p. 105607, mar 2022.

[55] V. G. Dubrovskii and N. V. Sibirev, "Growth rate of a crystal facet of arbitrary size and growth kinetics of vertical nanowires," *Physical Review E*, vol. 70, p. 031604, sep 2004.

[56] V. G. Dubrovskii, "Refinement of Nucleation Theory for Vapor–Liquid–Solid Nanowires," *Crystal Growth & Design*, vol. 17, pp. 2589–2593, may 2017.

[57] E. K. Mårtensson, S. Lehmann, K. A. Dick, and J. Johansson, "Effect of Radius on Crystal Structure Selection in III–V Nanowire Growth," *Crystal Growth & Design*, vol. 20, pp. 5373–5379, aug 2020.

[58] C. B. Maliakkal, E. K. Mårtensson, M. U. Tornberg, D. Jacobsson, A. R. Persson, J. Johansson, L. R. Wallenberg, and K. A. Dick, "Independent Control of Nucleation and Layer Growth in Nanowires," *ACS Nano*, vol. 14, pp. 3868–3875, apr 2020.

[59] D. Jacobsson, S. Lehmann, and K. A. Dick, "Zincblende-to-wurtzite interface improvement by group III loading in Au-seeded GaAs nanowires," *physica status solidi (RRL) - Rapid Research Letters*, vol. 7, pp. 855–859, oct 2013.

[60] H. J. Joyce, J. Wong-Leung, Q. Gao, H. H. Tan, and C. Jagadish, "Phase Perfection in Zinc Blende and Wurtzite III–V Nanowires Using Basic Growth Parameters," *Nano Letters*, vol. 10, pp. 908–915, mar 2010.

[61] F. Glas, J.-C. Harmand, and G. Patriarche, "Why Does Wurtzite Form in Nanowires of III-V Zinc Blende Semiconductors?," *Physical Review Letters*, vol. 99, p. 146101, oct 2007.

[62] S. Gorji Ghalamestani, S. Lehmann, and K. A. Dick, "Can antimonide-based nanowires form wurtzite crystal structure?," *Nanoscale*, vol. 8, no. 5, pp. 2778–2786, 2016.

[63] H. Abu-Farsakh and A. Qteish, "Ionicity scale based on the centers of maximally localized Wannier functions," *Physical Review B*, vol. 75, p. 085201, feb 2007.

[64] P. Caroff, J. B. Wagner, K. A. Dick, H. A. Nilsson, M. Jeppsson, K. Deppert, L. Samuelson, L. R. Wallenberg, and L.-E. Wernersson, "High-Quality InAs/InSb Nanowire Heterostructures Grown by Metal-Organic Vapor-Phase Epitaxy," *Small*, vol. 4, pp. 878–882, jul 2008.

[65] M. Yamaguchi, J.-H. Paek, and H. Amano, "Probability of twin formation on self-catalyzed GaAs nanowires on Si substrate," *Nanoscale Research Letters*, vol. 7, p. 558, dec 2012.

[66] M. Rosini and R. Magri, "Surface Effects on the Atomic and Electronic Structure of Unpassivated GaAs Nanowires," *ACS Nano*, vol. 4, pp. 6021–6031, oct 2010.

[67] S. G. Ghalamestani, M. Ek, and K. A. Dick, "Realization of single and double axial InSb-GaSb heterostructure nanowires," *physica status solidi (RRL) - Rapid Research Letters*, vol. 8, pp. 269–273, mar 2014.

[68] K. A. Dick, S. Kodambaka, M. C. Reuter, K. Deppert, L. Samuelson, W. Seifert, L. R. Wallenberg, and F. M. Ross, "The Morphology of Axial and Branched Nanowire Heterostructures," *Nano Letters*, vol. 7, pp. 1817–1822, jun 2007.

[69] M. Paladugu, J. Zou, Y.-N. Guo, X. Zhang, Y. Kim, H. J. Joyce, Q. Gao, H. H. Tan, and C. Jagadish, "Nature of heterointerfaces in GaAs/InAs and InAs/GaAs axial nanowire heterostructures," *Applied Physics Letters*, vol. 93, p. 101911, sep 2008.

[70] M. E. Messing, J. Wong-Leung, Z. Zanolli, H. J. Joyce, H. H. Tan, Q. Gao, L. R. Wallenberg, J. Johansson, and C. Jagadish, "Growth of Straight InAs-on-GaAs Nanowire Heterostructures," *Nano Letters*, vol. 11, pp. 3899–3905, sep 2011.

[71] S. Vlassov, S. Oras, B. Polyakov, E. Butanovs, A. Kyritsakis, and V. Zadin, "Kinking in Semiconductor Nanowires: A Review," *Crystal Growth & Design*, vol. 22, pp. 871–892, jan 2022.

[72] A. S. Ameruddin, P. Caroff, H. H. Tan, C. Jagadish, and V. G. Dubrovskii, "Understanding the growth and composition evolution of gold-seeded ternary InGaAs nanowires.," *Nanoscale*, vol. 7, no. 39, pp. 16266–72, 2015.

[73] T. Fu, X. Yan, L. Ai, X. Zhang, and X. Ren, "A Si-based InP/InGaAs nanowire array photodetector operating at telecommunication wavelength," *Photonics and Nanostructures - Fundamentals and Applications*, vol. 40, p. 100794, jul 2020.

[74] G. B. Stringfellow, "Spinodal decomposition and clustering in III/V alloys," *Journal of Electronic Materials*, vol. 11, pp. 903–918, sep 1982.

[75] E. D. Leshchenko, M. Ghasemi, V. G. Dubrovskii, and J. Johansson, "Nucleation-limited composition of ternary III–V nanowires forming from quaternary gold based liquid alloys," *CrystEngComm*, vol. 20, no. 12, pp. 1649–1655, 2018.

[76] C. Ophus, "Four-Dimensional Scanning Transmission Electron Microscopy (4D-STEM): From Scanning Nanodiffraction to Ptychography and Beyond," *Microscopy and Microanalysis*, vol. 25, pp. 563–582, jun 2019.

[77] M. H. Leth Larsen, F. Dahl, L. P. Hansen, B. Barton, C. Kisielowski, S. Helveg, O. Winther, T. W. Hansen, and J. Schiøtz, "Reconstructing the exit wave of 2D materials in high-resolution transmission electron microscopy using machine learning," *Ultramicroscopy*, vol. 243, p. 113641, jan 2023.

[78] D. B. Williams and C. B. Carter, *Transmission Electron Microscopy*. Boston, MA: Springer NY, 2 ed., feb 2009.

[79] G. Vicidomini, P. Bianchini, and A. Diaspro, "STED super-resolved microscopy," *Nature Methods*, vol. 15, no. 3, pp. 173–182, 2018.

[80] M. J. Rust, M. Bates, and X. Zhuang, "Sub-diffraction-limit imaging by stochastic optical reconstruction microscopy (STORM)," *Nature Methods*, vol. 3, no. 10, pp. 793–795, 2006.

[81] C. Hetherington, "Aberration correction for TEM," *Materials Today*, vol. 7, pp. 50–55, dec 2004.

[82] D. Jacobsson, F. Panciera, J. Tersoff, M. C. Reuter, S. Lehmann, S. Hofmann, K. A. Dick, and F. M. Ross, "Interface dynamics and crystal phase switching in GaAs nanowires," *Nature*, vol. 531, no. 7594, pp. 317–322, 2016.

[83] J. M. Howe and H. Saka, "In Situ Transmission Electron Microscopy Studies of the Solid–Liquid Interface," *MRS Bulletin*, vol. 29, pp. 951–957, dec 2004.

[84] Z. Ma, W. L. Dacayan, C. Chatzichristodoulou, K. S. Mølhave, F. M. Chiabrera, W. Zhang, and S. B. Simonsen, "Electrochemical Impedance Spectroscopy Integrated with Environmental Transmission Electron Microscopy," *Small Methods*, vol. 7, pp. 1–10, jul 2023.

[85] B. C. da Silva, Z. Sadre Momtaz, E. Monroy, H. Okuno, J.-L. Rouviere, D. Cooper, and M. I. Den Hertog, "Assessment of Active Dopants and p–n Junction Abruptness Using In Situ Biased 4D-STEM," *Nano Letters*, vol. 22, pp. 9544–9550, dec 2022.

[86] M. N. Yesibolati, K. I. Mortensen, H. Sun, A. Brostrøm, S. Tidemand-Lichtenberg, and K. Mølhave, "Unhindered Brownian Motion of Individual Nanoparticles in Liquid-Phase Scanning Transmission Electron Microscopy," *Nano Letters*, vol. 20, pp. 7108–7115, oct 2020.

[87] W. Dachraoui and R. Erni, "Nonclassical Nucleation and Growth of Pd Nanocrystals from Aqueous Solution Studied by In Situ Liquid Transmission Electron Microscopy," *Chemistry of Materials*, vol. 35, pp. 1201–1208, feb 2023.

[88] M. S. Seifner, M. Snellman, O. A. Makgae, K. Kumar, D. Jacobsson, M. Ek, K. Deppert, M. E. Messing, and K. A. Dick, "Interface Dynamics in Ag–Cu 3 P Nanoparticle Heterostructures," *Journal of the American Chemical Society*, vol. 144, pp. 248–258, jan 2022.

[89] O. A. Makgae, T. N. Phaahlamohlaka, B. Yao, M. E. Schuster, T. J. A. Slater, P. P. Edwards, N. J. Coville, E. Liberti, and A. I. Kirkland, "Atomic Structure and Valence State of Cobalt Nanocrystals on Carbon under Syngas Versus Hydrogen Reduction," *The Journal of Physical Chemistry C*, vol. 126, pp. 6325–6333, apr 2022.

[90] A. M. Żak, "Light-Induced In Situ Transmission Electron Microscopy-Development, Challenges, and Perspectives," *Nano Letters*, vol. 22, pp. 9219–9226, dec 2022.

[91] X. Wang, S. Zheng, C. Deng, C. R. Weinberger, G. Wang, and S. X. Mao, "In Situ Atomic-Scale Observation of 5-Fold Twin Formation in Nanoscale Crystal under Mechanical Loading," *Nano Letters*, vol. 23, pp. 514–522, jan 2023.

[92] P. Toth, D. Jacobsson, M. Ek, and H. Wiinikka, "Real-time, in situ, atomic scale observation of soot oxidation," *Carbon*, vol. 145, pp. 149–160, apr 2019.

[93] G. Divitini, S. Cacovich, F. Matteocci, L. Cinà, A. Di Carlo, and C. Ducati, "In situ observation of heat-induced degradation of perovskite solar cells," *Nature Energy*, vol. 1, p. 15012, jan 2016.

[94] A. B. Brady, J. Weber, K. Yuan, L. F. Allard, O. Avina, R. Ogaz, Y.-J. Chang, N. Rampal, V. Starchenko, G. Rother, L. M. Anovitz, J. L. Bañuelos, H.-W. Wang, and A. G. Stack, "In Situ Observations of Barium Sulfate Nucleation in Nanopores," *Crystal Growth & Design*, vol. 22, pp. 6941–6951, dec 2022.

[95] W. Dachraoui, M. I. Bodnarchuk, and R. Erni, "Direct Imaging of the Atomic Mechanisms Governing the Growth and Shape of Bimetallic Pt–Pd Nanocrystals by In Situ Liquid Cell STEM," *ACS Nano*, vol. 16, pp. 14198–14209, sep 2022.

[96] X. Fu, X.-D. Wang, B. Zhao, Q. Zhang, S. Sun, J.-J. Wang, W. Zhang, L. Gu, Y. Zhang, W.-Z. Zhang, W. Wen, Z. Zhang, L.-q. Chen, Q. Yu, and E. Ma, "Atomic-scale observation of non-classical nucleation-mediated phase transformation in a titanium alloy," *Nature Materials*, vol. 21, pp. 290–296, mar 2022.

[97] F. Cavalca, A. B. Laursen, B. E. Kardynal, R. E. Dunin-Borkowski, S. Dahl, J. B. Wagner, and T. W. Hansen, "In situ transmission electron microscopy of light-induced photocatalytic reactions," *Nanotechnology*, vol. 23, p. 075705, feb 2012.

[98] S. B. Vendelbo, C. F. Elkjær, H. Falsig, I. Puspitasari, P. Dona, L. Mele, B. Morana, B. J. Nelissen, R. van Rijn, J. F. Creemer, P. J. Kooyman, and S. Helveg, "Visualization of oscillatory behaviour of Pt nanoparticles catalysing CO oxidation," *Nature Materials*, vol. 13, pp. 884–890, sep 2014.

[99] M. Ek, A. Godiksen, L. Arnarson, P. G. Moses, S. B. Rasmussen, M. Skoglundh, E. Olsson, and S. Helveg, "Redox dynamics of 2D crystalline vanadium oxide phases on high-index anatase facets," *Nanoscale*, vol. 15, no. 21, pp. 9503–9509, 2023.

[100] Y. Xing, I. Kim, K. T. Kang, B. Park, Z. Wang, J. Chan Kim, H. Y. Jeong, W. S. Choi, J. Lee, and S. H. Oh, "Atomic-scale operando observation of oxygen diffusion during topotactic phase transition of a perovskite oxide," *Matter*, vol. 5, pp. 3009–3022, sep 2022.

[101] F. M. Ross, J. Tersoff, and M. C. Reuter, "Sawtooth Faceting in Silicon Nanowires," *Physical Review Letters*, vol. 95, p. 146104, sep 2005.

[102] T. Hu, M. S. Seifner, M. Snellman, D. Jacobsson, M. Sedrpooshan, P. Ternero, M. E. Messing, and K. A. Dick, "Direct Observation of Liquid–Solid Two-Phase Seed Particle-Assisted Kinking in GaP Nanowire Growth," *Small Structures*, p. 2300011, apr 2023.

[103] M. Marnauza, M. Tornberg, E. K. Mårtensson, D. Jacobsson, and K. A. Dick, "In situ observations of size effects in GaAs nanowire growth," *Nanoscale Horizons*, vol. 8, no. 2, pp. 291–296, 2023.

[104] J.-C. Harmand, G. Patriarche, F. Glas, F. Panciera, I. Florea, J.-L. Maurice, L. Travers, and Y. Ollivier, "Atomic Step Flow on a Nanofacet," *Physical Review Letters*, vol. 121, p. 166101, oct 2018.

[105] C. Hetherington, D. Jacobsson, K. A. Dick, and L. R. Wallenberg, "In situ metal-organic chemical vapour deposition growth of III–V semiconductor nanowires in the Lund environmental transmission electron microscope," *Semiconductor Science and Technology*, vol. 35, p. 034004, mar 2020.

[106] M. Tornberg, C. B. Maliakkal, D. Jacobsson, R. Wallenberg, and K. A. Dick, "Enabling In Situ Studies of Metal-Organic Chemical Vapor Deposition in a Transmission Electron Microscope," *Microscopy and Microanalysis*, vol. 28, pp. 1484–1492, oct 2022.

[107] M. H. Magnusson, K. Deppert, J. O. Malm, J. O. Bovin, and L. Samuelson, "Gold nanoparticles: Production, reshaping, and thermal charging," *Journal of Nanoparticle Research*, vol. 1, no. 2, pp. 243–251, 1999.

[108] P. Schlexer, A. B. Andersen, B. Sebok, I. Chorkendorff, J. Schiøtz, and T. W. Hansen, "Size-Dependence of the Melting Temperature of Individual Au Nanoparticles," *Particle & Particle Systems Characterization*, vol. 36, p. 1800480, mar 2019.

[109] M. Tornberg, C. B. Maliakkal, D. Jacobsson, K. A. Dick, and J. Johansson, "Limits of III-V Nanowire Growth Based on Droplet Dynamics," *Journal of Physical Chemistry Letters*, vol. 11, no. 8, pp. 2949–2954, 2020.

[110] M. A. Green, E. D. Dunlop, M. Yoshita, N. Kopidakis, K. Bothe, G. Siefer, and X. Hao, "Solar cell efficiency tables (version 62)," *Progress in Photovoltaics: Research and Applications*, pp. 651–663, jul 2023.

[111] M. Jeppsson, K. A. Dick, J. B. Wagner, P. Caroff, K. Deppert, L. Samuelson, and L.-E. Wernersson, "GaAs/GaSb nanowire heterostructures grown by MOVPE," *Journal of Crystal Growth*, vol. 310, pp. 4115–4121, aug 2008.

[112] M. Borg, *Antimonide Heterostructure Nanowires*. PhD thesis, Lund University, 2012.

[113] B. Mattias Borg and L.-E. Wernersson, "Synthesis and properties of antimonide nanowires," *Nanotechnology*, vol. 24, p. 202001, may 2013.

[114] A. Urbonavicius, *In-Situ Investigation of Particle Assisted GaSb Nucleation Using Environmental TEM*. Master's Thesis: Lund University, 2023.

[115] M. Hÿtch, E. Snoeck, and R. Kilaas, "Quantitative measurement of displacement and strain fields from HREM micrographs," *Ultramicroscopy*, vol. 74, pp. 131–146, aug 1998.

[116] M. Ek, B. M. Borg, J. Johansson, and K. A. Dick, "Diameter Limitation in Growth of III-Sb-Containing Nanowire Heterostructures," *ACS Nano*, vol. 7, pp. 3668–3675, apr 2013.

[117] M. Ek, C. L. M. Petersson, J. Wallentin, D. Wahlqvist, A. Ahadi, M. Borgström, and R. Wallenberg, "Compositional analysis of oxide-embedded III–V nanostructures," *Nanotechnology*, vol. 33, p. 375705, sep 2022.

[118] K. A. Dick, K. Deppert, L. Samuelson, and W. Seifert, "InAs nanowires grown by MOVPE," *Journal of Crystal Growth*, vol. 298, pp. 631–634, jan 2007.

[119] Z. X. Yang, S. Yip, D. Li, N. Han, G. Dong, X. Liang, L. Shu, T. F. Hung, X. Mo, and J. C. Ho, "Approaching the Hole Mobility Limit of GaSb Nanowires," *ACS Nano*, vol. 9, pp. 9268–9275, sep 2015.

[120] M. Y. Swinkels, M. R. van Delft, D. S. Oliveira, A. Cavalli, I. Zardo, R. W. van der Heijden, and E. P. A. M. Bakkers, "Diameter dependence of the thermal conductivity of InAs nanowires," *Nanotechnology*, vol. 26, p. 385401, sep 2015.

[121] M. Scheffler, S. Nadj-Perge, L. P. Kouwenhoven, M. T. Borgström, and E. P. A. M. Bakkers, "Diameter-dependent conductance of InAs nanowires," *Journal of Applied Physics*, vol. 106, p. 124303, dec 2009.

[122] M. Ko, S. H. Baek, B. Song, J. W. Kang, S. A. Kim, and C. H. Cho, "Periodically Diameter-Modulated Semiconductor Nanowires for Enhanced Optical Absorption," *Advanced Materials*, vol. 28, no. 13, pp. 2504–2510, 2016.

[123] V. A. Nebol'sin and A. A. Shchetinin, "Role of Surface Energy in the Vapor–Liquid–Solid Growth of Silicon," *Inorganic Materials*, vol. 39, pp. 899–903, 2003.

[124] V. J. Gómez, M. Marnauza, K. A. Dick, and S. Lehmann, "Growth selectivity control of InAs shells on crystal phase engineered GaAs nanowires," *Nanoscale Advances*, vol. 4, no. 16, pp. 3330–3341, 2022.

[125] H. J. Joyce, Q. Gao, J. Wong-Leung, Y. Kim, H. H. Tan, and C. Jagadish, "Tailoring GaAs, InAs, and InGaAs Nanowires for Optoelectronic Device Applications," *IEEE Journal of Selected Topics in Quantum Electronics*, vol. 17, pp. 766–778, jul 2011.

[126] J. C. Shin, D. Y. Kim, A. Lee, H. J. Kim, J. H. Kim, W. J. Choi, H.-S. Kim, and K. J. Choi, "Improving the composition uniformity of Au-catalyzed InGaAs nanowires on silicon," *Journal of Crystal Growth*, vol. 372, pp. 15–18, jun 2013.

[127] E. D. Leshchenko and J. Johansson, "Role of thermodynamics and kinetics in the composition of ternary III-V nanowires," *Nanomaterials*, vol. 10, pp. 1–15, dec 2020.

[128] T. Jean and V. G. Dubrovskii, "Suppression of miscibility gaps in vapor-liquid-solid InGaAs and InGaN nanowires," *Journal of Physics: Conference Series*, vol. 1124, p. 022031, dec 2018.

[129] J. Johansson and M. Ghasemi, "Composition of Gold Alloy Seeded InGaAs Nanowires in the Nucleation Limited Regime," *Crystal Growth & Design*, vol. 17, pp. 1630–1635, apr 2017.

[130] J. Johansson and M. Ghasemi, "Kinetically limited composition of ternary III-V nanowires," *Physical Review Materials*, vol. 1, p. 040401, sep 2017.

[131] E. K. Mårtensson, J. Johansson, and K. A. Dick, "Simulating Vapor–Liquid–Solid Growth of Au-Seeded InGaAs Nanowires," *ACS Nanoscience Au*, vol. 2, pp. 239–249, jun 2022.

[132] E. Mårtensson, *Kinetic and Thermodynamic Modeling of Nanowire Growth*. PhD thesis, Lund University, 2021.

[133] A. Pishchagin, F. Glas, G. Patriarche, A. Cattoni, J.-C. Harmand, and F. Oehler, "Dynamics of Droplet Consumption in Vapor–Liquid–Solid III–V Nanowire Growth," *Crystal Growth & Design*, vol. 21, pp. 4647–4655, aug 2021.

[134] M. De Luca, C. Fasolato, M. A. Verheijen, Y. Ren, M. Y. Swinkels, S. Kölling, E. P. A. M. Bakkers, R. Rurali, X. Cartoixà, and I. Zardo, "Phonon Engineering in Twinning Superlattice Nanowires," *Nano Letters*, vol. 19, pp. 4702–4711, jul 2019.

[135] Z. Azimi, N. Gagrani, J. Qu, O. L. C. Lem, S. Mokkapati, J. M. Cairney, R. Zheng, H. H. Tan, C. Jagadish, and J. Wong-Leung, "Understanding the role of facets and twin defects in the optical performance of GaAs nanowires for laser applications," *Nanoscale Horizons*, vol. 6, pp. 559–567, jun 2021.

[136] V. G. Dubrovskii, "Self-regulated pulsed nucleation in catalyzed nanowire growth," *Physical Review B*, vol. 87, p. 195426, may 2013.

[137] M. Paladugu, J. Zou, Y.-N. Guo, G. J. Auchterlonie, H. J. Joyce, Q. Gao, H. Hoe Tan, C. Jagadish, and Y. Kim, "Novel Growth Phenomena Observed in Axial InAs/GaAs Nanowire Heterostructures," *Small*, vol. 3, pp. 1873–1877, nov 2007.

[138] Z. Azimi, A. Gopakumar, A. S. Ameruddin, L. Li, T. Truong, H. T. Nguyen, H. H. Tan, C. Jagadish, and J. Wong-Leung, "Tuning the crystal structure and optical properties of selective area grown InGaAs nanowires," *Nano Research*, vol. 15, pp. 3695–3703, apr 2022.

Scientific publications